

# IMPERFECT QUANTUM PHOTONIC INTEGRATED CIRCUITS WITH QUANTUM DOT PHASE SHIFTERS

by

ADAM ROBERT JAMES MCCAW

A thesis submitted to the  
Department of Physics, Engineering Physics, & Astronomy  
in conformity with the requirements for  
the degree of Master of Applied Science

Queen's University  
Kingston, Ontario, Canada  
September 2023

Copyright © Adam Robert James McCaw, 2023

# Abstract

There has recently been a tremendous movement in research towards the field of quantum computing due to its potential to solve problems not possible with classical systems. Quantum computers can be implemented using on-chip quantum photonic circuits, which leverage photons as information for low-loss, high-speed processing. Integrating these circuits on-chip would allow for mass production with consistent performance and integration with electronic components. However, these circuits need to be cryogenically compatible to integrate single-photon detectors, and highly scalable for complex circuit implementation. In this thesis, we propose the use of quantum dots as phase shifters in quantum photonic circuits, which provide advantages over current phase shifter architecture through cryogenic compatibility, compactness, and fast reconfigurability. We show how chirally coupled quantum dots can achieve directional photon scattering with phase shifts of  $[-\pi, \pi]$ , and how these can be used in Mach-Zehnder interferometer mesh architecture to implement any linear quantum circuit. We then go on to consider both nanophotonic and quantum dot imperfections, implementing a novel global phase shift optimization method to improve performance. By simulating random circuits with ranges of imperfections, we determine performance dependence for each imperfection independently. We then simulate state-of-the-art and typical imperfections to determine our architecture's

validity and scalability. From these results, we determine that fault-tolerant, highly-scalable quantum computers are achievable with this architecture. Lastly, we consider this architecture for specific circuits, where we see near-perfect performance for state-of-the-art imperfections.

## Acknowledgments

First and foremost, I would like to thank my primary supervisor Prof. Nir Rotenberg for making this thesis possible with his constant guidance. His genuine interest in this project was highly motivating and he was always able to make time to answer questions and provide feedback, allowing me to overcome difficult hurdles in this project. I would also like to thank my co-supervisor Prof. Bhavin J. Shastri for his support, guidance, and questions that helped me develop a better understanding of my work. Thank you to both my professors for allowing me to work with them as it has been a tremendous learning experience.

I would also like to thank all my labmates in the Quantum Nanophotonics Lab at Queen's University who were the best coworkers I could have asked for. Specifically, I would like to thank Jacob Ewaniuk for all the helpful suggestions and discussions that helped bolster my knowledge of quantum photonics. He and I were Nir's first students at Queen's and his hard work and incredible organizational skills were essential for the development of our lab. I would also like to thank Adam Grace and Andrew Wakileh for their essential roles in building the lab and for many thought-provoking discussions on quantum photonics. Thank you as well to everyone from Shastri Lab for helpful guidance and fun socials. It is sad to be leaving the group after all this time, but I am very excited to see what QNL and Shastri Lab can do in the future

as I know they are destined for great accomplishments.

I would also like to thank all the friends who have supported me throughout my time here. Namely: Alan, Connor, Justin, Noah, and all the other members from the fictional Wolp State University. Not to mention everyone from Wally 10, I was very lucky to meet such a great group of lifelong friends all the way back in first year. My years at Queen's have been the best of my life, and I have them to thank for that. Last but not least I would like to thank my family, who provided me with the opportunity to be here, and support me through everything in life. This would not have been possible without them.

# Contents

<b>Abstract</b>	<b>i</b>
<b>Acknowledgments</b>	<b>iii</b>
<b>Contents</b>	<b>v</b>
<b>List of Tables</b>	<b>viii</b>
<b>List of Figures</b>	<b>ix</b>
<b>Chapter 1: Introduction</b>	<b>1</b>
1.1 Motivation . . . . .	1
1.2 On-Chip Quantum Photonic Circuit Requirements . . . . .	3
1.3 Thesis Objective . . . . .	4
1.4 Thesis Organization . . . . .	6
<b>Chapter 2: Reconfigurable Quantum Photonic Circuits</b>	<b>7</b>
2.1 Quantum Photonic Integrated Circuits . . . . .	7
2.1.1 Photonic Qubits . . . . .	7
2.1.2 Quantum Circuit Transfer Matrices . . . . .	8
2.1.3 Mach-Zehnder Interferometer Architecture . . . . .	10
2.1.4 MZI Meshes and Decomposition Procedure . . . . .	13
2.1.5 Transferring to the Fock Basis for Multi-Qubit Gates . . . . .	18
2.2 Nanophotonic Imperfections . . . . .	19
2.2.1 Beam Splitter Error . . . . .	19
2.2.2 Nanophotonic Loss . . . . .	19
2.3 MZM Optimization . . . . .	20
2.3.1 Methods of Measuring Mesh Accuracy . . . . .	20
2.3.2 Common Optimization Methods . . . . .	23
2.3.3 Our Optimization Methods . . . . .	24
<b>Chapter 3: Quantum Dots as Phase Shifters</b>	<b>27</b>

3.1	Quantum Dots and Light-Matter Interactions . . . . .	27
3.2	Quantum Dots Embedded in a Waveguide . . . . .	29
3.2.1	Mathematical Model of a Two-Level System . . . . .	30
3.2.2	Embedding the Emitter in a Waveguide . . . . .	31
3.2.3	Moving into the Interaction Picture . . . . .	32
3.2.4	Electric Field Derivation . . . . .	35
3.2.5	The Rotating Wave Approximation . . . . .	36
3.2.6	Deriving the Scattered Field from the Emitter . . . . .	37
3.3	Symmetric Coupling and Scattering Power Dependence . . . . .	43
3.4	Chiral Quantum Dot Coupling . . . . .	47
3.5	Chiral Quantum Dot Imperfections . . . . .	52
3.5.1	Quantum Dot Losses . . . . .	52
3.5.2	Environmental Interactions with Emitters . . . . .	55
3.6	Reconfigurability through Detuning . . . . .	57
<b>Chapter 4:</b>	<b>Circuit Simulations and Results</b>	<b>61</b>
4.1	Simulations with Nanophotonic Imperfections . . . . .	61
4.2	Simulations with Imperfect Directionality and Coupling . . . . .	66
4.3	Simulating Dephasing . . . . .	70
4.3.1	The Probabilistic Model for Dephasing . . . . .	70
4.3.2	Dephasing Using Monte-Carlo Simulations . . . . .	73
4.4	Simulating Spectral Diffusion . . . . .	77
4.4.1	The Convolutional Model for Spectral Diffusion . . . . .	77
4.4.2	Spectral Diffusion Using Monte-Carlo Simulations . . . . .	78
4.5	Simulated Circuit Scalability . . . . .	80
4.6	Two-Qubit Example Circuit Simulations . . . . .	83
4.6.1	CNOT and CZ Matrix Infidelity . . . . .	84
4.6.2	CNOT and CZ Output Infidelity . . . . .	87
<b>Chapter 5:</b>	<b>Conclusions and Outlook</b>	<b>92</b>
5.1	Summary . . . . .	92
5.2	Future Work . . . . .	94
	<b>Bibliography</b>	<b>96</b>
<b>Appendix A:</b>	<b>Additional Mathematical Derivation for Chapter 3</b>	<b>114</b>
A.1	Interaction Picture Evolution Operator Derivation . . . . .	114
A.2	Current Density Operator Derivation . . . . .	116
A.3	Open System Emitter Dynamics and the Density Matrix . . . . .	118
A.4	Commutator Derivation for Heisenberg Equation of Motion . . . . .	121

<b>Appendix B: Supplemental Data and Analysis for Chapter 4</b>	<b>124</b>
B.1 Infidelity Beta Distributions . . . . .	124
B.2 Optimization Convergence and Tolerance . . . . .	126
B.3 Supplemental Monte-Carlo Testing Data . . . . .	127



# List of Tables

# List of Figures

2.1	Dual rail encoding scheme for photonic qubits . . . . .	8
2.2	Mach-Zehnder interferometer rectangular mesh (MZM) architecture. (a) The ideal $2 \times 2$ Mach-Zehnder interferometer (b) An example $4 \times 4$ MZM . . . . .	12
2.3	Local MZI mesh optimization results for one random unitary of sizes $N = 2, 6, 10$ with beam splitter error ranging from 0% to 50% . . . .	25
3.1	Quantum emitter as a two-level system coupled to a light field. . . . .	28
3.2	Initial and scattered positive frequency field for a quantum dot in a waveguide . . . . .	39
3.3	Light-matter interaction dependence on Rabi frequency . . . . .	46
3.4	Chiral quantum dot coupled to a waveguide. . . . .	48
3.5	Transmission and phase shift detuning dependence. (a) Coherent and incoherent transmission across a range of detunings. (b) QD scattered phase shift for different dephasings across a range of detunings. (c) QD scattered phase shift for different directionalities across a range of detunings. . . . .	59
4.1	Example distribution for nanophotonic loss with a central value of 4.5%. 62	

4.2	Circuit infidelities spanning across nanophotonic losses of 0.1% to 50% for $N = 2, 6, 10$ modes, including imperfect and optimized results. . .	63
4.3	Circuit infidelities spanning beam splitter errors of 0.1% to 50% for $N = 2, 6, 10$ modes, with both imperfect and optimized results. . . .	65
4.4	Circuit infidelities for couplings ranging from $\beta = 0.5$ to $\beta = 1$ , for $N = 2, 6, 10$ modes with both imperfect and optimized results. . . .	68
4.5	Directionality infidelity simulations spanning $D = 0$ to $D = 1$ for circuit sizes of $N = 2, 6, 10$ , with both imperfect and optimized results. . .	69
4.6	Dephasing infidelity simulations for $N = 2, 6, 10$ circuits using the complete probabilistic model. Results are shown for both imperfect and optimized data. . . . .	72
4.7	Monte-Carlo sample testing for dephasing and spectral diffusion. Infidelities shown with beta fit standard deviation errors for $N = 4$ circuits, from 10 to 10000 Monte-Carlo samples with $\Gamma_{dp} = 0.001\Gamma$ and $\sigma_{SD} = 0.01\Gamma$ . . . . .	74
4.8	Dephasing model comparison between the complete probabilistic model and the Monte-Carlo approximation for $\Gamma_{dp} = 10^{-4}\Gamma$ to $\Gamma_{dp} = 0.10\Gamma$ . Results are shown for both imperfect and optimized data for (a) $N = 2$ simulations, and (b) $N = 4$ simulations. . . . .	76
4.9	Infidelity results from dephasing span of $\Gamma_{dp} = 10^{-4}\Gamma$ to $\Gamma_{dp} = 0.10\Gamma$ for the Monte-Carlo dephasing model. Results are shown for the imperfect and optimized data for $N = 2, 6, 10$ . . . . .	77

4.10	Example detuning and phase shift transformations from spectral diffusion of $\sigma_{SD} = 0.30\Gamma$ for $\Delta_P = 0.1\Gamma$ over 10000 samples. (a) Depicts the detuning distribution. (b) Depicts the phase shift distribution. . .	78
4.11	Circuit infidelity simulation results for spectral diffusion span from $\sigma_{SD} = 10^{-4}\Gamma$ to $\sigma_{SD} = 0.30\Gamma$ . Shown for imperfect and optimized data for $N = 2, 6, 10$ . . . . .	80
4.12	Optimized circuit infidelity plot from $N = 2$ to $N = 10$ . Infidelities shown for 100 Haar random unitaries for nanophotonic (red), state-of-the-art (green), typical (navy) imperfections. Includes typical imperfections without spectral diffusion (purple) and without dephasing and spectral diffusion (orange). . . . .	82
4.13	Unheralded CNOT imperfect and optimized matrix infidelities for nanophotonic, state-of-the-art, and typical imperfections across $\Gamma_{dp} = 10^{-4}\Gamma$ to $\Gamma_{dp} = 0.10\Gamma$ . . . . .	85
4.14	Unheralded CZ imperfect and optimized matrix infidelities for nanophotonic, state-of-the-art, and typical imperfections across $\Gamma_{dp} = 10^{-4}\Gamma$ to $\Gamma_{dp} = 0.10\Gamma$ . . . . .	86
4.15	CNOT post-selected imperfect and optimized $4 \times 4$ matrices and their associated conditional infidelities for nanophotonic, state-of-the-art, and typical imperfections. . . . .	89
4.16	CZ post-selected imperfect and optimized $4 \times 4$ matrices and their associated conditional infidelities for nanophotonic, state-of-the-art, and typical imperfections. . . . .	91

B.1	Matrix infidelity histogram over 100 Haar random $N = 4$ circuits for a beam splitter error of 2.3%, showing the mean of the data, a beta fit, and a normal fit. . . . .	125
B.2	Standard deviation between Monte-Carlo samples for $N = 3, 4, 6, 10$ circuit infidelities with $\Gamma_{dp} = 0.001\Gamma$ and $\sigma_{SD} = 0.01\Gamma$ for 10 to 10000 Monte-Carlo Samples per unitary. . . . .	127
B.3	Standard deviation between Monte-Carlo samples for $N = 3, 4, 6, 10$ circuit infidelities with $\Gamma_{dp} = 0.01\Gamma$ and $\sigma_{SD} = 0.01\Gamma$ for 10 to 10000 Monte-Carlo Samples per unitary. . . . .	128
B.4	Standard deviation between Monte-Carlo samples for $N = 3, 4, 6, 10$ circuit infidelities with $\Gamma_{dp} = 0.10\Gamma$ and $\sigma_{SD} = 0.01\Gamma$ for 10 to 10000 Monte-Carlo Samples per unitary. . . . .	129
B.5	Monte-Carlo sample testing for dephasing and spectral diffusion. Infidelities shown with beta fit standard deviation errors for $N = 4$ circuits, from 10 to 10000 Monte-Carlo samples with $\Gamma_{dp} = 0.01\Gamma$ and with spectral diffusion of $\sigma_{SD} = 0.01\Gamma$ . . . . .	130
B.6	Monte-Carlo sample testing for dephasing and spectral diffusion. Infidelities shown with beta fit standard deviation errors for $N = 4$ circuits, from 10 to 10000 Monte-Carlo samples with $\Gamma_{dp} = 0.10\Gamma$ and with spectral diffusion of $\sigma_{SD} = 0.01\Gamma$ . . . . .	131
B.7	Monte-Carlo sample testing for dephasing and spectral diffusion. Infidelities shown with beta fit standard deviation errors for $N = 3$ circuits, from 10 to 10000 Monte-Carlo samples with $\Gamma_{dp} = 0.001\Gamma$ and with spectral diffusion of $\sigma_{SD} = 0.01\Gamma$ . . . . .	132

B.8	Monte-Carlo sample testing for dephasing and spectral diffusion. Infidelities shown with beta fit standard deviation errors for $N = 6$ circuits, from 10 to 10000 Monte-Carlo samples with $\Gamma_{dp} = 0.001\Gamma$ and with spectral diffusion of $\sigma_{SD} = 0.01\Gamma$ . . . . .	133
B.9	Monte-Carlo sample testing for dephasing and spectral diffusion. Infidelities shown with beta fit standard deviation errors for $N = 10$ circuits, from 10 to 10000 Monte-Carlo samples with $\Gamma_{dp} = 0.001\Gamma$ and with spectral diffusion of $\sigma_{SD} = 0.01\Gamma$ . . . . .	134

# Chapter 1

## Introduction

### 1.1 Motivation

Quantum information processing (QIP) has recently exploded in popularity, with companies and researchers racing to be the first to implement scalable quantum computers that achieve quantum advantage [1, 2, 3, 4]. Quantum advantage refers to QIP's ability to solve computational problems that cannot be solved in a reasonable time with classical systems. This stems from the unique quantum properties of superposition and entanglement, which allow the implementation of quantum algorithms that cannot be implemented on classical computers [5]. Examples of these include Shor's algorithm [6], which has the potential to break classical cryptography as we know it, and Grover's search algorithm [7], which can search a solution space in  $O(\sqrt{N})$  time where a classical computer would require  $O(N)$  time. These algorithms give rise to applications in complex system simulation and optimization [8, 9, 10], quantum neural networks [11, 12], secure quantum encryption [13, 14], drug discovery [15], financial modeling [16] and much more [17, 18, 19].

Quantum computing uses qubits (quantum bits) for information in lieu of classical

bits, which can be encoded into a quantum superposition, where a qubit can be in both states  $|0\rangle$  and  $|1\rangle$  at the same time. However, qubits in superposition will collapse their state when measured, changing the state, and making quantum states impossible to clone [20]. Additionally, qubits can be entangled, meaning their states depend on each other, so by measuring one entangled qubit the other's state can be known without the need for measurement [21]. This allows for quantum teleportation, where quantum information can be sent across large distances assuming there is also a classical information link between sender and receiver [22].

While some applications such as quantum encryption take advantage of the inability to clone quantum states, this makes quantum computers difficult to implement due to their sensitivity to loss and error. As a result, fault-tolerant scalable reconfigurable quantum computers have yet to be implemented successfully. However, it has been determined that if quantum circuit infidelity, a measure of a circuit's error on a scale from 0 to 1, is  $\leq 0.01$  [23], then fault-tolerant quantum computing can theoretically be achieved using error-correcting codes and additional components.

Due to the need for low loss and error, single photons are a natural choice for qubits, since they have minimal interaction with the environment. Photons have multiple properties that can store quantum information such as polarization [24], frequency [25], time [2], and path [26]. They can also be processed in circuits using optical components like beam splitters, which route the amplitude of light, and phase shifters, which manipulate the phase [26, 27]. Since photons travel at light speed with limited environmental interaction, they also become the leading choice for efficient quantum communication [28], since other implementations, such as superconducting qubits [29] and trapped ions [30], do not allow qubits to be sent over long distances.



## **1.2. ON-CHIP QUANTUM PHOTONIC CIRCUIT REQUIREMENTS**

---

By coupling photons to optical waveguides, quantum photonic circuits can be implemented on-chip, known as quantum photonic integrated circuits (QPIC), allowing mass production, consistent performance, and integration with electrical systems. As a result, quantum photonic circuits have become a leading architecture in quantum computing, and they have already shown a quantum advantage for specific problems [2].

### **1.2 On-Chip Quantum Photonic Circuit Requirements**

To implement arbitrary quantum circuits successfully, they need to be reconfigurable. By reconfiguring your circuits, you can not only implement reprogrammable quantum circuits but also adjust for fabrication errors in components. Current on-chip implementations achieve this primarily through phase shifter reconfiguration, which when paired with beam splitters, can implement any linear quantum circuit [26]. Hardware component choice is important for quantum circuit implementation as they need to be highly scalable, since large many-qubit circuits are required for useful applications that can implement quantum advantage. They also need to have low loss and error for fault-tolerant quantum computing and need to be quickly reconfigurable for high processing speeds. Additionally, state-of-the-art single photon sources and detectors are implemented in cryogenic temperatures, so hardware components must be cryogenically compatible to implement a complete on-chip quantum circuit.

Reconfigurable on-chip photonic phase shifters have many different implementation methods. These include thermo-optic phase shifters [31, 32], micro and nano-electro-mechanical systems (MEMS, NEMS) [33, 34], free-carrier-based phase shifters [35], and lithium niobate electro-optic phase shifters [36, 37]. Thermo-optic phase

shifters are the most commonly implemented in quantum circuit architectures [38, 39, 40], as they have the lowest insertion losses ( $< 0.01dB$  [32]), maximizing performance. However, they also have limitations; they are bulky, ranging in lengths from tens to hundreds of microns, have high power consumption, and have slow reconfigurability on the order of  $MHz$  [31]. They also each require heaters with independent voltage control and are not cryogenically compatible. MEMS and NEMS implementations boast lower power, with slightly smaller footprints on the order of microns and are cryogenically compatible, but also have slow ( $MHz$ ) reconfigurability, with insertion losses on the order of  $< 1dB$  [33, 34]. Free-carrier-based phase shifters boast faster reconfigurability ( $> GHz$ ) and are cryogenically compatible, but have large footprints on the order of hundreds to thousands of microns, and also have higher insertion losses since photons can be absorbed by the free carriers [35]. Lastly, lithium niobate-based electro-optic phase shifters can achieve up to hundreds of  $GHz$  for reconfigurability and are cryogenically compatible, but have losses on the order of  $0.5dB$ , and are not compact, with lengths of  $mm$  to tens of  $mm$  [36, 37]. All current phase shift implementations use a small change in refractive index for the phase shift, so they lack compactness as they require long lengths to achieve large phase shifts.

Thus, the industry lacks a phase-shift architecture that can be integrated on-chip that is compatible with current quantum infrastructure, has a small footprint, has quick reconfigurability, and has low loss and error.

### 1.3 Thesis Objective

In this work, we propose a new architecture to solve this problem using quantum dots, which are man-made groupings of atoms that act as a two-level system, as

phase shifters in our circuits. We show in Chapter 3, that by scattering light off a quantum dot (QD), you can impart a phase shift that can be reconfigured by adjusting QD parameters. Since this phase shift occurs through interaction with a QD it does not rely on long phase shifter length for refractive index changes. Quantum dots are also minuscule, on the order of tens of  $nm$  [41], and when they are embedded within a p-i-n diode (which are on the order of tens to hundreds of  $nm$  in size), they can be reconfigured through a Stark shift through the application of an electric field [42]. This method boasts similar speeds to free-carrier-based phase shifters on the order of  $GHz$ , providing quick reconfigurability and improving compactness by an order of magnitude over existing methods. They have also been shown to be reconfigurable with pump photons through an AC Stark shift, removing the need for electrical components in the circuit, and offering the potential for sub-nanosecond ( $> GHz$ ) reconfigurability [43]. Additionally, QDs are cryogenically compatible and can be integrated on the same platforms as single-photon sources and detectors. High QD to waveguide coupling efficiencies have been shown [44], indicating they can achieve low insertion losses of  $< 0.01dB$ . These properties suggest that QDs would be a natural choice as phase shifters for quantum photonic integrated circuits, as they have the potential to achieve all the requirements for high performance scalable QPICs, unlike existing methods.

While QDs have long been considered for use as single photon sources, it is only within the last decade that people have considered building devices with quantum emitters, such as QDs, as processing components [45]. In addition to their use as phase shifters, quantum emitters have been considered for optical isolators [46], circulators [47], and switches [48]. The goal of this work is to consider, for the first time, the

use of many quantum dot phase shifters in a fully quantum scalable on-chip quantum photonic circuit and determine the viability of this approach in terms of performance and scalability. To do this, we consider both nanophotonic and QD imperfections and develop a model for simulating and optimizing these circuits to determine performance limits.

#### 1.4 Thesis Organization

Having covered the motivations and goals of this work in this Chapter, Chapter 2 discusses the background behind on-chip quantum photonic circuits, their nanophotonic imperfections, and their optimization. Chapter 3 then covers the background behind quantum dots, how to harness their phase shifts, and quantum dot imperfections. Chapter 4 moves on to the simulation results for these circuits, exploring the effects of different imperfections on performance and scalability for arbitrary circuits, as well as considering their effects on specific example circuits. Finally, in Chapter 5, we summarize the results and discuss the conclusions and outlook of this work.

## Chapter 2

# Reconfigurable Quantum Photonic Circuits

### 2.1 Quantum Photonic Integrated Circuits

#### 2.1.1 Photonic Qubits

In Chapter 1, we noted that qubits can be in the states  $|0\rangle$  and  $|1\rangle$ , which is known as the Z basis. This is not the only way to encode qubits, but it is the most common [21]. Other bases such as the X basis are also common, consisting of  $|+\rangle$  and  $|-\rangle$  states, which can be written in the Z basis as,

$$\begin{aligned} |+\rangle &= \frac{1}{\sqrt{2}}(|0\rangle + |1\rangle) \\ |-\rangle &= \frac{1}{\sqrt{2}}(|0\rangle - |1\rangle), \end{aligned} \tag{2.1}$$

which is used for simulations in Chapter 4.

In this work, we encode photonic qubits using path encoding, as it has the most developed integration for on-chip circuitry [26, 49, 38]. More specifically, we consider dual-rail encoding, as shown in Figure 2.1, where one qubit is encoded with two waveguide paths such that a photon in the top path corresponds to a  $|0\rangle$  state, and

in the bottom path corresponds to a  $|1\rangle$  state. Mathematically, we represent these qubit states as vectors, where for single qubits we have,

$$|0\rangle = \begin{bmatrix} 1 \\ 0 \end{bmatrix}, |1\rangle = \begin{bmatrix} 0 \\ 1 \end{bmatrix}, \quad (2.2)$$

represented by a two-entry column vector. Similarly, we can extend this encoding to the two-qubit basis states,

$$|00\rangle = \begin{bmatrix} 1 \\ 0 \\ 0 \\ 0 \end{bmatrix}, |01\rangle = \begin{bmatrix} 0 \\ 1 \\ 0 \\ 0 \end{bmatrix}, |10\rangle = \begin{bmatrix} 0 \\ 0 \\ 1 \\ 0 \end{bmatrix}, |11\rangle = \begin{bmatrix} 0 \\ 0 \\ 0 \\ 1 \end{bmatrix}, \quad (2.3)$$

where we use four-entry column vectors.

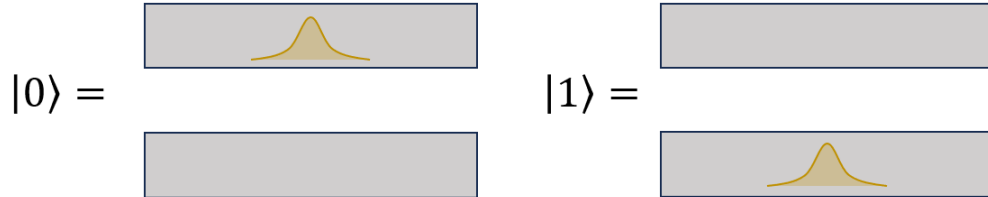


Figure 2.1: Dual rail encoding of photonic qubits. The boxes represent waveguides, where a photon in the top waveguide corresponds to the  $|0\rangle$  state, and a photon in the bottom waveguide corresponds to the  $|1\rangle$  state.

### 2.1.2 Quantum Circuit Transfer Matrices

The basis of a quantum circuit is that it performs an operation on the input qubits, resulting in a transformation to a desired output state. Thus, it becomes convenient

to map these transformations to transfer matrices, where the matrix acts on the input vector to produce the output. In fact, any linear quantum circuit, meaning a circuit with linear components that becomes inherently probabilistic when dealing with multiple photons [27], can be represented by a unitary transfer matrix,  $\hat{U}$ , defined as,

$$\hat{U}^\dagger \hat{U} = \hat{U} \hat{U}^\dagger = \hat{I}, \quad (2.4)$$

where  $\hat{I}$  is the identity matrix [49]. Unitary matrices preserve normalization, so it logically follows that a quantum circuit with no loss would be unitary, and since they are unitary, they are also by definition reversible. This scales such that with an  $N$  mode (number of input/output ports) quantum circuit, the circuit's unitary matrix would be  $N \times N$ .

While any unitary is a quantum circuit, some specific unitaries are commonly studied due to their applications. For example, the Hadamard single qubit gate,

$$H = \frac{1}{\sqrt{2}} \begin{bmatrix} 1 & 1 \\ 1 & -1 \end{bmatrix}, \quad (2.5)$$

is often used since it brings the  $|0\rangle$  state (or the  $|1\rangle$  state) into a superposition of  $|0\rangle$  and  $|1\rangle$  [50]. For two-qubit gates, a common gate is the controlled-not (CNOT),

$$CNOT = \begin{bmatrix} 1 & 0 & 0 & 0 \\ 0 & 1 & 0 & 0 \\ 0 & 0 & 0 & 1 \\ 0 & 0 & 1 & 0 \end{bmatrix}, \quad (2.6)$$

where the first qubit is a control qubit that determines if the second qubit swaps between  $|0\rangle$  and  $|1\rangle$ . The CNOT gate can be used in a variety of circuits, but its popularity stems from its ability to make an entangling gate in combination with the Hadamard gate [50]. The other two-qubit gate we consider in this work is the controlled-phase (CZ) gate, written as,

$$CZ = \begin{bmatrix} 1 & 0 & 0 & 0 \\ 0 & 1 & 0 & 0 \\ 0 & 0 & 1 & 0 \\ 0 & 0 & 0 & -1 \end{bmatrix}, \quad (2.7)$$

which will rotate the phase of the second qubit by  $\pi$  if the control qubit is  $|1\rangle$  [50].

### 2.1.3 Mach-Zehnder Interferometer Architecture

To encode unitary matrices on-chip, Chapter 1 outlined that photons can be coupled to waveguide modes using beam splitters and phase shifters as processing components. Beam splitters, as the name implies, route photons between two different waveguide paths and they are often described by a ratio between reflection and transmission R:T. For example, a 100:0 beam splitter will reflect all light, resulting in photons remaining in the same paths. However, a 50:50 beam splitter would equally reflect and transmit photons from each path, splitting the amplitude between paths [49]. Common on-chip beam splitters include directional couplers [51], multi-mode interferometers [52], and inversely designed splitters [53].

Phase shifters, on the other hand, act on only one path, and impart some phase



shift,  $\phi$  on photons such that,

$$|\psi\rangle_{out} = e^{i\phi}|\psi\rangle_{in}, \quad (2.8)$$

where  $|\psi\rangle_{in}$  is the input photon state and  $|\psi\rangle_{out}$  is the output state.

To implement a  $2 \times 2$  unitary on-chip, two phase shifters and two beam splitters can be combined into a Mach-Zehnder interferometer (MZI) [49]. Figure 2.2a shows the basic MZI architecture where we have two 50:50 beam splitters, with one phase shifter in between that controls the amplitude between the output paths, and a phase shifter outside the beam splitters that controls the phase between paths.

To model these MZIs mathematically, transfer matrices for the phase shifters and beam splitters can be combined. For a perfect 50:50 beam splitter we have,

$$50 : 50 = \frac{1}{\sqrt{2}} \begin{bmatrix} 1 & i \\ i & 1 \end{bmatrix}, \quad (2.9)$$

which is a commonly used 50:50 matrix [54]. Similarly, we can write a phase shifter's transfer matrix as,

$$PS = \begin{bmatrix} e^{i\phi} & 0 \\ 0 & 1 \end{bmatrix}, \quad (2.10)$$

where  $\phi$  is the phase shift, and  $PS$  is the matrix with the phase shifter on the upper path, consistent with our MZI model [49]. By combining these transfer matrices

together, we achieve the  $2 \times 2$  MZI as,

$$\begin{aligned} MZI &= \frac{1}{\sqrt{2}} \begin{bmatrix} 1 & i \\ i & 1 \end{bmatrix} \begin{bmatrix} e^{i2\theta} & 0 \\ 0 & 1 \end{bmatrix} \frac{1}{\sqrt{2}} \begin{bmatrix} 1 & i \\ i & 1 \end{bmatrix} \begin{bmatrix} e^{i\phi} & 0 \\ 0 & 1 \end{bmatrix} \\ &= ie^{i\theta} \begin{bmatrix} e^{i\phi}\sin\theta & \cos\theta \\ e^{i\phi}\cos\theta & -\sin\theta \end{bmatrix}. \end{aligned} \quad (2.11)$$

If  $\phi$  spans  $[0, 2\pi]$  and  $2\theta^1$  spans  $[0, \pi]$ , then any  $2 \times 2$  unitary can be achieved through phase shift reconfiguration [49].

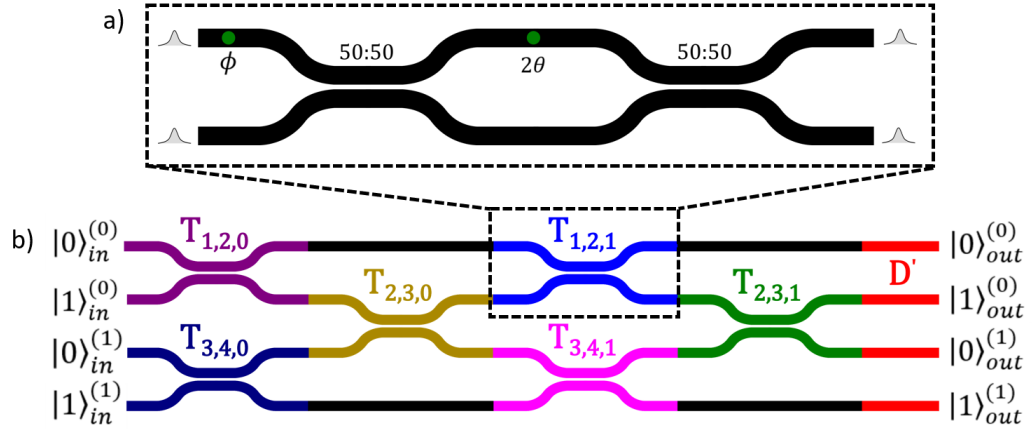


Figure 2.2: The Mach-Zehnder interferometer mesh (MZM) architecture. (a) The ideal  $2 \times 2$  MZI with two 50:50 beam splitters and two phase shifters, represented mathematically by Equation 2.11. (b) A schematic of a two-qubit  $4 \times 4$  rectangular Mach-Zehnder interferometer mesh (MZM). Each  $T_{m,n,p}$  is an MZI, with the colors used to identify each MZI and the  $D'$  global phases.

<sup>1</sup>Note that we use  $2\theta$  instead of  $\theta$  here to simplify the final  $2 \times 2$ , which is standard but unnecessary.

#### 2.1.4 MZI Meshes and Decomposition Procedure

To build MZIs into  $N \times N$  circuits, optical modes must be added, resulting in more MZIs. A method of building any  $N \times N$  using MZIs was first proposed in 1994 [26], where they combined  $N(N-1)/2$  MZIs, where  $N$  is the number of modes in the circuit, into a triangular mesh where you could encode the phases to implement a desired unitary. In 2016, Clements et al. proposed a new rectangular mesh scheme (as shown in Figure 2.2b) that also uses  $N(N-1)/2$  MZIs, which improved loss balance and consequently performance, making it the go-to scheme for current implementations [49]. In this work, we follow the Clements decomposition method to determine the ideal phase shifts in the circuit for a given unitary.

The procedure begins by expanding the  $2 \times 2$  MZI equation shown in Equation 2.11 into the  $N \times N$  matrix,

$$T_{m,n,p} = \begin{bmatrix} 1 & 0 & \dots & \dots & \dots & 0 \\ 0 & \ddots & \dots & \dots & \dots & \vdots \\ \vdots & \dots & ie^{i\theta}e^{i\phi}\sin\theta & ie^{i\theta}\cos\theta & \dots & \vdots \\ \vdots & \dots & ie^{i\theta}e^{i\phi}\cos\theta & -ie^{i\theta}\sin\theta & \dots & \vdots \\ \vdots & \dots & \dots & \dots & \ddots & 0 \\ 0 & \dots & \dots & \dots & 0 & 1 \end{bmatrix}, \quad (2.12)$$

where  $T_{m,n,p}$  is the MZI transmission matrix between modes  $m$  and  $n$ , and  $p$  is the MZI's appearance number from left to right for those two modes (ie. *0th*, *1st*, *2nd*, ...). The decomposition method involves applying  $T_{m,n,p}$ 's to both sides of the desired unitary, choosing them appropriately to null out all the entries underneath the diagonal. If the initial matrix was unitary, this will also correspond to nulling out all entries

above the diagonal, leaving a diagonal global phase matrix at the end. The decomposition steps are the same for any  $N$ , but we show it here for an arbitrary  $4 \times 4$  as an example,

$$\begin{aligned}
 U &= \begin{bmatrix} * & * & * & * \\ * & * & * & * \\ * & * & * & * \\ * & * & * & * \end{bmatrix} \\
 UT_{1,2,0}^{-1} &= \begin{bmatrix} * & * & * & * \\ * & * & * & * \\ * & * & * & * \\ 0 & * & * & * \end{bmatrix} \\
 \tilde{T}_{3,4,1}\tilde{T}_{2,3,1}UT_{1,2,0}^{-1}T_{3,4,0}^{-1}T_{2,3,0}^{-1}T_{1,2,1}^{-1} &= \begin{bmatrix} * & 0 & 0 & 0 \\ 0 & * & 0 & 0 \\ 0 & 0 & * & 0 \\ 0 & 0 & 0 & * \end{bmatrix} \\
 \tilde{T}_{3,4,1}\tilde{T}_{2,3,1}UT_{1,2,0}^{-1}T_{3,4,0}^{-1}T_{2,3,0}^{-1}T_{1,2,1}^{-1} &= D,
 \end{aligned} \tag{2.13}$$

where  $D$  is a diagonal matrix, and the tilde on the left-applied  $T_{m,n,p}$ 's indicate that these are not the MZIs used in the hardware implementation, as they will be changed during the recombination steps [49].

To determine the required phases for these MZIs, we follow the Clements algorithm

as follows. If a  $T_{m,n,p}^{-1}$  is being applied to the RHS, we choose that  $T_{m,n,p}^{-1}$ 's phases as,

$$\begin{aligned}\theta &= \frac{\pi}{2} - \arctan \left( \left| \frac{U_{Null}[x, m]}{U_{Null}[x, n]} \right| \right) \\ \phi &= \pi + \arg \left( \frac{U_{Null}[x, m]}{U_{Null}[x, n]} \right),\end{aligned}\tag{2.14}$$

where  $U_{Null}$  corresponds to the partially decomposed matrix at the current decomposition step, and the index  $x$  is the row index of the element you are trying to nullify.

Conversely, if a  $T_{m,n,p}$  is being applied to the LHS, we choose each phase as,

$$\begin{aligned}\theta &= \frac{\pi}{2} - \arctan \left( \left| \frac{U_{Null}[n, y]}{U_{Null}[m, y]} \right| \right) \\ \phi &= \pi + \arg \left( \frac{U_{Null}[n, y]}{U_{Null}[m, y]} \right),\end{aligned}\tag{2.15}$$

where now the column index  $y$  corresponds to the column of the element you are trying to nullify.

With the unitary decomposed into MZIs and a diagonal phase matrix  $D$ , we can rearrange Equation 2.13 to get the unitary,

$$\begin{aligned}\tilde{T}_{3,4,1}\tilde{T}_{2,3,1}UT_{1,2,0}^{-1}T_{3,4,0}^{-1}T_{2,3,0}^{-1}T_{1,2,1}^{-1} &= D \\ U &= \tilde{T}_{2,3,1}^{-1}\tilde{T}_{3,4,1}^{-1}DT_{1,2,1}T_{2,3,0}T_{3,4,0}T_{1,2,0},\end{aligned}\tag{2.16}$$

where we apply the inverse MZIs to move them to the RHS of the equation. We now have a formula for  $U$ , but it does not correspond to hardware as we still have inverse MZIs in the formula. To remove these, we shift the diagonal matrix to the

left, replacing it and the  $\tilde{T}_{m,n,p}^{-1}$ 's according to,

$$\tilde{T}_{m,n,p}^{-1}D = D_1T_{m,n,p}, \quad (2.17)$$

where  $D_1$  is another diagonal matrix and  $T_{m,n,p}$  is the MZI that corresponds to the hardware implementation. The new phases for  $T_{m,n,p}$ , following the Clements solution are,

$$\begin{aligned} \theta &= \frac{\pi}{2} - \arctan \left( \left| \frac{M[n, m]}{M[n, n]} \right| \right) \\ \phi &= \pi + \angle \frac{M[n, m]}{M[n, n]}, \end{aligned} \quad (2.18)$$

where  $M = \tilde{T}_{m,n,p}^{-1}D$ . From here, we determine the new diagonal matrix as,

$$D_1 = \tilde{T}_{m,n,p}^{-1}DT_{m,n,p}^{-1}. \quad (2.19)$$

By repeating these steps until  $D$  is on the left side of the formula, we get the recombination equation,

$$U = D'T_{2,3,1}T_{3,4,1}T_{1,2,1}T_{2,3,0}T_{3,4,0}T_{1,2,0}, \quad (2.20)$$

where we have relabelled the final diagonal matrix as  $D'$ , which corresponds to global phase shifts we can apply at the end of the MZI mesh. Now, all MZIs can be mapped directly to hardware, with an example  $4 \times 4$  MZM shown in Figure 2.2b.

While this scheme can map any unitary matrix to hardware, it is important to note that it is a linear optical scheme, meaning that non-linear quantum information

processing with multiple photons cannot be done perfectly, unless you include the addition of ancilla (extra) photons to detect, allowing heralded operation [27]. Thus, using this scheme, you cannot create a two-photon CNOT gate with Equation 2.6. Instead, the linear optical unheralded CNOT gate is a circuit with a 1/9 probability of success with the associated unitary matrix,

$$CNOT = \frac{1}{\sqrt{3}} \begin{bmatrix} -1 & \sqrt{2} & 0 & 0 & 0 & 0 \\ \sqrt{2} & 1 & 0 & 0 & 0 & 0 \\ 0 & 0 & -1 & 1 & 1 & 0 \\ 0 & 0 & 1 & 1 & 0 & 1 \\ 0 & 0 & 1 & 0 & 1 & -1 \\ 0 & 0 & 0 & 1 & -1 & -1 \end{bmatrix}, \quad (2.21)$$

where we include 6 modes instead of 4 with an extra vacuum (empty) mode on the top and bottom to account for probabilistic photon routing to those outputs [55]. Similarly, the unheralded CZ gate becomes,

$$CZ = \frac{1}{\sqrt{3}} \begin{bmatrix} -1 & \sqrt{2} & 0 & 0 & 0 & 0 \\ \sqrt{2} & 1 & 0 & 0 & 0 & 0 \\ 0 & 0 & -1 & \sqrt{2} & 0 & 0 \\ 0 & 0 & \sqrt{2} & 1 & 0 & 0 \\ 0 & 0 & 0 & 0 & 1 & \sqrt{2} \\ 0 & 0 & 0 & 0 & \sqrt{2} & -1 \end{bmatrix}, \quad (2.22)$$

where we again have 1/9 success probability and 6 modes instead of the 4 that were shown in Equation 2.7 [56]. The CNOT and CZ are used as examples since we use

them to evaluate our circuits in Chapter 4.

### 2.1.5 Transferring to the Fock Basis for Multi-Qubit Gates

We have now shown that we can map any  $N \times N$  unitary matrix to an on-chip MZM following the Clements procedure, but as mentioned, multi-qubit gates become probabilistic with this scheme. Thus, if we want to evaluate a multi-qubit gate on input/output states using a mathematical model, we require a transformation into the Fock state basis, composed of the states  $\{|0\rangle, |1\rangle, |2\rangle, \dots, |n\rangle\}$ , where  $n$  is the number of photons you send into the circuit. This is required since it is possible for multiple photons to be routed to the same output, which is not handled in the Z-basis. To transform a unitary into the Fock basis, we calculate the matrix permanent of a unitary, mapping it to a larger dimensional space that accounts for all possible locations for input and output photons. This transformation scheme was first proposed in 2014 by Aaronson and Arkhipov [57], and calculating matrix permanents is a computationally complex problem that has become a popular application for showing quantum advantage [2]. Here, to compute this, we use code based on this approach that has previously been written in our group.

As an example, the  $6 \times 6$  unheralded CNOT or CZ with two input photons converted to the Fock basis results in an input/output basis of  $\{|2, 0, 0, 0, 0, 0\rangle, |0, 2, 0, 0, 0, 0\rangle, \dots, |1, 1, 0, 0, 0, 0\rangle, \dots, |0, 0, 0, 0, 0, 2\rangle\}$ , so calculating the matrix permanent transforms them into  $21 \times 21$  transfer matrices.



## 2.2 Nanophotonic Imperfections

While theoretically we can implement any  $N \times N$  unitary matrix on-chip, performance and scalability are often limited by hardware imperfections. Thus, we must include these imperfections when evaluating our simulated circuits. In nanophotonics there are two main imperfections that must be accounted for; beam splitter error and loss.

### 2.2.1 Beam Splitter Error

Beam splitter error in MZMs is an imperfection associated with having unequal reflection and transmission such as 47:53 or 51:49, instead of the ideal 50:50. To model this imperfection in our transfer matrices, we replace the ideal beam splitter matrices, as shown in Equation 2.9, with the matrix;

$$BS = \begin{bmatrix} \sqrt{r} & i\sqrt{1-r} \\ i\sqrt{1-r} & \sqrt{r} \end{bmatrix}, \quad (2.23)$$

where  $r$  is the reflection coefficient for the beam splitter (BS). To model this in simulation, we take a central value of 50% reflectivity, and sample from a normal distribution with some standard deviation on the reflectivity of  $\sigma_r$  to mimic fabrication imperfections. Existing implementations of MZM circuits have demonstrated beam splitter standard deviations from 0.2% to 5% [58, 59, 60, 61, 52, 62].

### 2.2.2 Nanophotonic Loss

Loss is the measure of photons that do not reach the output of the circuit as they scatter out of the waveguides or are absorbed. More specifically, nanophotonic loss is the portion of loss that comes from photon propagation within waveguides, beam

splitters, and usually phase shifters, though in our model phase shifter loss is not included in this since this comes from the quantum dots instead of nanophotonics. Many implementations characterize the loss of each component [61, 62, 63], and others use a simpler model of a loss value per MZI. For this work, we deem it sufficient to it as model loss per MZI, since we are performing a general implementation and do not specify the hardware specifications for our design. To model the nanophotonic loss per MZI, we assume a balanced loss in both paths, which is a good assumption since lengths will be the same in each path and since MZIs are small their proximity during fabrication should lead to similar imperfections in each path. This allows us to apply the loss matrix,

$$Loss = \begin{bmatrix} \sqrt{1-L} & 0 \\ 0 & \sqrt{1-L} \end{bmatrix}, \quad (2.24)$$

to the RHS of the  $2 \times 2$  MZI equation, where  $L$  is the nanophotonic loss for each MZI. Existing MZM implementations range in loss per MZI of 1% to 30% [63, 62, 64, 65].

## 2.3 MZM Optimization

### 2.3.1 Methods of Measuring Mesh Accuracy

By adjusting the tunable phase shifters in MZMs, optimization can be performed to reduce hardware imperfections, improving the performance of QPICs. However, this requires a method of measuring the error in the circuit. A common method is with

matrix fidelity [66, 49, 38], calculated as,

$$\mathcal{F}(U_{exp}, U) = \left| \frac{tr(U^\dagger U_{exp})}{\sqrt{N tr(U_{exp}^\dagger U_{exp})}} \right|^2, \quad (2.25)$$

where  $U$  is the target unitary matrix,  $U_{exp}$  is the circuit transfer matrix with losses and errors,  $N$  is the number of modes in the circuit, and  $\mathcal{F}$  is the transfer matrix fidelity, measured on a scale of 0, for the worst possible circuit, to 1 for the perfect circuit [49]. This fidelity calculation is normalized to exclude balanced losses, as the balanced loss will only affect the count rate, and it is often more useful to determine how accurate the circuit is when photons are detected at the outputs. This error can also be modeled as infidelity,

$$\mathcal{I}(U_{exp}, U) = 1 - \mathcal{F}(U_{exp}, U), \quad (2.26)$$

which is the opposite of fidelity, where 0 would be the perfect circuit, and 1 is the worst possible circuit.

Circuit accuracy can also be measured globally using mean squared error (MSE) between matrices [67, 68], or with local accuracy based on relative error per MZI [59]. When the circuit has a specific task, such as implementing a quantum optical neural network, accuracy can also be based on its performance accuracy [69].

Output state fidelity is also commonly used, as it is easier to characterize in hardware, where instead of characterizing every component to determine the imperfect matrix, the experimental and ideal output states can be compared to judge a circuit's performance. This can be measured through the projection of the experimental

output state onto the ideal state, which we call the unconditional output fidelity, written as,

$$\mathcal{F}_i^{(unc)} = \left| \left\langle \psi_{out}^{(i)} | U_{exp} | \psi_{in}^{(i)} \right\rangle \right|^2, \quad (2.27)$$

where  $|\psi_{in}^{(i)}\rangle$  and  $\langle\psi_{out}^{(i)}|$  are an arbitrary input-output pair, and  $\mathcal{F}_i^{(unc)}$  is the unconditional fidelity for that pair. This can be extended to a total unconditional fidelity by averaging over all input-output pairs, calculated as,

$$\mathcal{F}^{(unc)} = \frac{1}{K} \sum_{i=1}^K \mathcal{F}_i^{(unc)}, \quad (2.28)$$

where  $K$  is the number of input-output pairs in the system [62]. We can also precondition the system such that the fidelity depends only on the cases where photons provide a valid logical output for the circuit, which can be done by first truncating each expected output state down to the computational basis and re-normalizing them. This results in,

$$|\psi_{out}^{(i,con)}\rangle = \frac{|\psi_{out}^{(i,cb)}\rangle}{\sqrt{\left| \left\langle \psi_{out}^{(i,cb)} | \psi_{out}^{(i,cb)} \right\rangle \right|^2}}, \quad (2.29)$$

where  $|\psi_{out}^{(i,con)}\rangle$  is the expected conditional output state, and  $cb$  indicates the computational basis. If we then perform a re-normalization of the experimental output state in the computational basis using the same formula, we get a  $|\psi_{out,exp}^{(i,con)}\rangle$ , representing our conditional experimental output state, and can then find the conditional output

state infidelity using the equation,

$$\mathcal{I}_i^{(con)} = 1 - \left| \left\langle \psi_{out}^{(i,con)} | \psi_{out,exp}^{(i,con)} \right\rangle \right|^2, \quad (2.30)$$

which can again be averaged over all computational basis input-output pairs to determine the conditional infidelity,  $\mathcal{I}^{(con)}$ . An example of this is on the unheralded CNOT and CZ, where you can find the conditional infidelity on the computational basis of  $\{|00\rangle, |01\rangle, |10\rangle, |11\rangle\}$ . Other methods of measuring output state accuracy have also been used such as using a Hilbert-Schmidt inner product as fidelity [61].

### 2.3.2 Common Optimization Methods

While many methods have been used to optimize MZMs, it has become a mainstay for architecture proposals to add extra tunable components to meshes to improve optimization. For example, increasing mesh size with redundant tunable layers can both speed up and improve optimization with a gradient-descent-based global optimization, with MSE as cost [67]. Similarly, if you use two MZIs for each functional MZI in the mesh, known as a double MZI (DMZI) architecture, you can perfectly correct from beam splitter errors of 85:15 to 15:85. This uses a self-configuration algorithm using a feedback loop where nearly-transparent detectors can sample the power of both MZI outputs, the inner phase shifter can be chosen to create what should be the cross and bar states, and the other phases can be adjusted until these states are met, making the DMZI represent a perfect MZI assuming no loss [70, 71]. Similarly, it has been shown that adding two redundant phase shifters at the output port of each MZI allows you to follow an algorithm to minimize the relative error per MZI, optimizing the circuit [59]. Other optimization methods have also been used such as numerical

non-linear local optimization on each MZI [61]. Hardware implementations will also often avoid additional redundant components allowing simpler implementation, but will reduce their error by characterizing and adjusting their MZIs one at a time to be as close to the desired unitary as possible [65, 38, 39].

### 2.3.3 Our Optimization Methods

In this work, due to the current complications of implementing multiple quantum dots on-chip (see Chapter 3), we chose not to add any redundant components to the MZIs. Instead, our goal was to determine the possible performance of the simplest implementation of these circuits. For determining circuit accuracy, we use matrix infidelity as shown in Equation 2.26, which we use to remove balanced losses as we want to characterize the circuit’s accuracy, not count rate. Similarly, we also use the post-selected conditional output infidelity as shown in Equation 2.30 in Chapter 4 to evaluate the CNOT and CZ gates.

Using these circuit accuracy equations as cost functions, we performed our optimization using the local gradient-free BOBYQA non-linear numerical optimization algorithm [72], as implemented in Python’s NLOpt library [73]. This optimization algorithm was used because it avoids the need for gradient calculation, it is fast, and it is built for well-constrained problems, which is perfect for the constrained phase shifts in the system. To optimize, BOBYQA performs a quadratic approximation to the given cost function, and has shown impressive results for optimizing up to 320 variables at once with robustness to local minima [72].

To begin, we optimized on each MZI in the mesh one by one, calculating the matrix infidelity between the imperfect and ideal  $2 \times 2$ . This was a natural choice

since the Clements decomposition, shown in Section 2.1.4, breaks the unitary down to the ideal  $2 \times 2$  MZIs, naturally suggesting local optimization. Optimizing each gate locally has also been done successfully with other optimization methods [59]. Additionally, it only requires  $N(N-1)/2$  optimizations of two parameters, instead of many variable optimizations that are more computationally intensive. However, when we simulated this method we did not achieve the desired results. While it optimized the accuracy of each  $2 \times 2$  locally, it did not always reduce the infidelity of the overall circuit, since the interactions between MZIs were not accounted for. Figure 2.3 shows optimization on beam splitter loss per MZI for one random unitary for  $N = 2, 6, 10$  circuits. While  $N = 2$  will always optimize or match the imperfect, its clear from the figure that that is not the case for larger circuits.

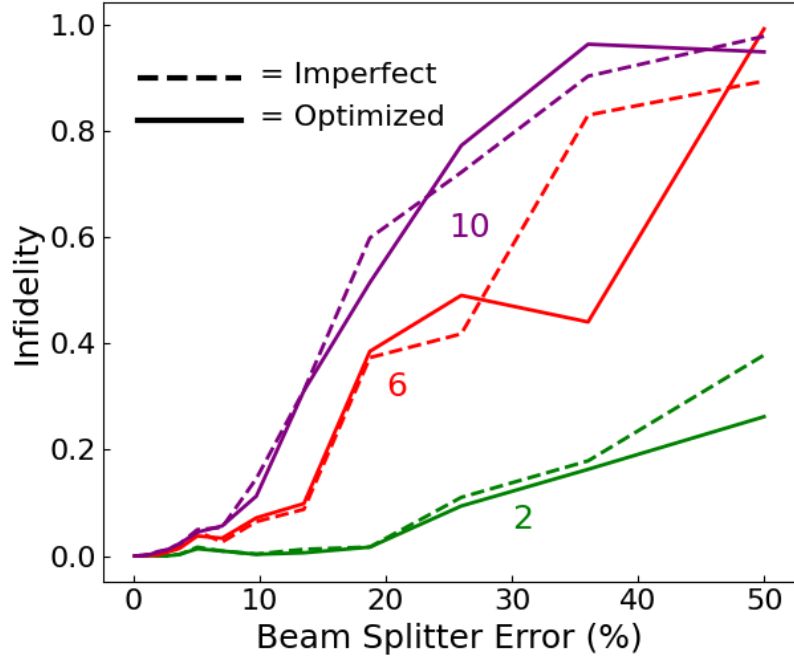


Figure 2.3: Local MZI mesh optimization results for one random unitary of sizes  $N = 2$  (green),  $N = 6$  (red),  $N = 10$  (purple) with beam splitter error ranging from 0% to 50%

Thus, we instead used a global optimization, where the cost was taken as the infidelity of the overall circuit (Equation 2.26), and all MZI phases were set as parameters. This is the first time, to our knowledge, that a global matrix infidelity optimization has been performed using the BOBYQA optimizer. To do this, we began by determining the phase shifts for a given unitary in the ideal case using the Clements decomposition method outlined in Section 2.1.4. Then, imperfections were added to the circuit to calculate the “imperfect” unitary and its associated infidelity. For optimization, the ideal phases were chosen as initial phase guesses, with phase constraints of  $[-\pi, \pi]$  as determined by the quantum dot phase shifters in Chapter 3. Optimization convergence requirements are covered in Section B.2. This approach, as shown in Chapter 4, provided significant performance improvements.

Note that in our optimizations, the global phases in  $D'$  were all separately optimized to match their ideal global phases, since each of these phases are independent from the rest of the circuit. This optimization was performed using the Scipy optimization library [74], using their minimize function, which uses the Broyden-Fletcher-Goldfarb-Shanno algorithm. Future work could implement these global phases into the global optimization, but time constraints did not allow for that in this work.



## Chapter 3

### Quantum Dots as Phase Shifters

#### 3.1 Quantum Dots and Light-Matter Interactions

Quantum electrodynamical (QED) systems, with the interactions between single photons and quantum emitters, have become a promising QPIC source platform due to the ability to generate indistinguishable single photons that can be used as qubits [75, 76]. These quantum emitters, in a broad sense, can be described as a two-level system (TLS) with a ground state  $|g\rangle$  and an excited state  $|e\rangle$ . Shining light on these emitters allows you to drive them into the excited state, causing them to spontaneously emit single photons [41], as shown in Figure 3.1.

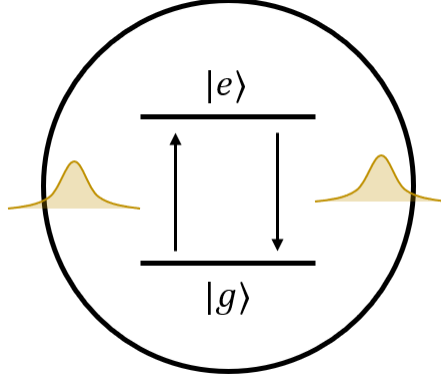


Figure 3.1: Quantum emitter two-level system (TLS) coupled to a light field. The TLS can be excited into  $|e\rangle$  by photons, and then will spontaneously decay back to its ground state  $|g\rangle$ , emitting photons.

Ever since the discovery in 1994 [77] that single self-assembled quantum dots (QDs) photoluminesce, these man-made semiconductor atoms have become popular quantum emitters due to the ability to engineer their optical properties during growth [41]. QDs are often used as single photon sources because they are bright, and can emit pure, indistinguishable, coherent single photons [78]. A QD's excitation and emission comes from an electron-hole pair between the conduction and valence band of the semiconductor, known as an exciton, which can be neutral, or charged if they are bound to an additional electron or hole [79]. Quantum dots have an exciton in each planar direction, where their interaction with an electric field can be modeled by transition dipoles,  $\hat{d}$ , which are linear (ie.  $\hat{d} = \hat{x}, \hat{y}$ ) for a neutral exciton and circular (ie.  $\hat{d} = \hat{\sigma}_+, \hat{\sigma}_-$ ) for a charged exciton [80].

Quantum dots are fabricated using molecular-beam epitaxy and other epitaxial methods, which deposit thin crystal films onto substrates [81]. The most popular and successful method of growing quantum dots is the Stranski-Krastanov method, which is a method where quantum dots will grow randomly across the substrate in a process

called self-assembly [82, 83]. This is commonly done using InGaAs or InAs quantum dots on a GaAs substrate, but methods using InP have been rising in popularity since they emit at 1500 nm telecom wavelength [84, 85]. Fabrication parameters allow for control over the density of the self-assembled QDs across the surface, as well as the sizing of the QDs, allowing height variations from 1 – 10 nm and in-plane widths of 10 – 70 nm [41, 86, 83]. The control over these parameters also affects the resonant wavelength of the quantum dots, allowing you to control the emission wavelength. The drawback is that due to the random nature of this self-assembly, only some QDs will be adequate for the required application. Additionally, if you are coupling quantum dots to nanophotonic systems, the coupling will heavily depend on the location of the good quality QDs. This makes large-scale QPICs with many QDs difficult to implement due to the randomness of finding good QDs in the right locations.

Other newer methods of QD growth include droplet epitaxy, which allows for more uniform growth and better control over growth parameters [87, 84], as well as site-selected quantum dot growth, where the growth location can be selected, solving the random placement issue at the cost of QD quality [88]. Site-selected QD growth is a promising technology for developing the large-scale QPICs with embedded QDs that we discuss here, assuming fabrication imperfections can be improved.

### 3.2 Quantum Dots Embedded in a Waveguide

The goal of this section is to step through the mathematical model for the light-matter interaction between a light field and a quantum dot coupled to a waveguide. We will see that we can derive a scattered field that arises from the interaction that

will impart a phase shift on the light, which we will use in this work for phase shifters in MZM circuits.

### 3.2.1 Mathematical Model of a Two-Level System

A common method of modeling the interaction between a light field and a quantum emitter's TLS is with the Jaynes-Cummings Hamiltonian [89] in the Schrodinger picture,

$$\hat{H}_S = \hbar\omega_A \hat{\sigma}_{eg} \hat{\sigma}_{ge} + \int d^3r \int_0^\infty d\omega \hbar\omega \hat{f}^\dagger(r, \omega) \hat{f}(r, \omega) - \hat{d} \cdot \hat{E}(r, \omega), \quad (3.1)$$

where the first term describes the TLS, where  $\hat{\sigma}_{ij} = |i\rangle\langle j|$  is the atomic transition operator, and  $\hbar\omega_A$  is the transition energy. The second term describes the free light field, where  $\hat{f}^\dagger$  and  $\hat{f}$  are the bosonic creation and annihilation operators in a nanophotonic light-matter system. They are similar, but distinctly different than the field operators  $\hat{a}^\dagger$  and  $\hat{a}$  since they have a material component from the possibility of dispersion or absorption in the material. The third term describes the system's light-matter interaction, using the relation between the transition dipole operator  $\hat{d}$  and the electric field operator  $\hat{E}$  evaluated at some point  $r$  in the waveguide for a frequency  $\omega$ .

The bosonic operators can be represented in the number basis as,

$$\hat{f}^\dagger(r, \omega) = \sum_n \sqrt{n(r, \omega) + 1} |n(r, \omega) + 1\rangle \langle n(r, \omega)| \quad (3.2)$$

$$\hat{f}(r, \omega) = \sum_n \sqrt{n(r, \omega)} |n(r, \omega) - 1\rangle \langle n(r, \omega)|, \quad (3.3)$$

where we are assuming here that we are considering a single-mode waveguide, and

where photon number  $n$  is evaluated at the location  $r$  for a frequency  $\omega$ .

The dipole transition operator can be written using the atomic transition operators as,

$$\hat{d} = d^* \hat{\sigma}_{eg} + d \hat{\sigma}_{ge}, \quad (3.4)$$

where  $d = \langle g | \hat{d} | e \rangle$  is the transition dipole moment. As expected, this contains both the transition from ground to excited state, and the reverse.

### 3.2.2 Embedding the Emitter in a Waveguide

Now, we consider the case where all photons have the same angular frequency  $\omega_P$  in a simple nanophotonic rectangular waveguide, allowing us to simplify to a one-dimensional model. If we expand the interaction term with Equation 3.4, this allows us to rewrite the Hamiltonian as,

$$\hat{H}_S = \hbar\omega_A \hat{\sigma}_{eg} \hat{\sigma}_{ge} + \hbar\omega_P \hat{f}^\dagger \hat{f} - (d^* \hat{\sigma}_{eg} + d \hat{\sigma}_{ge}) \cdot (\hat{E}^+ + \hat{E}^-), \quad (3.5)$$

where here we also write the electric field as,

$$\hat{E} = \hat{E}^+ + \hat{E}^-, \quad (3.6)$$

where the positive frequency component  $\hat{E}^+$  depends on  $\hat{f}$  and the negative frequency component  $\hat{E}^-$ , depends on  $\hat{f}^\dagger$ . Note that henceforth we omit the  $r$  and  $\omega$  dependence for the bosonic operators for clarity.

If we split the Hamiltonian into its non-interacting,  $\hat{H}_0$ , and interacting,  $\hat{H}_{int}$ ,

terms we have,

$$\hat{H}_0 = \hbar\omega_A \hat{\sigma}_{eg} \hat{\sigma}_{ge} + \hbar\omega_P \hat{f}^\dagger \hat{f}, \quad (3.7)$$

$$\hat{H}_{int} = -(d^* \cdot \hat{E}^+ \hat{\sigma}_{eg} + d^* \cdot \hat{E}^- \hat{\sigma}_{eg} + d \cdot \hat{E}^+ \hat{\sigma}_{ge} + d \cdot \hat{E}^- \hat{\sigma}_{ge}), \quad (3.8)$$

where we are able to swap the order of the field and atomic operators since they act on different Hilbert spaces and thus commute. However, this interaction term is complex and difficult to solve, so to simplify it we move into the interaction picture, which will allow us to apply the rotating wave approximation.

### 3.2.3 Moving into the Interaction Picture

To convert the Hamiltonian to the interaction picture we require the time evolution operator,

$$\hat{U} = \exp\left[-\frac{i}{\hbar} \hat{H}_0 t\right], \quad (3.9)$$

which we can use to transform any operator into the interaction picture using,

$$\hat{O}_I = \hat{U}^\dagger \hat{O} \hat{U}. \quad (3.10)$$

To simplify the conversion, we can define separate evolution operators for the non-interacting emitter and light field terms since their states are in different Hilbert spaces. The emitter evolution gives us,

$$\begin{aligned} \hat{U}_A &= \exp\left[-\frac{i}{\hbar} \hat{H}_{0A} t\right] \\ &= |g\rangle\langle g| + \exp(-i\omega_A t) |e\rangle\langle e|. \end{aligned} \quad (3.11)$$

Similarly, we can determine the light field evolution operator as,

$$\begin{aligned}\hat{U}_P &= \exp\left[-\frac{i}{\hbar}\hat{H}_{0_P}t\right] \\ &= \exp\left[-i\omega_P t \sum_n n|n\rangle\langle n|\right].\end{aligned}\tag{3.12}$$

For a more detailed derivation, see Section A.1. Equipped with the evolution operators, we can determine the atomic and bosonic operators in the interaction picture.

For the atomic operators we have,

$$\begin{aligned}\hat{\sigma}_{eg,I} &= \hat{U}_A^\dagger \hat{\sigma}_{eg} \hat{U}_A \\ &= [|g\rangle\langle g| + \exp(i\omega_A t)|e\rangle\langle e|]|e\rangle\langle g| + \exp(-i\omega_A t)|e\rangle\langle e|] \\ &= \exp(i\omega_A t)|e\rangle\langle g| \\ &= \exp(i\omega_A t)\hat{\sigma}_{eg},\end{aligned}\tag{3.13}$$

and,

$$\begin{aligned}\hat{\sigma}_{ge,I} &= \hat{\sigma}_{eg,I}^\dagger \\ &= \exp(-i\omega_A t)\hat{\sigma}_{eg}^\dagger \\ &= \exp(-i\omega_A t)\hat{\sigma}_{ge},\end{aligned}\tag{3.14}$$

where we label operators with a subscript  $I$  in the interaction picture. The bosonic operators experience a similar result, as shown here by the derivation of  $\hat{f}_I$ ,

$$\begin{aligned}
\hat{f}_I &= \hat{U}_P^\dagger \hat{f} \hat{U}_P \\
&= \exp[i\omega_P t (\sum_n n |n\rangle\langle n|)] \sum_{n'} \sqrt{n'} |n' - 1\rangle\langle n'| \exp[-i\omega_P t (\sum_{n''} n'' |n''\rangle\langle n''|)]. \quad (3.15) \\
&= \sum_n \sum_{n'} \sum_{n''} \sqrt{n'} \exp[i\omega_P t n] |n\rangle\langle n| n' - 1\rangle\langle n'| n''\rangle\langle n''| \exp[-i\omega_P t n''].
\end{aligned}$$

Equation 3.15 is 0 unless  $n = n' - 1$  and  $n' = n''$ . So, we can write the whole equation in terms of  $n'$  as,

$$\begin{aligned}
\hat{f}_I &= \sum_{n'} \sqrt{n'} \exp[i\omega_P t (n' - 1)] |n'\rangle\langle n' - 1| n' - 1\rangle\langle n'| n'\rangle\langle n'| \exp[-i\omega_P t n'] \\
&= \sum_{n'} \sqrt{n'} \exp[-i\omega_P t] |n'\rangle\langle n'| \quad (3.16) \\
&= \exp(-i\omega_P t) \hat{f}.
\end{aligned}$$

Through the same steps, you can find that,

$$\hat{f}_I^\dagger = \exp(i\omega_P t) \hat{f}^\dagger. \quad (3.17)$$

Now we have all operators except the electric field in the interaction picture, which we must now derive.



### 3.2.4 Electric Field Derivation

To determine the electric field operator, we begin with the volume integral equation [90],

$$\hat{E}^+(r, \omega) = i\omega\mu_0\mu \int_{V'} \overleftrightarrow{G}(r, r') \cdot \hat{j}(r') dV', \quad (3.18)$$

where Green's tensor  $\overleftrightarrow{G}$  is the solution for the electric field operator for a point source. Green's tensor describes the way the electric field evolves as it travels from  $r'$  to  $r$ .  $\hat{j}$  is the current density, which must be defined to determine the electric field operator. In Section A.2, we go through the steps behind solving the current density, resulting in an electric field operator  $\hat{E}^+$  of,

$$\begin{aligned} \hat{E}^+(r, \omega) &= i\omega\mu_0\mu \int_{V'} \overleftrightarrow{G}(r, r') \hat{j}(r') dV' \\ &= i\omega\mu_0\mu \int_{V'} \overleftrightarrow{G}(r, r') \omega \sqrt{\frac{\hbar}{\pi} \epsilon_0 \epsilon_I(r', \omega)} \hat{f}(r', \omega) dV' \\ &= i\omega^2\mu_0 \sqrt{\frac{\hbar}{\pi} \epsilon_0} \int_{-\infty}^{\infty} dr' \sqrt{\epsilon_I(r', \omega)} \overleftrightarrow{G}(r, r') \hat{f}(r', \omega), \end{aligned} \quad (3.19)$$

where we assume  $\mu = 1$  and the volume integral becomes an integral over the horizontal location in the waveguide. This equation essentially tells us that the electric field at some point  $r$  in the waveguide is made up of the sum of all the excitations at all points  $r'$  propagated back to  $r$ . The same steps can be taken to find  $\hat{E}^-$ , resulting in,

$$\hat{E}^-(r, \omega) = -i\omega^2\mu_0 \sqrt{\frac{\hbar}{\pi} \epsilon_0} \int_{-\infty}^{\infty} dr' \sqrt{\epsilon_I(r', \omega)} \overleftrightarrow{G}^*(r, r') \hat{f}^\dagger(r', \omega). \quad (3.20)$$

### 3.2.5 The Rotating Wave Approximation

With equations for the electric field operators, we now return to the interaction picture to apply the rotating wave approximation to simplify the Hamiltonian. Equations 3.19 and 3.20 only depend on the bosonic operators, and we know how they transform in the interaction picture, resulting in,

$$\begin{aligned}\hat{E}_I^+(r, \omega) &= e^{-i\omega_P t} \hat{E}^+, \\ \hat{E}_I^-(r, \omega) &= e^{i\omega_P t} \hat{E}^-, \end{aligned}\tag{3.21}$$

making the interacting part of the Hamiltonian,

$$\begin{aligned}\hat{H}_{int,I} &= -[(d^* \cdot \hat{E}_I^+ e^{-i\omega_P t} + d^* \cdot \hat{E}_I^- e^{i\omega_P t}) \hat{\sigma}_{eg,I} e^{i\omega_A t} + (d \cdot \hat{E}_I^+ e^{-i\omega_P t} + d \cdot \hat{E}_I^- e^{i\omega_P t}) \hat{\sigma}_{ge,I} e^{-i\omega_A t}] \\ &= -[(d^* \cdot \hat{E}_I^+ e^{i(\omega_A - \omega_P)t} + d^* \cdot \hat{E}_I^- e^{i(\omega_A + \omega_P)t}) \hat{\sigma}_{eg,I} \\ &\quad + (d \cdot \hat{E}_I^+ e^{-i(\omega_A + \omega_P)t} + d \cdot \hat{E}_I^- e^{-i(\omega_A - \omega_P)t}) \hat{\sigma}_{ge,I}].\end{aligned}\tag{3.22}$$

This equation does not have a simple solution, but it can be simplified by making the rotating wave approximation (RWA). In this equation, we see two different types of terms. We have the terms that evolve with  $\omega_A + \omega_P$  that have very fast oscillations over time, and we have terms that evolve with  $\omega_A - \omega_P$ , which oscillate slowly over time. The RWA assumes that the fast oscillations are so much faster than our system that they average out and can be ignored. Thus, those terms disappear from the Hamiltonian and we are left with,

$$\hat{H}_{int,I} \approx -[(d^* \cdot \hat{E}_I^+ e^{i(\omega_A - \omega_P)t}) \hat{\sigma}_{eg,I} + (d \cdot \hat{E}_I^- e^{-i(\omega_A - \omega_P)t}) \hat{\sigma}_{ge,I}],\tag{3.23}$$

which is of a simpler form that can be solved. Now, with this simplification, we return to the Schrodinger picture for the rest of this work, and write the overall Hamiltonian as,

$$\hat{H}_S = \hbar\omega_A\hat{\sigma}_{eg}\hat{\sigma}_{ge} + \hbar\omega_P\hat{f}^\dagger\hat{f} - \left[(d^* \cdot \hat{E}^+)\hat{\sigma}_{eg} + (d \cdot \hat{E}^-)\hat{\sigma}_{ge}\right]. \quad (3.24)$$

### 3.2.6 Deriving the Scattered Field from the Emitter

We next want to look at how our field is affected over time, to determine the interactions with the emitter. To do this, we use the Heisenberg equation of motion and derive the equations for the bosonic operators over time, using  $\hat{f}$  as an example here,

$$\begin{aligned} \dot{\hat{f}}(r, \omega_P) &= \frac{i}{\hbar} \left[ \hat{H}, \hat{f}(r, \omega_P) \right] \\ &= \frac{i}{\hbar} \left[ \hbar\omega_A\hat{\sigma}_{eg}\hat{\sigma}_{ge} + \hbar\omega_P\hat{f}^\dagger\hat{f} - \left[(d^* \cdot \hat{E}^+)\hat{\sigma}_{eg} + (d \cdot \hat{E}^-)\hat{\sigma}_{ge}\right], \hat{f}_L(r, \omega_P) \right]. \end{aligned} \quad (3.25)$$

Here we derive each term of this commutator one at a time, which can be seen in Section A.4. From these results, we solve Equation 3.25 as,

$$\dot{\hat{f}}(r, \omega_P) = -i\omega_P\hat{f}(r, \omega_P) + \omega_P^2\mu_0\sqrt{\frac{\hbar}{\pi}\epsilon_0}d(r_A)\sqrt{\epsilon_I(r, \omega_P)}\overleftrightarrow{G}^*(r_A, r, \omega_P)\hat{\sigma}_{ge}. \quad (3.26)$$

Now, we can formally integrate Equation 3.26 from some initial time  $t'$  to  $t$ , resulting in [91],

$$\begin{aligned} \hat{f}(r, \omega_P, t) &= \hat{f}(r, \omega_P, t') \exp(-i\omega_P(t - t')) + \\ &\quad \omega_P^2\mu_0\sqrt{\frac{\hbar}{\pi}\epsilon_0} \int_0^t dt' d(r_A)\sqrt{\epsilon_I(r, \omega_P)}\overleftrightarrow{G}^*(r_A, r, \omega_P)\hat{\sigma}_{ge}(t')e^{-i\omega_P(t-t')}. \end{aligned} \quad (3.27)$$

Here we see the bosonic operator is defined by two terms, the first term describes a free excitation in the system, coming from the initial field and not interacting with the emitter, and the second term coming from interactions with the emitter (as is clear from the  $\hat{\sigma}_{ge}$ ), either through a scattering event, representing a virtual transition, or through a decay from excited to ground state. We will call the electric field from the first term the incident field  $\hat{E}_P^+$ , and the field from the second term the scattered field,  $\hat{E}_S^+$ , allowing us to write the field as,

$$\hat{E}^+ = \hat{E}_P^+ + \hat{E}_S^+. \quad (3.28)$$

Note that when the light interacts with the emitter, or quantum dot in our case, the scattering can cause it to change direction. However, the free field that does not interact will travel through. This is shown in Figure 3.2, depicting the initial and scattered field for light interacting with an emitter in a waveguide. This figure also includes a  $\hat{E}_{Loss}^+$ , which is the portion that is lost from the waveguide.

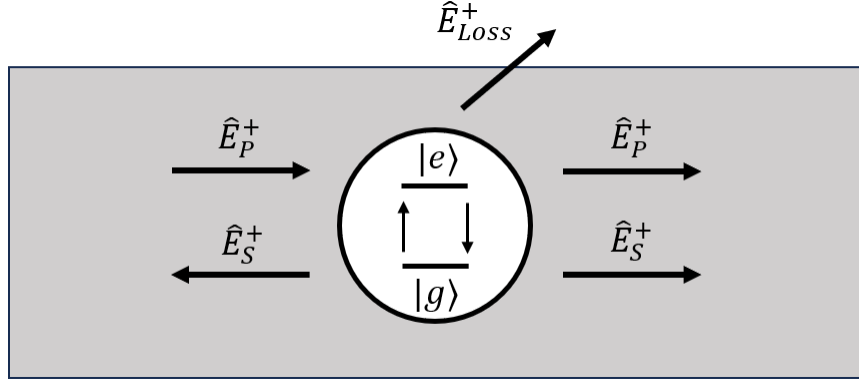


Figure 3.2: Initial and scattered positive frequency field for a quantum dot in a waveguide. This example shows the incident field coming from the left and going through without interaction, with the scattered field both reflecting and transmitting. A loss term is also included for light that is lost from the waveguide from the interaction.

Since all the reflected light is scattered light, we can determine the transmission coefficient as,

$$t = \frac{\langle \hat{E}^+ \rangle}{\langle \hat{E}_P^+ \rangle}, \quad (3.29)$$

and the reflection coefficient as,

$$r = \frac{\langle \hat{E}_S^+ \rangle}{\langle \hat{E}_P^+ \rangle}. \quad (3.30)$$

The transmission coefficient calculated from Equation 3.29, will contain phase shift information between the incident and transmitted light, allowing us to determine the phase shift on the light from the interaction with the emitter, calculated as,

$$\phi = \arg(t), \quad (3.31)$$

where  $\phi$  is the phase shift on the light field.

Thus, we now have a method to determine the phase shift, but the electric field still must be determined. Note that since the transmission and reflection coefficients are written relative to the incident field, instead of determining the incident field we can write the scattered field in terms of it. To determine the scattered field, we begin with the Green's tensor identity [90],

$$\frac{\omega^2}{c^2} \int_{-\infty}^{\infty} ds \epsilon_I(s, \omega) G(r, s, \omega) G^*(r', s, \omega) = \text{Im} G(r, r', \omega), \quad (3.32)$$

allowing us to combine Equation 3.19 and the second term of Equation 3.27 to write the scattered field as,

$$\hat{E}_S^+(r, \omega_P, t) = \frac{i\mu_0\omega_P^2}{\pi} \text{Im} G(r, r_A, \omega_P) d(r_A) \int_0^t dt' \hat{\sigma}_{eg}(t') e^{-i\omega_P(t-t')}. \quad (3.33)$$

Now we begin by solving the time integral by introducing the slowly varying atomic operator  $\tilde{\sigma}_{ge}(t) = \hat{\sigma}_{ge}(t) e^{i\omega_A t}$ , allowing us to rewrite the time integral as,

$$\int_0^t dt' \hat{\sigma}_{eg}(t') e^{-i\omega_P(t-t')} = \int_0^t dt' \tilde{\sigma}_{ge}(t') e^{-i\omega_A t'} e^{-i\omega_P(t-t')}. \quad (3.34)$$

We then remove the slowly varying atomic operator from the integral using the Markov approximation that  $\tilde{\sigma}_{ge}(t') \approx \tilde{\sigma}_{ge}(t)$  resulting in,

$$\int_0^t dt' \tilde{\sigma}_{ge}(t') e^{-i\omega_A t'} e^{-i\omega_P(t-t')} = \tilde{\sigma}_{ge}(t) \int_0^t dt' e^{-i(\omega_P - \omega_A)(t-t')}, \quad (3.35)$$

where we multiplied and divided by  $e^{-i\omega_A t}$  to recover the original operator. This

integral is easily solved by separating it into a delta function and the Principle part with the identity;

$$\int_0^t dt' e^{-i(\omega_P - \omega_A)(t-t')} = \pi \delta(\omega_P - \omega_A) - i\mathcal{P} \left\{ \frac{1}{\omega_P - \omega_A} \right\}, \quad (3.36)$$

allowing the scattered field to be written as,

$$\begin{aligned} \hat{E}_S^+(r, \omega_P, t) &= i\mu_0\omega_P^2 \text{Im}G(r, r_A, \omega_P) \cdot d(r_A) \hat{\sigma}_{ge}(t) \delta(\omega_P - \omega_A) \\ &+ \frac{\mu_0}{\pi} \mathcal{P} \left\{ \frac{\omega_P^2 \text{Im}G(r, r_A, \omega_P) \cdot d}{\omega_P - \omega_A} \right\} \hat{\sigma}_{ge}(t). \end{aligned} \quad (3.37)$$

We want the overall field at a point  $r$  for a time  $t$ , not the field for only one frequency, so we integrate across all frequencies for both the scattered and incident fields to determine the total positive frequency components of the fields,

$$\hat{E}_P^+(r, t) = \int_0^\infty d\omega \hat{E}_P^+(r, \omega, t), \quad (3.38)$$

$$\hat{E}_S^+(r, t) = \int_0^\infty d\omega \hat{E}_S^+(r, \omega, t). \quad (3.39)$$

When integrating Equation 3.37 over all frequencies, the first term has a delta function, converting all frequencies to  $\omega_A$ , but the second term is a complicated integral. However, note that the Kramers-Kronig relations relate the Cauchy Principle integral of the imaginary component of a causal function to its real component, with the causal function being Green's tensor here. For Green's tensor, this follows the

equation [92],

$$\mathcal{P} \int_0^\infty d\omega_P \frac{\omega_P^2 \text{Im}G(r, r_A, \omega_P)}{\omega_P - \omega_A} = \pi\omega_A^2 \text{Re}G(r, r_A, \omega_A) + \int_0^\infty d\kappa \kappa^2 \text{Re}G(r, r_A, i\kappa) \frac{\omega_A}{\kappa^2 + \omega_A^2}, \quad (3.40)$$

where the second term can be considered negligible for this case, since the integral is over the imaginary axis where the Green's tensor exponentially decays, so it is negligible beyond the near-field and does not contribute to the detected fields. Using this relation the scattered field becomes,

$$\begin{aligned} \hat{E}_S^+(r, t) &= i\mu_0\omega_A^2 \text{Im}G(r, r_A, \omega_A) \cdot d(r_A) \hat{\sigma}_{ge}(t) + \mu_0\pi\omega_A^2 \text{Re}G(r, r_A, \omega_A) \cdot d(r_A) \hat{\sigma}_{ge}(t) \\ \hat{E}_S^+(r, t) &= \mu_0\omega_A^2 G(r, r_A, \omega_A) \cdot d(r_A) \hat{\sigma}_{ge}(t). \end{aligned} \quad (3.41)$$

Now to determine transmission, we express the scattered field in terms of  $\hat{E}_P^+(r, t)$  by multiplying and dividing Equation 3.41 by  $d^*(r) \cdot \hat{E}_P^+(r_A, t)$  where we note that these commute, allowing us to write,

$$\begin{aligned} \hat{E}_S^+(r, t) &= \mu_0\omega_A^2 \frac{\hat{E}_P^+(r_A, t) d^*(r) \cdot G(r, r_A, \omega_A) \cdot d(r_A)}{d^*(r) \cdot \hat{E}_P^+(r_A, t)} \hat{\sigma}_{ge}(t) \\ \hat{E}_S^+(r, t) &= \frac{1}{\hat{\Omega}_P} g(r, r_A, \omega_A) \hat{\sigma}_{ge}(t) \hat{E}_P^+(r_A, t), \end{aligned} \quad (3.42)$$

where we have defined the Rabi frequency operator as  $\hat{\Omega}_P = d^* \cdot \hat{E}_P^+ / \hbar$ , where we know that for the rabi frequency,  $\langle \hat{\Omega}_P \rangle = \Omega_P$ , which is an observable representing the frequency of fluctuation of the energy levels in the TLS, making it a measurement for the power of the light field. We have also simplified this equation using the



dipole-projected Green's function [90],

$$g(r_i, r_j, \omega) = \frac{\mu_0 \omega^2}{\hbar} d^*(r_i) \cdot G(r_i, r_j, \omega) \cdot d(r_j). \quad (3.43)$$

Equipped with Equation 3.42, we can define the dipole-projected Green's function based on nanophotonic structure and quantum emitter properties, allowing us to determine the phase shift and transmission of the interaction.

### 3.3 Symmetric Coupling and Scattering Power Dependence

When a quantum dot with an in-plane linear transition dipole (ie. neutral exciton) is coupled to a waveguide where the in-plane local field polarization is linear, the result is a symmetrically coupled quantum emitter [93]. This coupling scheme is the most common because it naturally arises from coupling QDs to standard rectangular waveguides [94, 76, 95]. The dipole-projected Green's function for this system can be defined as [90],

$$g(r, r_A, \omega) = i \frac{\Gamma \beta}{2} e^{ik_P |r - r_A|}, \quad (3.44)$$

where  $\Gamma$  is the rate of spontaneous emission in the TLS, also corresponding to the QD resonant linewidth, and  $\beta$  is the coupling for the waveguide, measured as the ratio of photons emitted into the waveguide versus all photons. This can be written as,

$$\beta = \frac{\Gamma_{WG}}{\Gamma} = \frac{\Gamma_{WG}}{\Gamma_{WG} + \Gamma_{loss}}, \quad (3.45)$$

where  $\Gamma_{WG}, \Gamma_{loss}$  are the rates of emission into the waveguide, and escaping the waveguide, respectively. Note that this is known as the symmetric case since the coupling to the waveguide is independent of the light field's propagation direction. This allows us to write the scattered field from Equation 3.42 as,

$$\hat{E}_S^+(r, t) = i \frac{\Gamma\beta}{2\Omega_P} \hat{\sigma}_{ge}(t) \hat{E}_P^+(r, t), \quad (3.46)$$

where we have used the fact that  $\hat{E}_P^+(r, t) = \hat{E}_P^+(r_A, t) e^{ik_P|r-r_A|}$ .

A quantum dot will have very different light-matter interactions depending on the power of the coupled light field, which we represent with the Rabi frequency. Since the goal of this work is to use the phase shift of the scattered light, we want to work in the region where scattering dominates. To analyze this, we determined the observable transmission,  $T$ , for symmetrically coupled QDs,

$$\begin{aligned} T &= \frac{\langle \hat{E}^- \hat{E}^+ \rangle}{\langle \hat{E}_P^- \hat{E}_P^+ \rangle} \\ &= \frac{\langle (\hat{E}_P^- - i \frac{\Gamma\beta}{2\Omega_P} \hat{\sigma}_{eg}(t) \hat{E}_P^-) (\hat{E}_P^+ + i \frac{\Gamma\beta}{2\Omega_P} \hat{\sigma}_{ge}(t) \hat{E}_P^+) \rangle}{\langle \hat{E}_P^- \hat{E}_P^+ \rangle} \\ &= 1 + i \frac{\Gamma\beta}{2\Omega_P} (\langle \hat{\sigma}_{ge}(t) \rangle - \langle \hat{\sigma}_{eg}(t) \rangle) + \left( \frac{\Gamma\beta}{2\Omega_P} \right)^2 \langle \hat{\sigma}_{eg}(t) \hat{\sigma}_{ge}(t) \rangle, \end{aligned} \quad (3.47)$$

where  $\langle \hat{\sigma}_{ge}(t) \rangle - \langle \hat{\sigma}_{eg}(t) \rangle = 2i \text{Im} \langle \hat{\sigma}_{ge}(t) \rangle$  and  $\langle \hat{\sigma}_{eg}(t) \hat{\sigma}_{ge}(t) \rangle = \langle \hat{\sigma}_{ee}(t) \rangle$ . We can determine these expectation values by applying the operators to the system's density matrix and taking the trace. The derivation of the density matrix and population

dynamics is shown in Section A.3. For  $\langle \hat{\sigma}_{ge}(t) \rangle$ ,

$$\begin{aligned}
 \langle \hat{\sigma}_{ge}(t) \rangle &= Tr \left[ \sum_{ij} \rho_{ij} |i\rangle \langle j| \hat{\sigma}_{ge} \right] \\
 &= Tr [\rho_{gg} |g\rangle \langle e| + \rho_{eg} |e\rangle \langle e|] \\
 &= \rho_{eg} \\
 &= \frac{\Omega_P(i\Gamma_2 - \Delta_P)}{\Gamma_2^2 + \Delta_P^2 + 4(\Gamma_2/\Gamma)\Omega_P^2}.
 \end{aligned} \tag{3.48}$$

Here we use Equation A.28 for  $\rho_{eg}$ , where  $\Delta_P = \omega_P - \omega_A$  is the detuning between the light field and the quantum dot resonant frequency, and we define the mathematically useful  $\Gamma_2 = \frac{\Gamma}{2} + \Gamma_{dp}$ , where  $\Gamma_{dp}$  is the rate of dephasing in the system. More on dephasing in Section 3.5. Note that this is the steady state solution for  $\rho_{eg}$ , which we assume is sufficient since in this work we only consider pulse widths that are orders of magnitude narrower than the QD linewidth, meaning these pulses are spread out in time compared to the QD dynamics, allowing us to assume a steady state. This pulse width constraint is enforced since it is required for a linear phase response from the light field's interaction with the QD, resulting in a phase shift with no amplitude changes in the pulses [96]. Similarly,  $\langle \hat{\sigma}_{ee}(t) \rangle = \rho_{ee}$ , where Equation A.26 shows its population.

The transmission, Equation 3.47, has 3 terms, the first indicating light that passes through and does not interact. If the quantum dot was not there, this would make  $T = 1$ , as expected. The second term, dependent on  $2iIm\rho_{eg}$ , depicts the photons that scatter off the emitter without being absorbed. This is the phase shift interaction we want to enhance. The final term is dependent on  $\rho_{ee}$ , which are the photons that are emitted from the TLS decaying. These photons are not desired for the phase shifters

as they emit at random times, causing their phase shifts to be scrambled. Figure 3.3 depicts the dependence of  $Im\rho_{eg}$  and  $\rho_{ee}$  on Rabi frequency, indicating that at high power, TLS decay will dominate, and at low power, scattering will dominate. Thus, to ensure we are getting phase shifts from scattering we need  $\Omega_P \rightarrow 0$ , which matches with the goal of building MZM circuits as we use single photons for information, as described in Chapter 2, and have near-zero power.

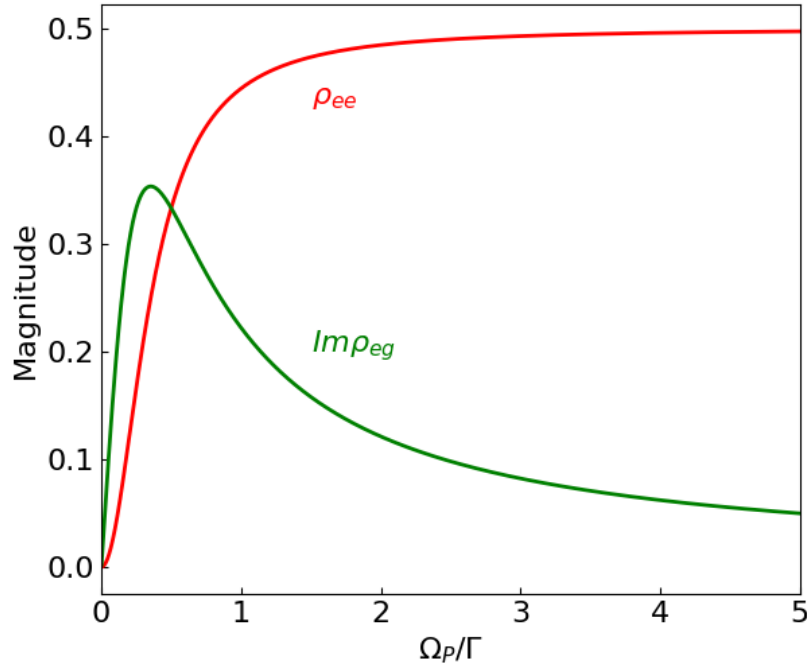


Figure 3.3: Light-matter interaction dependence on Rabi frequency.  $Im\rho_{eg}$  (green) represents a scattering event, and  $\rho_{ee}$  (red) represents emission from TLS decay. For this data,  $\Delta_P = 0$ ,  $\Gamma_{dp} = 0$ ,  $\beta = 1$ .

Note that this derivation assumes the use of coherent pulses, but in practice, we consider single photons for this architecture. However, here we consider the low-power regime, where we have coherent pulses with average photon number  $\ll 1$ . This allows us to assume that we primarily have a combination of terms with zero photons

with no interaction and terms with the single photon interaction as desired. While some terms from two-photon interaction could be present, we assume the number of occurrences to be much less than the single-photon case, making them negligible.

Next, we want to know the phase shift from symmetric coupling, which we can find through the transmission coefficient with Equation 3.29 as,

$$\begin{aligned}
 t &= \frac{\langle \hat{E}^+ \rangle}{\langle \hat{E}_P^+ \rangle} \\
 &= 1 + i \frac{\Gamma \beta}{2\hat{\Omega}_P} \langle \hat{\sigma}_{ge}(t) \rangle \\
 &= 1 + i \frac{\Gamma \beta}{2\Omega_P} \frac{\Omega_P(i\Gamma_2 - \Delta_P)}{\Gamma_2^2 + \Delta_P^2 + 4(\Gamma_2/\Gamma)\Omega_P^2}
 \end{aligned} \tag{3.49}$$

which is 0 if  $\beta = 1$ ,  $\Gamma_{dp} = 0$ ,  $\Omega_P \rightarrow 0$ ,  $\Delta_P = 0$ , resulting in no transmission. The reflection coefficient however, following Equation 3.30, gives  $r = -1$ , meaning all light would be reflected with a phase shift of  $\pi$ . This result indicates that the symmetric case will not work for our application, as in the perfect case all light will be reflected, but in a QPIC light must feed forward. Thus, despite the popularity of symmetric coupling to harness quantum dot phase shifters, we require a different coupling scheme.

### 3.4 Chiral Quantum Dot Coupling

This leads us to instead consider the chiral coupling scheme, which occurs when the QD has a circular transition dipole and is coupled in a location that has a local circular light field polarization. Since the interaction is the dot product between the polarization and the dipole, as shown in Equation 3.5, and the reciprocal light field will have the complex conjugate of the polarization, this causes light from one direction

to interact with the QD and emit forwards, and light from the other direction to pass through with no interaction, achieving the desired non-reciprocal emission for QPIC implementation [97]. This coupling scheme is shown in Figure 3.4, where most of the light is scattered forward in the waveguide picking up a phase shift  $\phi$ . We also include imperfections in this figure, with non-zero reflection  $R$  and coupling loss  $C$  from light scattered out of the waveguide. Here we also introduce a new parameter  $\gamma = 1 - T$  to represent the loss from the interaction.

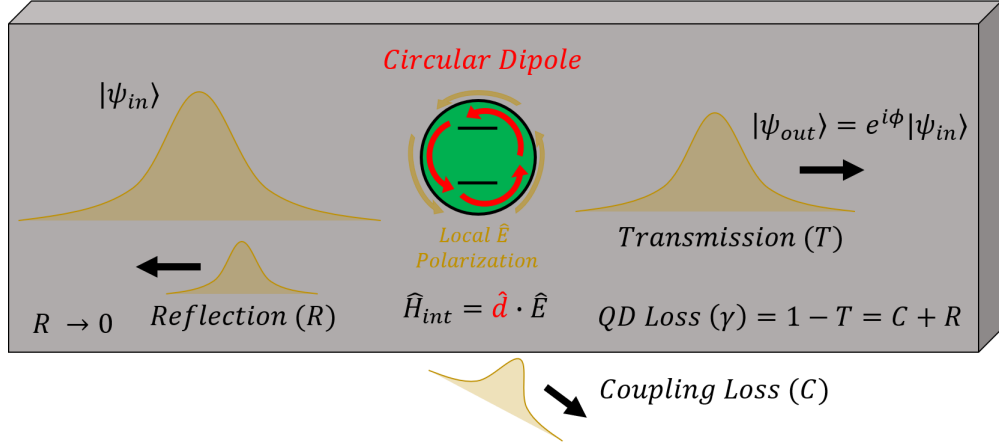


Figure 3.4: Chiral quantum dot coupled to a waveguide. Here the forward direction is chosen as right, and we are working in the low power regime, meaning the transmitted light will be from scattering and pick up a phase shift  $\phi$ . The QD has a circular transition dipole and is located at a point in the waveguide with circular electric field polarization.

To derive the phase shift and transmission of a chiral QD, we first establish the appropriate dipole-projected Green's function (Equation 3.43) for the system. With a circular dipole and a circular field polarization this can be modeled as,

$$g(r, r_A, \omega) = i\Gamma(\Theta(r_A - r)\beta_L + \Theta(r - r_A)\beta_R)e^{ik_p|r-r_A|}, \quad (3.50)$$

where we define the couplings for photons moving left  $\beta_L$  and for photons moving right  $\beta_R$  as,

$$\beta_L = \frac{\Gamma_L}{\Gamma} = \frac{\Gamma_L}{\Gamma_L + \Gamma_R + \Gamma_{Loss}}, \quad (3.51)$$

$$\beta_R = \frac{\Gamma_R}{\Gamma} = \frac{\Gamma_R}{\Gamma_L + \Gamma_R + \Gamma_{Loss}}. \quad (3.52)$$

These now include  $\Gamma_L$  and  $\Gamma_R$ , which are the rates of spontaneous emission for light moving left and right in the waveguide, respectively. Equation 3.50 also uses the Heaviside function,

$$\Theta(x) = \begin{cases} 0 & \text{if } x < 0 \\ 1 & \text{if } x > 0 \end{cases}, \quad (3.53)$$

which allows Equation 3.50 to select  $\beta_L$  or  $\beta_R$  depending on the side of the waveguide we are on. While this is not based on the direction light is moving, but rather the location in the waveguide, they are equivalent since this is for the scattered field, which will always be moving away from the emitter.

Note that although the derivation from the Hamiltonian (Equation 3.5) did not list different bosonic,  $\hat{f}$ , or electric field,  $\hat{E}$ , operators for left and right traveling light, they both depend on Green's tensor, which encodes the directional information from Equation 3.50, meaning this model still holds for the chiral case. The same goes for the Rabi frequency, which is also directionally dependent, but is dependent on the electric field operator and thus contains that information as well.

Equipped with Equation 3.50, the scattered field becomes,

$$\hat{E}_S^+(r, t) = i \frac{\Gamma}{\hat{\Omega}_P} (\Theta(r_A - r) \beta_L + \Theta(r - r_A) \beta_R) \hat{\sigma}_{ge}(t) \hat{E}_P^+(r, t). \quad (3.54)$$

Now we can determine the phase shift using Equation 3.29 to determine the transmission coefficient,

$$\begin{aligned}
t &= 1 + \frac{\langle \frac{i\Gamma}{\Omega_P} (\Theta(r_A - r)\beta_L + \Theta(r - r_A)\beta_R) \hat{\sigma}_{ge}(t) \hat{E}_P^+(r, t) \rangle}{\langle \hat{E}_P^+(r, t) \rangle} \\
t &= 1 + \frac{i\Gamma}{\Omega_P} (\Theta(r_A - r)\beta_L + \Theta(r - r_A)\beta_R) \langle \hat{\sigma}_{ge}(t) \rangle \\
t &= 1 - (\Theta(r_A - r)\beta_L + \Theta(r - r_A)\beta_R) \frac{\Gamma(\Gamma_2 + i\Delta_P)}{\Gamma_2^2 + \Delta_P^2 + 4(\Gamma_2/\Gamma)\Omega_P^2}.
\end{aligned} \tag{3.55}$$

To determine the potential phase shifts of this scheme, take the forward direction as right and assume we are looking at the transmission in that direction, collapsing Equation 3.55 into,

$$t = 1 - \beta_R \frac{\Gamma(\Gamma_2 + i\Delta_P)}{\Gamma_2^2 + \Delta_P^2 + 4(\Gamma_2/\Gamma)\Omega_{P_R}^2}, \tag{3.56}$$

where the Rabi frequency is now  $\Omega_{P_R}$  to indicate the Rabi frequency for light going right. Now, we assume the perfectly directional case with no errors where  $\beta_R = 1$ ,  $\Omega_{P_R} \rightarrow 0$ ,  $\Gamma_{dp} = 0$ , and  $\Delta_P = 0$ , giving,

$$t = 1 - \frac{\Gamma^2/2}{\Gamma^2/4} = -1, \tag{3.57}$$

resulting in a phase shift of  $\pi$  from Equation 3.31. However, if  $\Delta_P \rightarrow 0$  from the right,  $t$  will have a very small negative imaginary component, resulting in a phase shift of  $-\pi$ . Thus, chiral quantum dots can span a phase shift range of  $[-\pi, \pi]$ , meeting the phase requirements for MZM phase shifters as listed in Section 2.1. Note that if you calculate the reflection with Equation 3.30, the Heaviside function would use  $\beta_L$  instead of  $\beta_R$ , where in this case  $\beta_L = 0$ , resulting in  $r = 0$ . Thus, in the perfect case,



all scattered light will transmit forward in the waveguide and pick up a phase shift, as desired for QPIC implementation.

Note that although you may be tempted to calculate  $|t|^2$  for the observable transmission, it only describes the transmission from the incident field and the scattered light, whereas  $T$  describes all observable transmission. While they are often equivalent, this is not the case with dephasing, as described in Section 3.5. Thus, to know losses, we need to determine  $T$ , which can be derived similarly to Equation 3.47 as,

$$T = 1 + 2(\Theta(r_A - r)\beta_L + \Theta(r - r_A)\beta_R)\Gamma_2 \left( \frac{\Theta(r_A - r)\beta_L + \Theta(r - r_A)\beta_R - 1}{\Gamma_2^2 + \Delta_p^2} \right), \quad (3.58)$$

where we have assumed we are in the low-power regime ( $\Omega_P \rightarrow 0$ ).

The chiral coupling scheme allows us to use quantum dots as phase shifters in QPICs, but the question remains on how we can achieve a circular transition dipole overlapping with a local circular in-plane field polarization. A circular transition dipole can be achieved for QDs either by coupling to a charged exciton, which naturally exhibits a circular dipole, or by applying a constant external magnetic field to the QD, which causes the in-plane neutral excitons to couple together and create a circular transition dipole from Zeeman splitting [98].

While finding a high-quality QD in a location with the correct local circular light-field polarization can be difficult, it can be done on many different platforms [45]. The current most successful platform for implementing chirally coupled quantum dots is photonic crystal waveguides, where light can be slowed down for strong interaction, and local circular polarizations are simpler to engineer [99]. Specifically, the use of glide-plane waveguides is common, where holes on one side of the in-plane axis of

symmetry are shifted, making circular polarization more abundant [97, 100]. However, chiral emitter implementations using other photonic crystal structures such as bearded-type and zig-zag interfaces [99] have also been considered, as well as using whispering-gallery-mode nanophotonic resonators [101], nanowire waveguide crossings [102], optical fibers with arrays of cold atoms [103], and standard nanophotonic waveguides [99, 104].

### 3.5 Chiral Quantum Dot Imperfections

While there are many advantages to using quantum dots as phase shifters in QPICs, as outlined in Chapter 1, chiral quantum dots have additional imperfections that must be considered when evaluating them.

#### 3.5.1 Quantum Dot Losses

Loss from chiral quantum dots comes from two different imperfections, coupling and directionality. Here we begin with coupling, which is the measure of how well a quantum dot is coupled to the waveguide. This is defined in the chiral case as,

$$\begin{aligned}\beta &= \beta_L + \beta_R \\ \beta &= \frac{\Gamma_L + \Gamma_R}{\Gamma},\end{aligned}\tag{3.59}$$

where  $\beta$  is the coupling coefficient between the QD and the waveguide. Perfect coupling is when  $\beta = 1$ , meaning no light is lost from the waveguide. We also note here that,

$$\Gamma = \Gamma_L + \Gamma_R + \Gamma_{Loss}.\tag{3.60}$$

For chiral quantum dots, a state-of-the-art implementation in photonic crystal waveguides achieved  $\beta = 0.984$  [44], which massively outclasses other platforms for the time being. A typical coupling for other current implementations is  $\beta \approx 0.90$  [97, 103, 105].

Directionality, on the other hand, is a measure of how well the QD scatters light in the forward direction versus how much is reflected. It is defined as,

$$\begin{aligned} D &= \frac{\beta_R - \beta_L}{\beta_L + \beta_R} \\ D &= \frac{\Gamma_R - \Gamma_L}{\Gamma_L + \Gamma_R} \end{aligned} \tag{3.61}$$

assuming right is the forward direction, which will be the assumption throughout this work. Perfect directionality would be  $D = 1$ , where  $\beta_L = 0$ , indicating that all the light is interacting with the QD, staying in the waveguide, and going in the forward direction. State-of-the-art implementations in glide-plane waveguides have shown a directionality of  $D \geq 0.90$  [97]. However, a state-of-the-art nanobeam waveguide implementation was able to achieve a directionality of  $D = 0.95 \pm 0.05$  [104], which is the best implementation to date.

In this work, directionality and coupling factor solely into the loss of a quantum emitter, since although directionality will cause some light to be reflected and reach previous phase shifters in the circuit, the high directionality of these phase shifters will cause limited interaction with those emitters, so we exclude this from the simulations and consider that light lost. This assumption could lead to small inaccuracies at lower directionalities near  $D = 0.50$ , which we do simulate in Chapter 4, but since performance is already poor at those lower directionalities, the difference is inconsequential.

Thus, we model the QD loss by adding a loss factor  $\gamma$  to the phase shifters, where

$$\gamma = 1 - T, \quad (3.62)$$

where  $T$  is the transmission from Equation 3.58. Directionality and coupling naturally factor into the loss since they depend on the  $\beta$ 's. The adjusted phase shifter matrices in the MZI from Equation 2.11 become,

$$PS = \begin{bmatrix} e^{i\phi}\sqrt{1-\gamma} & 0 \\ 0 & 1 \end{bmatrix}, \quad (3.63)$$

where  $PS$  is our phase shifter matrix, and  $\phi$  is the phase shift applied on the top path. This, combined with nanophotonic loss and beam splitter error as mentioned in Section 2.2, results in our imperfect MZI matrix of,

$$MZI = \begin{bmatrix} \sqrt{r_2} & i\sqrt{1-r_2} \\ i\sqrt{1-r_2} & \sqrt{r_2} \end{bmatrix} \begin{bmatrix} \sqrt{1-\gamma_2}e^{i2\theta} & 0 \\ 0 & 1 \end{bmatrix} \begin{bmatrix} \sqrt{r_1} & i\sqrt{1-r_1} \\ i\sqrt{1-r_1} & \sqrt{r_1} \end{bmatrix} \begin{bmatrix} \sqrt{1-\gamma_1}e^{i\phi} & 0 \\ 0 & 1 \end{bmatrix} \begin{bmatrix} \sqrt{1-L} & 0 \\ 0 & \sqrt{1-L} \end{bmatrix}, \quad (3.64)$$

where we have the losses  $\gamma_1, \gamma_2$  from the two QD phase shifters, beam splitter reflectivities of  $r_1, r_2$  associated with the two imperfect beam splitters, and  $L$  representing the nanophotonic loss per MZI.

### 3.5.2 Environmental Interactions with Emitters

While the ideal chiral QD embedded in a nanophotonic system would have no interaction with the environment, in hardware, while they can be limited, they are impossible to remove entirely. Thus, we must consider these interactions in our model. These interactions can be grouped into two phenomena; spectral diffusion, and dephasing.

Spectral diffusion is the broad term that encompasses all environmental interactions with the emitter that cause its resonant frequency to shift over time. It encompasses the effects of both slow noise, like temperature fluctuations, and fast noise, like charge/spin noise [106], and because of this will often be listed in the literature on both short and long time scales, such as one minute versus hours [105]. The effect this has over many samples is a broadening of the linewidth of the QD, which can be modeled as a convolution between the QD emission spectra and the spectral diffusion distribution. The spectral diffusion distribution is modeled as a normal distribution about the quantum dot resonant frequency with some standard deviation  $\sigma_{SD}$ ,

$$\sigma_{SD} = \frac{\Gamma_{SD}}{\Gamma}, \quad (3.65)$$

where  $\Gamma_{SD}$  is the linewidth of the normal distribution for spectral diffusion, which we measure relative to  $\Gamma$ . This then allows you to model spectral diffusion as a normal Gaussian distribution with the formula,

$$SD(\Delta) = e^{\frac{-\Delta^2}{2\sigma_{SD}^2}}, \quad (3.66)$$

where  $\Delta$  is the detuning from the quantum dot resonant frequency. While this convolutional linewidth broadening model is sufficient for applications like single photon

generation and characterization of on-chip QDs [107, 108, 42], Section 3.6 shows that the phase shift from a QD is heavily dependent on the detuning between the light field and the QD resonant frequency. Since we are sampling on the single photon level, the spectral diffusion shift at any point in time will have a large effect on the phase shifts and consequently performance of our circuit. Thus, to model this in this work, we instead sample from a normal distribution with standard deviation  $\sigma_{SD}$  for every phase shifter.

While most literature characterizes spectral diffusion in terms of a linewidth broadening, some implementations list  $\sigma_{SD}$  [105, 109, 110]. Of these, one implementation lists fast spectral diffusion around 27% [105]. However, a pure dephasing rate of 6%, which includes both dephasing and spectral diffusion, has also been achieved, so conservatively assuming that is all coming from spectral diffusion, this can be used as a typical  $\sigma_{SD}$  [111]. However, integrating QDs into p-i-n diodes has been shown to provide QD resonant frequency tunability through a Stark shift by applying a voltage across the QD, which can in principle eliminate all spectral diffusion from the system [42]. It has also been shown that if QDs can be operated at high enough frequencies, spectral diffusion can also be eliminated [106]. This allows us to consider the state-of-the-art spectral diffusion as  $\sigma_{SD} = 0$ .

Conversely, dephasing is caused by fast environmental interactions that cause fluctuations of the excited state energy level of an emitter. Fast, in this context, encompasses noise that is on a faster time scale than the decay dynamics of the emitter. While the natural linewidth of the QD corresponds to the rate of excited-to-ground state transitions, which can be written as  $\Gamma = \Gamma_{eg} = \Gamma_{ge}$ , the pure dephasing rate can instead be written in terms of the rate of transitions between the same

states  $\Gamma_{dp} = \Gamma_{ee} = \Gamma_{gg}$ , where  $\Gamma_{dp}$  is usually quantified relative to  $\Gamma$  as a percentage. Dephasing adds incoherence to a QD phase shifter, since its fast fluctuations will cause a pulse's phase to be scrambled, imparting an average of 0 phase shift onto the QD instead of the desired phase shift. However, as we show in Section 3.6, this effect is probabilistic where the chance of a phase shifter imparting 0 phase shift depends on the rate of dephasing, forcing us to implement this with a probabilistic model, as outlined in Chapter 4. The incoherence probability from dephasing can be quantified from the difference between the overall transmission,  $T$  (Equation 3.58), and the coherently scattered transmission,  $|t|^2$  (Equation 3.55).

Current hardware implementations are now able to achieve dephasings as low as 0–2% [105, 97, 112, 113, 114], allowing us to assume no dephasing for state-of-the-art implementations.

### 3.6 Reconfigurability through Detuning

To implement and optimize a QPIC the phase shifters must be reconfigurable, but most QD parameters are set from fabrication and are difficult to adjust. However, the detuning,  $\Delta_P$ , between the light field and QD resonant frequency can be adjusted on nanosecond time scales and thus becomes the go-to control parameter for setting and adjusting phases due to its large effect on the transmission and phase shift, as shown in Equations 3.58 and 3.55. Detuning is not reconfigurable through adjusting light field frequency, since each phase shifter must be able to be independently controlled. It can instead be adjusted by embedding QDs into p-i-n diodes, allowing voltage application across them, causing a shift of the QD resonant frequency due to the Stark Effect. This can be controlled on the time scale of hundreds of  $ns$  [42], making

it an order of magnitude faster than thermo-optic phase shift reconfigurability [31]. It has also been shown that by shining pump photons onto the QDs, the same effect can be achieved, allowing an all-optical implementation with sub-nanosecond detuning control [43].

Figure 3.5 shows the effects of detuning on transmission and phase shift. Figure 3.5a depicts the ideal transmission with no QD imperfections, as well as  $T$  and  $|t|^2$  (Equations 3.58, and 3.55) for the case where  $\Gamma_{dp} = 0.10\Gamma$ ,  $D = 1$ , and  $\beta = 0.9$ . The first thing we see from this figure is that with more detuning you get less interaction from the QD, meaning the effects of loss and dephasing are minimized. However, you can see as detuning approaches zero, QD loss and the effects of incoherence from dephasing become more relevant. This is included in our simulations through the transmission and phase shift equations, where phase shifters with higher detunings are less susceptible to imperfections.



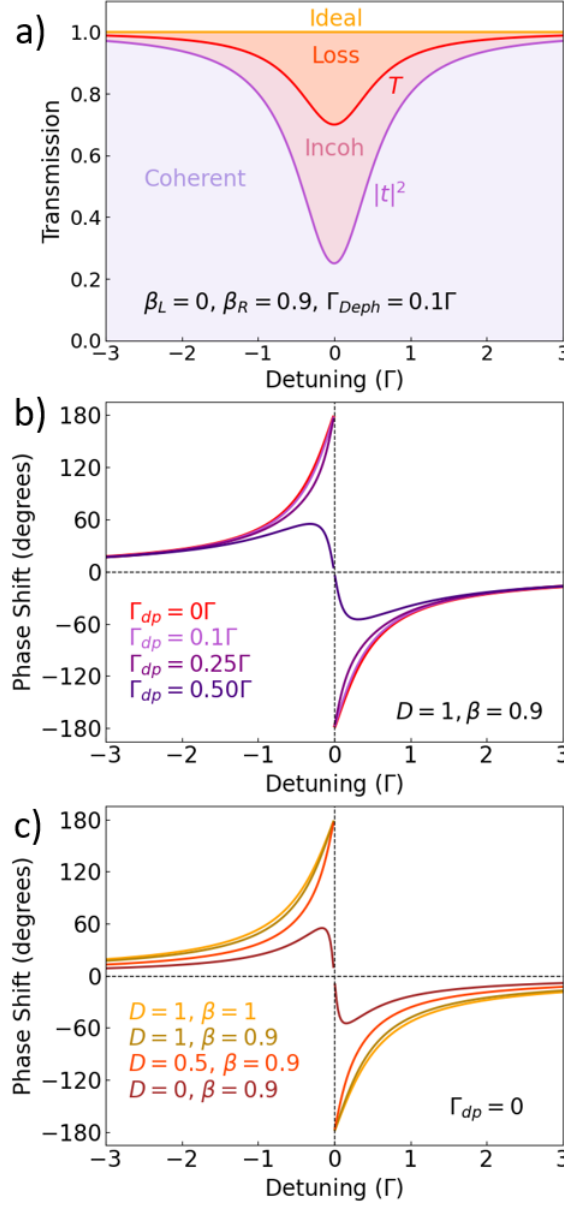


Figure 3.5: Transmission and phase shift detuning dependence across a range from  $\Delta_P = -3\Gamma$  to  $\Delta_P = 3\Gamma$ . (a) QD transmission detuning dependence for the ideal chiral QD, and a QD with  $\Gamma_{dp} = 0.10\Gamma$ ,  $\beta = \beta_R = 0.9$ .  $|t|^2$  (mauve) depicts the coherent scattered transmission that picks up the desired phase shift.  $T$  (red) depicts the overall forward transmission, which includes the coherent photons as well as the incoherent photons from dephasing. (b) Phase shifts for dephasings ranging from  $\Gamma_{dp} = 0\Gamma$  to  $\Gamma_{dp} = 0.5\Gamma$ , with  $\beta = 0.9, D = 1$ . (c) Phase shifts for directionalities ranging from  $D = 1$  to  $D = 0$ , with  $\Gamma_{dp} = 0, \beta = 0.9$ . Also depicts the ideal case with  $D = 1, \beta = 1$ .

Figure 3.5b,c show the QD phase shifts (Equation 3.31) based on detuning for different levels of dephasing (Figure 3.5b) and different directionalities (Figure 3.5c). We see that the lack of interaction from larger detuning also causes a lower phase shift on scattered light, and by spanning across negative and positive detunings, this provides a reconfigurable phase shift range of  $[-\pi, \pi]$ , as we claimed in Section 3.4. Imperfections such as dephasing, directionality, and coupling will have an effect on the required detuning for a specific phase, changing the shape of the phase shift curves. However, this will not limit the phase shift range unless the coherent coupling  $\beta_R$  in the forward direction becomes less than 0.5, in which case  $t$  can no longer have negative real components, causing a limit in the phase shift. Thus, the achievable phase shift range is robust, as very high imperfections would be required to limit the range.

## Chapter 4

### Circuit Simulations and Results

In this chapter, we display results for simulations performed on random circuits of varying sizes with different levels of error and loss. We begin with only nanophotonic imperfections, then add quantum dot imperfections to accurately determine the overall performance and scalability of this architecture on arbitrary circuits. To simulate arbitrary quantum circuits, we use Haar random unitaries, which is standard for sampling random circuits [115, 116, 117, 59]. To generate these random unitaries we use Qiskit’s Python library, which has a generate random unitaries function [118]. We then consider example circuits with the unheralded CNOT and CZ, determining output infidelities for specific imperfections. These simulations allow us to draw conclusions about the validity and scalability of our architecture.

#### 4.1 Simulations with Nanophotonic Imperfections

First, to understand the role of nanophotonic imperfections on circuit performance, we consider circuits with only nanophotonic loss and beam splitter error. For nanophotonic loss, we use Equation 2.24 to apply a balanced loss to each MZI. A central value for nanophotonic loss is given when simulating the circuit, but each MZI will

sample a different nanophotonic loss from a normal distribution around this central value, as shown in Figure 4.1. This figure depicts the normal distribution around a central nanophotonic loss of 4.5% per MZI, showing an example of losses that may be sampled from the distribution for the 6 MZIs in a  $4 \times 4$  MZM. The loss distribution will always have a standard deviation of 5% of the central value, which we chose to mimic randomness in fabrication parameters.

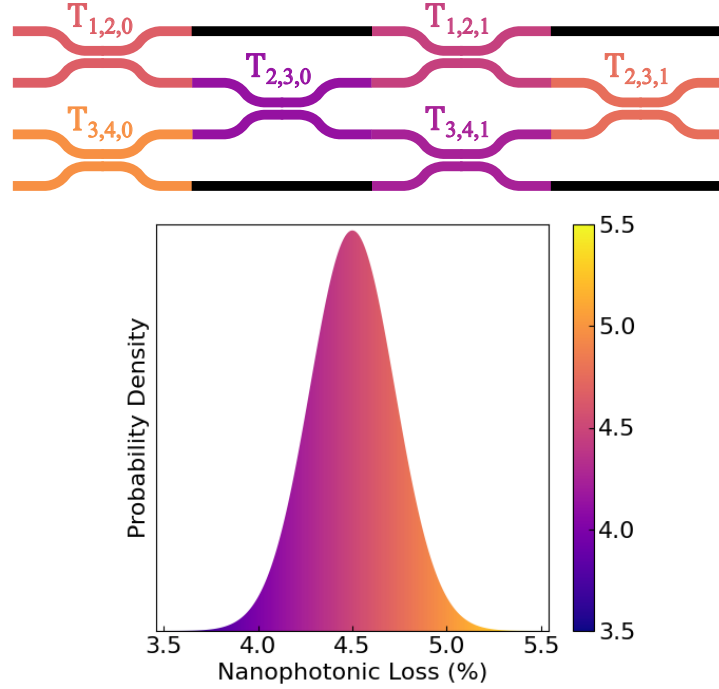


Figure 4.1: Example distribution for nanophotonic loss with a central value of 4.5%. Standard deviation for the normal distribution is chosen as 5% of the central value. Each MZI has loss based on a random sample from this distribution, as shown in the example  $4 \times 4$  mesh.

Thus, to determine the effects of nanophotonic losses we performed a simulation that spanned across central loss values of 0.1% to 50%, for  $N = 2, 6, 10$  circuits<sup>1</sup>,

<sup>1</sup>Note that we chose  $N = 2, 6, 10$  for most simulations to see the effects of different circuit sizes, but simulations can be run on any  $N$ .

as shown in Figure 4.2. Each point on these lines is the result of 100 Haar random unitary trials, which are averaged by taking the mean of a beta distribution fit to their matrix infidelities. A beta fit is used for all our random circuit simulations as it matches the infidelity distribution between trials more accurately than a normal fit or the mean of the data, which we outline in Section B.1. This plot includes both imperfect and globally<sup>2</sup> optimized simulation results, as described in Section 2.3 of Chapter 2.

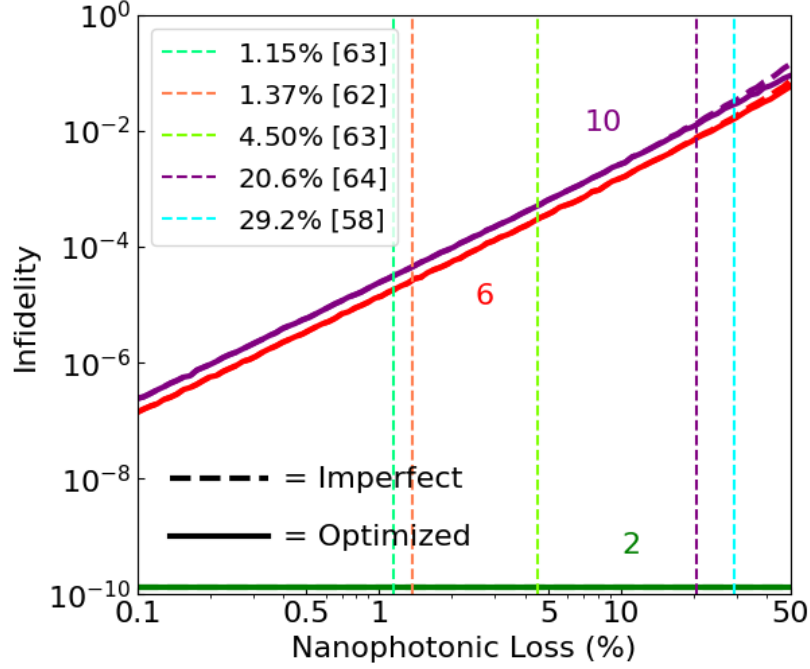


Figure 4.2: Circuit infidelities spanning across nanophotonic losses of 0.1% to 50% for  $N = 2$  (green),  $N = 6$  (red),  $N = 10$  (purple) modes, including imperfect (dashed) and optimized (solid) results. Vertical lines depict losses per MZI for existing implementations [63, 62, 64, 58], benchmarking circuit performance.

<sup>2</sup>All optimized results in this chapter are from the global optimization method, and will hereto only be referred to as the “optimized” results.

We see from Figure 4.2 that  $N = 2$  circuits perform perfectly with this loss since one MZI will have balanced loss, which our infidelity excludes (Equation 2.25). The non-zero infidelity comes only from computational rounding error. The larger circuits ( $N = 6, 10$ ) increase in infidelity with higher loss, where the difference in performance between 6 and 10 mode circuits is minimal, indicating good nanophotonic loss scalability. We also know from Chapter 1 that for fault tolerant computing we require infidelities of  $\mathcal{I} \leq 10^{-2}$ , which we achieve for the losses  $< 20\%$  for up to 10 modes. We also see from the figure that optimization with only loss is minimal, which is an expected result as without errors there is little to adjust for. For all further simulations, the central value for nanophotonic loss was chosen as 4.5% [63], as we do not specify hardware specifications in this work, so we chose a conservative value based on existing implementations, as shown in Figure 4.2.

The other nanophotonic imperfection we include is beam splitter error, which is applied by replacing the 50:50 beam splitter matrices (Equation 2.9) in the circuit with Equation 2.23. Similar to nanophotonic loss, to mimic hardware randomness, we sample from a normal distribution for each beam splitter's splitting ratio centered around 50%, as described in Section 2.2.

To then test the effects of beam splitter error, we simulated the matrix infidelities of  $N = 2, 6, 10$  circuits across errors of 0.1% to 50%, where again each point is the result of a beta fit to the infidelities for 100 Haar random unitaries. Figure 4.3 shows the results of these simulations for imperfect and optimized circuits, where we see that with beam splitter errors  $< 10\%$ , we can achieve infidelities required for fault-tolerant computing for up to 10 modes. This figure also shows that beam splitter error has a more significant effect on performance than loss, as infidelities for  $N = 6, 10$

are approximately an order of magnitude larger at most points. However, with the addition of errors, we see the importance and success of the global optimization, which is able to adjust the phase shifters to reduce infidelity by up to an order of magnitude. For all further simulations, we chose beam splitter error to be 4% [59], based on a conservative choice compared to existing implementations as shown in Figure 4.3.

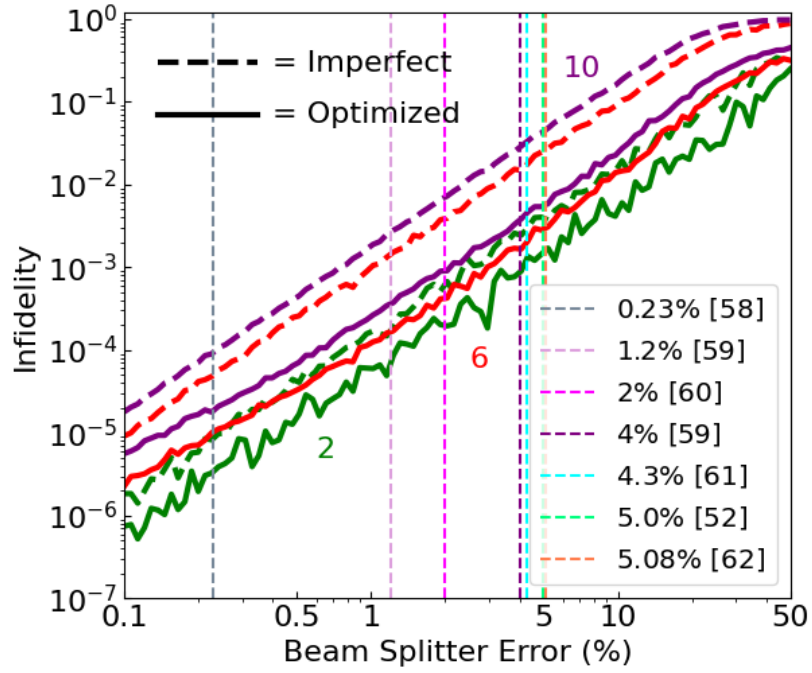


Figure 4.3: Circuit infidelities spanning beam splitter errors of 0.1% to 50% for  $N = 2$  (green),  $N = 6$  (red), and  $N = 10$  (purple) circuits, with both imperfect (dashed) and optimized (solid) data. Vertical lines show errors used by existing implementations [58, 59, 60, 61, 52, 62], benchmarking performance.

Having chosen values for the nanophotonic imperfections that will be used throughout the rest of the simulations, we now benchmark the infidelity for these choices before introducing quantum dot imperfections. Specifically, we benchmark these on  $N = 2, 6, 10$  circuits with 100 Haar random unitaries each, as these are the circuit

sizes we test in further simulations. Using a beta fit, we get imperfect infidelities of  $\mathcal{I} = \{0.0026, 0.016, 0.029\}$  and optimized infidelities of  $\mathcal{I} = \{0.0011, 0.0017, 0.0021\}$  for  $N = 2, 6, 10$ , respectively. All these optimized infidelities are below the limit for fault-tolerant computing, indicating that before adding quantum dot imperfections, this is achievable. These infidelities also show that we get more optimization for larger circuits, which is expected due to the increased number of optimization parameters.

## 4.2 Simulations with Imperfect Directionality and Coupling

With nanophotonic imperfections benchmarked, we are able to explore quantum dot imperfections, starting with coupling and directionality as they simply factor into the loss of a phase shifter through  $\gamma$ , as shown in Equation 3.62, which is calculated from the observable forward transmission (Equation 3.58).

All quantum dot parameters are passed to the simulation code through the  $\Gamma$ 's of the system (as described in Equation 3.60). However, since all parameters are normalized to  $\Gamma$ , we can set  $\Gamma = 1$ , even though this is a non-physical choice, making the  $\beta$ 's equivalent to the  $\Gamma$ 's, as is clear from Equations 3.51, 3.52. Thus, from now on we will express coupling and directionality in terms of the  $\beta$ 's for simplicity. Note that for all simulations we also choose right as the forward direction for our circuits, meaning in the ideal case we want  $\beta_R = 1$  and  $\beta_L = 0$ .

To run a simulation with a specific value of directionality or coupling, we choose a  $\beta_L$  and  $\beta_R$  to send to the simulation such that Equations 3.59 and 3.61 correspond to the desired  $\beta$  and  $D$ , respectively. However, for each QD phase shifter within the mesh, the  $\beta_L$  and  $\beta_R$  values are sampled from a normal distribution with central values as the chosen  $\beta$ 's, and standard deviations of 5% of the central value. This allows us



to simulate random fabrication fluctuations for directionality and coupling between different quantum dots in the mesh. This follows the same method as nanophotonic loss, as depicted in Figure 4.1, except it is for each phase shifter instead of each MZI.

To begin, we want to determine the importance of having well-coupled quantum dots in these circuits and how detrimental coupling can be to performance. Thus, we simulated circuit infidelities for  $N = 2, 6, 10$  circuits across couplings from  $\beta = 0.5$  to  $\beta = 1$ , with perfect directionalities  $D = 1$ , and including the nanophotonic errors as listed in Section 4.1. These results are shown in Figure 4.4, where we show both imperfect and optimized results, and each point on the lines is taken from the beta fit to the infidelities of 100 Haar random unitaries. This figure also depicts the state-of-the-art coupling in orange [44], and the typical coupling in blue [97], as listed in Section 3.5.

We see from Figure 4.4, that at  $\beta = 1$ , we retrieve the nanophotonic case, and as coupling decreases we see large increases in infidelity, where circuits become useless close to  $\beta = 0.5$ . However, for the state-of-the-art  $\beta = 0.98$ , we see  $\mathcal{I} < 10^{-2}$  for circuits up to size  $N = 10$ , as desired for fault-tolerant computing. We also see that optimization can account well for coupling with better optimization for larger circuits, allowing  $N = 10$  circuits to have comparable infidelities to  $N = 6$  and below. The optimization can improve infidelities by up to an order of magnitude near perfect coupling, but cannot retain this level of optimization as coupling decreases, indicating a need for good QD coupling in this architecture.

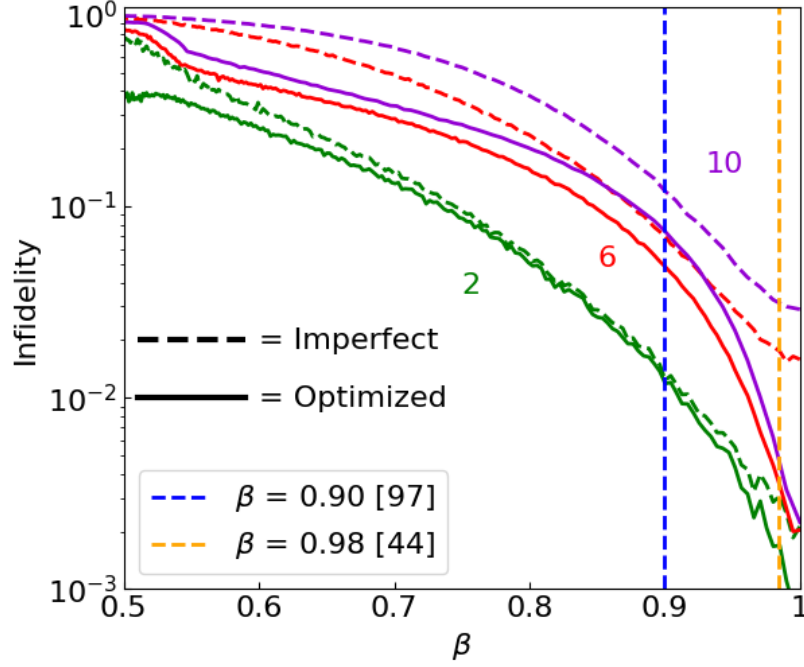


Figure 4.4: Circuit infidelities for couplings ranging from  $\beta = 0.5$  to  $\beta = 1$ , for  $N = 2$  (green),  $N = 6$  (red), and  $N = 10$  (purple) modes, including nanophotonic imperfections as listed in Section 4.1. Each point is taken from the beta fit to 100 Haar random unitaries and both imperfect (dashed) and optimized (solid) data is shown. The orange line depicts state-of-the-art coupling of  $\beta = 0.98$  [44], and the blue depicts the typical value of  $\beta = 0.90$  [97].

We also performed the same simulations for directionality from  $D = 0$  to  $D = 1$ , with perfect coupling,  $\beta = 1$ , for  $N = 2, 6, 10$ , as shown in Figure 4.5. This figure also depicts the typical directionality of  $D = 0.90$  [97] and the state-of-the-art of  $D = 0.95$  [104], as listed in Section 3.5.

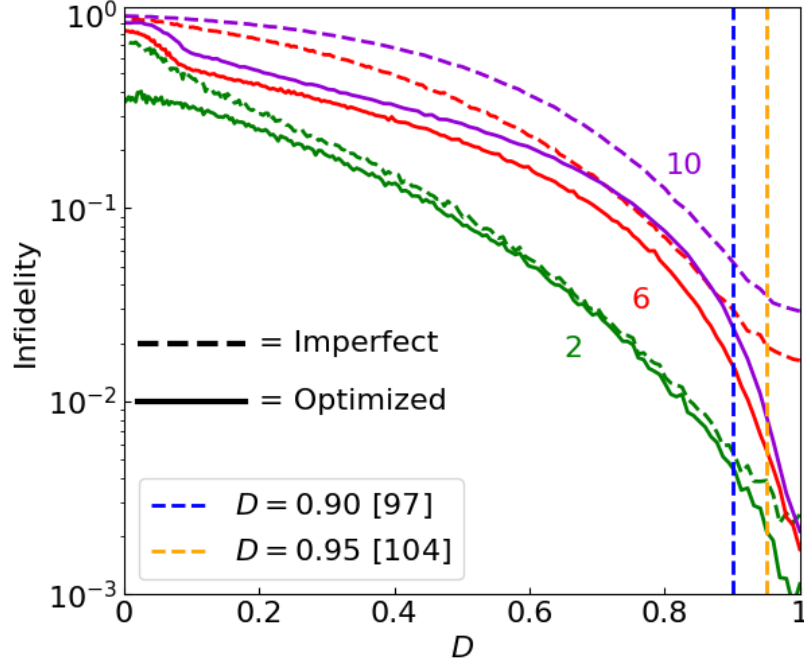


Figure 4.5: Directionality matrix infidelity simulations spanning  $D = 0$  to  $D = 1$  for imperfect (dashed) and optimized (solid)  $N = 2$  (green),  $N = 6$  (red),  $N = 10$  (purple) circuits, including nanophotonic imperfections as listed in Section 4.1. Each point is taken from the beta fit to 100 Haar random unitaries. The orange line depicts state-of-the-art directionality of  $D = 0.95$  [104], and the blue depicts the typical value of  $D = 0.90$  [97].

Figure 4.5 follows the same infidelity curves as coupling, which was expected since they both factor similarly into QD loss. Again here we see better optimization for larger circuits, advocating well for scalability, and the best optimization when near-perfect directionality. We also see that  $D = 0.8$  has equivalent losses to  $\beta = 0.9$ , which is exactly as expected since  $D = 0.8$  with perfect coupling requires  $\beta_R = 0.9$  and  $\beta_L = 0.1$ , which means it would have the equivalent  $\beta_R$  as a coupling of  $\beta = 0.9$ . Thus, while directionality is a different imperfection than coupling, they factor into loss the same way, as all that matters is the light that is coupled forward. At state-of-the-art directionality, we see  $\mathcal{I} < 10^{-2}$ , as desired for fault-tolerance, for optimized

results with circuit sizes as high as  $N = 10$ .

QD loss is more impactful to infidelity than nanophotonic loss because both phase shifters are in the upper path of each MZI, which inherently adds unbalanced losses, but the circuit is able to learn to adjust for the imbalance as long as losses are in the range of typical to state-of-the-art values. While you could consider an architecture with extra phase shifters on the other side of each MZI, this would essentially double the overall loss per MZI and would require more QDs per circuit, which could be a detriment to scalability.

### 4.3 Simulating Dephasing

#### 4.3.1 The Probabilistic Model for Dephasing

Dephasing, as mentioned in Section 3.5 of Chapter 3, results in a chance of a phase shifter giving 0 phase shift, which must be accounted for in the simulations. The first method we used to simulate this was a probabilistic model, where for example, a perfect MZI would go from Equation 2.11 to,

$$MZI = \alpha_0 i e^{i\theta} \begin{bmatrix} e^{i\phi} \sin\theta & \cos\theta \\ e^{i\phi} \cos\theta & -\sin\theta \end{bmatrix}, \alpha_1 i e^{i\theta} \begin{bmatrix} \sin\theta & \cos\theta \\ \cos\theta & -\sin\theta \end{bmatrix}, \alpha_2 i \begin{bmatrix} 0 & 1 \\ e^{i\phi} & 0 \end{bmatrix}, \alpha_3 i \begin{bmatrix} 0 & 1 \\ 1 & 0 \end{bmatrix}, \quad (4.1)$$

where there are four possible MZIs corresponding to; both phase shifters on, one or the other off, or both off. Here  $\alpha_i$  is the probability of each case occurring. These probabilities are calculated through the calculation of  $T - |t|^2$ , giving us the probability of getting an incoherent interaction with 0 phase shift. To calculate the chance of a phase shifter being on, we simply take  $1 - (T - |t|^2)$ . Thus, for example,  $\alpha_1$  in

Equation 4.1, corresponding to an incoherent interaction for  $\phi$  and coherent for  $2\theta$ , can be calculated by taking  $T - |t|^2$  for  $\phi$ , and multiplying this by  $2\theta$ 's  $1 - (T - |t|^2)$ . Here we use Equations 3.58 and 3.55 for  $T$  and  $|t|^2$ . We also factor these probabilities into the global phases in the  $D'$  matrix, providing  $N^2$  possibilities. From the probabilistic MZIs and  $D'$ , we recombine the unitary as shown in Section 2.1.4, such that all possible unitaries are calculated with their associated probabilities. The circuit infidelity is then the sum of the infidelity for each possible unitary multiplied by its associated probability.

Although we use  $\beta$ 's for coupling and directionality, we still write dephasing in terms of  $\Gamma_{dp}$ , which factors into phase shift and transmission through  $\Gamma_2$ , as shown in Section 3.4. When we simulate dephasing, again we choose a central value for all phase shifters in the mesh which we label  $\Gamma_{dp}$ , then sample from a normal distribution with a standard deviation of 5% of the central value. This again works the same as nanophotonic imperfections as shown in Figure 4.1, except it applies to each phase shifter instead of each MZI.

While we know we can achieve near-zero dephasing in QDs (Section 3.5), we simulated the infidelity dependence on dephasing to determine how important it is to have QDs with low dephasing in our circuits. Thus, we performed circuit infidelity simulations for  $N = 2, 3, 4$ , including nanophotonic imperfections, spanning  $\Gamma_{dp} = 10^{-4}\Gamma$  to  $\Gamma_{dp} = 0.10\Gamma$ , where each point on the lines is the beta fit to 100 Haar random unitaries. Figure 4.6 displays this data for the imperfect and optimized results, which also includes nanophotonic imperfections.

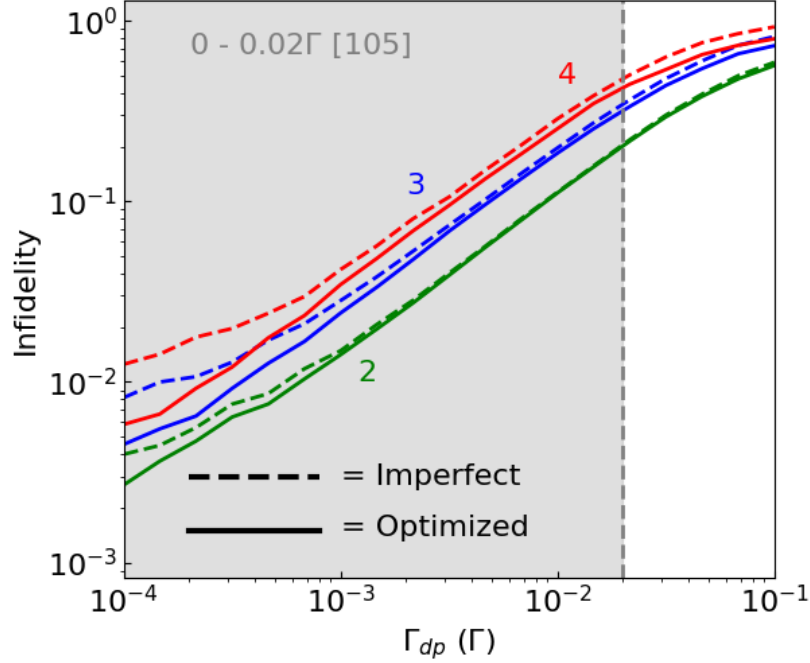


Figure 4.6: Dephasing matrix infidelity simulations with the complete probabilistic model. Each point is taken from the beta fit to 100 Haar random unitaries. Results are shown for  $N = 2$  (green),  $N = 3$  (blue),  $N = 4$  (red), from  $\Gamma_{dp} = 10^{-4}\Gamma$  to  $\Gamma_{dp} = 0.10\Gamma$ , including nanophotonic imperfections as listed in Section 4.1. Imperfect (dashed) and optimized (solid) data are both shown. The gray region shows the state-of-the-art dephasing, which has a central value of  $\Gamma_{dp} = 0\Gamma$  with an error up to  $\Gamma_{dp} = 0.02\Gamma$  [105].

We see from Figure 4.6 that at very low dephasing, the optimizer can still adjust for imperfections, but even at dephasings as low as  $\Gamma_{dp} = 10^{-3}\Gamma$ , the optimizer can struggle to find a better solution than the imperfect case. This is a somewhat surprising result, as even though every MZI will have a portion that acts differently than programmed, we expected optimization could still be made to the all-phases-on portion and that it could adjust for the other portions accordingly. Additionally, even at dephasing as low as  $10^{-4}\Gamma$ , we still have nearly 3 times the infidelity for  $N = 2$  as with only nanophotonic imperfections. It is possible that dephasing simply adds that

much error to the circuit even at  $10^{-4}\Gamma$ , however, for a QD with  $D = 1$ ,  $\beta = 1$  with  $10^{-4}\Gamma$  and  $\Delta_P = 0$ , we have an incoherence probability of only  $T - |t|^2 = 8 \times 10^{-4}$ , indicating only a 0.08% chance of a phase shifter being off, meaning for  $N = 2$ , this would likely never happen across 100 sampled unitaries. Thus, it seems more likely that the optimizer is not the best optimization scheme for this dephasing model, where a different optimizer could potentially improve results.

Additionally, this model has computational limitations that make it difficult to simulate larger circuits. Since each mesh has  $N(N-1)/2$  MZIs, each with 4 possibilities, and  $N$  global phase shifters, the total possibilities to be calculated is  $4^{N(N-1)/2}N^2$ , which scales into billions of options at as low as  $N = 6$ . In terms of simulations, this creates both a memory and runtime issue, which did not allow us to use this model for larger  $N$ , limiting results to  $N = 4$ . Thus, we determined that this had to be modeled through sampling instead of using the complete model.

#### 4.3.2 Dephasing Using Monte-Carlo Simulations

To numerically simulate phases that can be on or off, we can use a Monte-Carlo simulation, where we sample across many iterations to come to an accurate result. To do this with dephasing, for each sample we randomly pick if each phase is on or off, following its probability as described in the previous section, and build the unitary. For every unitary, the fidelity is calculated and the overall fidelity is taken as the average across all samples.

To use this method, we had to ensure we had enough samples to accurately model the system, so we tested from 10 to 10000 samples, as shown in Figure 4.7. For this testing data we used  $\Gamma_{dp} = 0.001\Gamma$  and we also included a spectral diffusion of

$\sigma_{SD} = 0.01\Gamma$ , which also factors into the model through a Monte-Carlo simulation as described in the next section. This was run for  $N = 3, 4, 6, 10$ , but for figure clarity, we only include  $N = 4$ , due to overlapping error bars. Each point is from the beta fit to the imperfect circuit infidelities for 100 Haar random unitaries, with the error bars as the standard deviations of the fit. Note that we only include the imperfect results here, as the variance between sample numbers should be identical for the optimized case, and the imperfect has faster runtime. Simulations with  $\Gamma_{dp} = 0.01\Gamma$  and  $\Gamma_{dp} = 0.1\Gamma$  for  $N = 4$ , as well as simulations for  $N = 3, 6, 10$  with  $\Gamma_{dp} = 0.001\Gamma$ , are shown in Section B.3, showing this testing was not biased for a specific dephasing or circuit size.

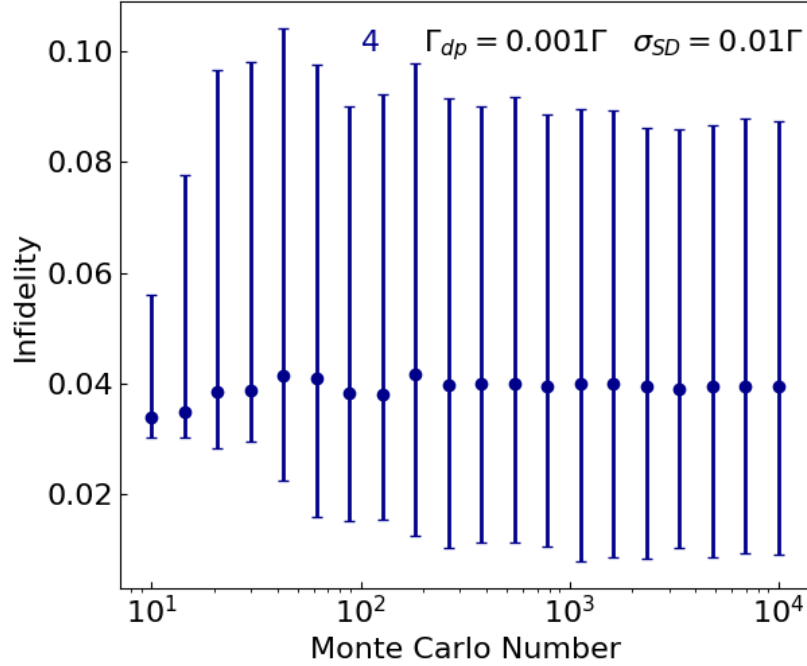


Figure 4.7: Imperfect infidelity results spanning 10 to 10000 Monte-Carlo simulations for  $N = 4$  circuits. Each point is taken from the beta fit to 100 Haar random unitaries, and the error bars are the standard deviations of the fit. This simulation was performed with  $\Gamma_{dp} = 0.001\Gamma$  and  $\sigma_{SD} = 0.01\Gamma$ .



From this data, we determined that 300 or more samples would be sufficient, as this is where the infidelity levels out and error bars no longer fluctuate, but we chose 500 samples per unitary to be conservative. It may be counter-intuitive that as we increase the number of trials error bars do not decrease in size, but this indicates that we are at the limit where the variance of infidelity between the 100 different unitary matrices for each point is more substantial than the variance from the Monte-Carlo simulations. In fact, in Section B.3, Figure B.2 shows the standard deviation for  $\Gamma_{dp} = 0.001\Gamma$  between samples within each unitary for  $N = 3, 4, 6, 10$  where this also levels out near 300 Monte-Carlo samples, indicating that the variance is accurately coming from the dephasing and spectral diffusion instead of the random sampling. Note that Section B.3 also includes the same standard deviation figures for  $\Gamma_{dp} = 0.01\Gamma$ , and  $\Gamma_{dp} = 0.10\Gamma$ .

To ensure accurate results, we also compared our 500 sample Monte-Carlo model to the complete probabilistic model for  $N = 2, 4$ , as shown in Figure 4.8, which compares the imperfect and optimized results across  $\Gamma_{dp} = 10^{-4}\Gamma$  to  $\Gamma_{dp} = 0.10\Gamma$  for the beta fit to 100 Haar random unitaries at each point where we see that the models agree within error at all points. We do however see that the Monte-Carlo model for  $N = 2$  outperforms in the optimized case. However, as explained above, the results for  $\Gamma_{dp} = 10^{-4}\Gamma$  for  $N = 2$  should have better performance than both these models indicate. Thus, we can determine that the Monte-Carlo model is accurate, and only outperforms the probabilistic case for  $N = 2$  because the optimizer performs better with it. Note that these were run on different sets of 100 unitaries which could also cause some of the differences. There could also be some inconsistency in the  $N = 2$  data for the Monte-Carlo simulation, due to the convergence of the optimization, as

explained in Section B.2.

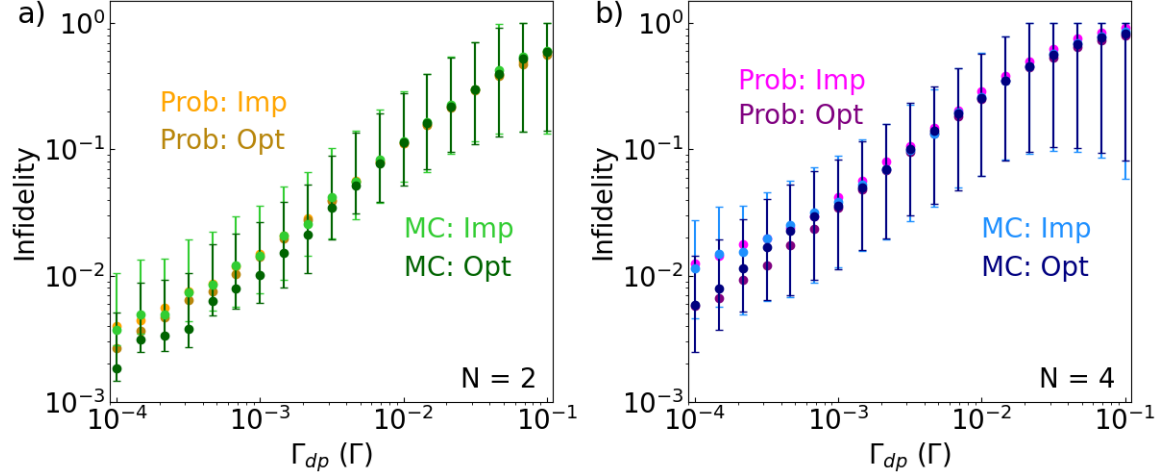


Figure 4.8: Comparison between dephasing results from the probabilistic complete model and Monte-Carlo simulations for both imperfect and optimized data. All data is taken from a beta fit to the infidelity of 100 Haar random unitaries. The standard deviation on the beta fit is shown for each point from the Monte-Carlo simulations. Results are spanned across  $\Gamma_{dp} = 10^{-4}\Gamma$  to  $\Gamma_{dp} = 0.10\Gamma$ . (a)  $N = 2$  simulations. (b)  $N = 4$  simulations.

With Monte-Carlo simulations, we were able to simulate results for higher  $N$ , allowing us to determine dephasing performance on larger circuits. Thus, we again simulated  $\Gamma_{dp} = 10^{-4}\Gamma$  to  $\Gamma_{dp} = 0.10\Gamma$  in Figure 4.9, with imperfect and optimized infidelities for  $N = 2, 6, 10$  similar to Figure 4.6. We see that larger circuits follow the same trends as  $N = 2, 3, 4$ , where we have optimization at low dephasing, and cannot improve much upon the imperfect at higher dephasing. It is clear from these results that even minor amounts of dephasing cause significant detriments to circuit infidelities. We do not have  $\mathcal{I} < 10^{-2}$  for  $N = 6$  or  $N = 10$  circuits at any points, indicating 0 dephasing will be required for fault-tolerant computing. However, this has been shown to be achievable for chiral QDs [105].

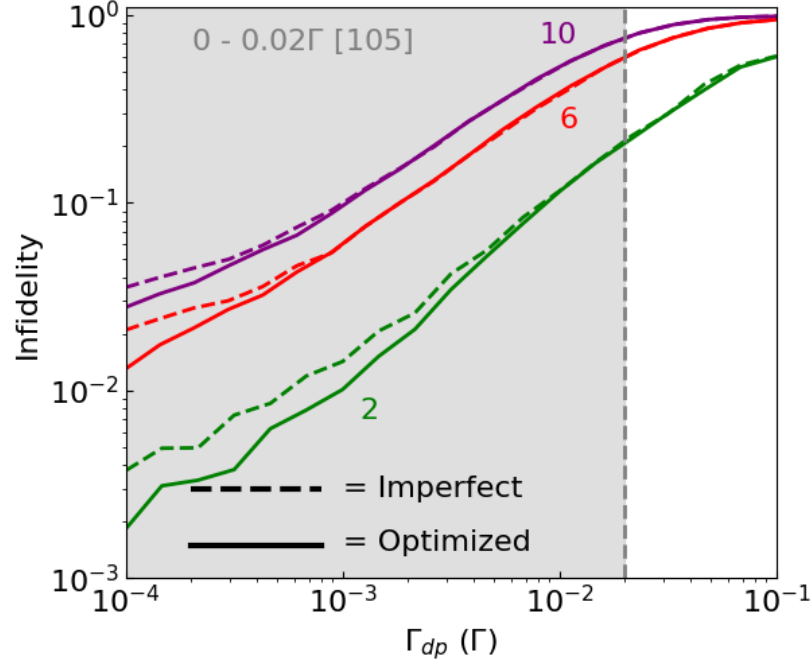


Figure 4.9: Dephasing infidelity simulation results from  $\Gamma_{dp} = 10^{-4}\Gamma$  to  $\Gamma_{dp} = 0.10\Gamma$  for the Monte-Carlo dephasing model as described in Section 4.3. Nanophotonic imperfections are also included as listed in Section 4.1. All points are beta fits to 100 Haar random unitaries with the imperfect data shown as dashed lines and the globally optimized data as solid lines. The gray region shows the state-of-the-art dephasing, which has a central value of  $\Gamma_{dp} = 0\Gamma$  with an error up to  $\Gamma_{dp} = 0.02\Gamma$  [105].

## 4.4 Simulating Spectral Diffusion

### 4.4.1 The Convolutional Model for Spectral Diffusion

Spectral diffusion, like dephasing, has a shot-to-shot effect on the phase shifts, shifting detuning and often modeled with a convolution, as mentioned in Chapter 3. In Figure 4.10 we plot an example detuning and phase shift distribution over 10000 samples with  $\sigma_{SD} = 0.30\Gamma$  for an otherwise perfect QD phase shifter with a set detuning of  $\Delta_P = 0.1\Gamma$ . This figure depicts why the convolutional model for spectral diffusion

is invalid for this application since for some near-zero detuning, the phase shift will fluctuate around 180 and  $-180$  degrees depending on the sign of the detuning after spectral diffusion. If the convolutional model was used for this, the average phase shift would be 0 degrees, which does not accurately represent the phase shift in our circuit.

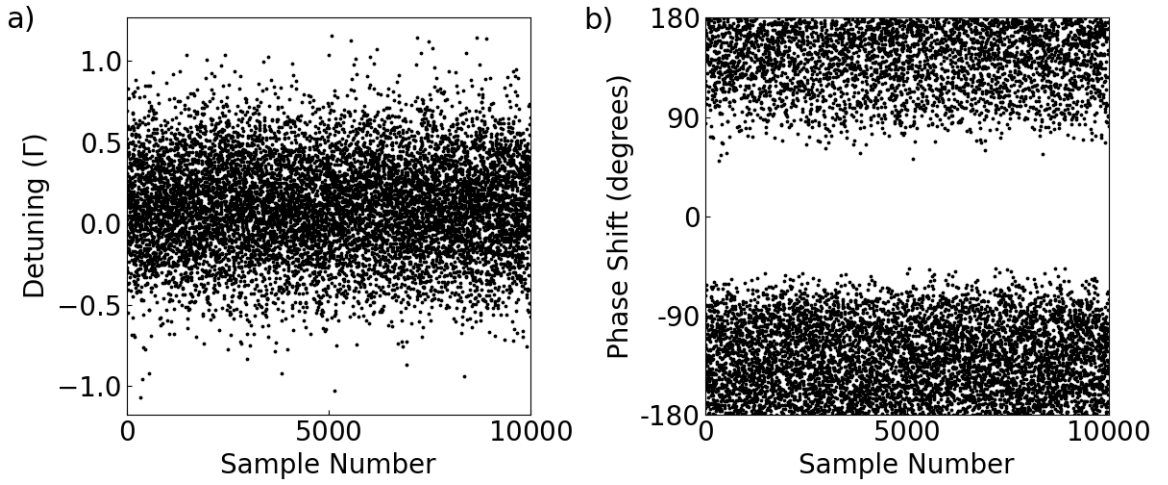


Figure 4.10: Example detuning and phase shift transformations from spectral diffusion of  $\sigma_{SD} = 0.30\Gamma$  for  $\Delta_P = 0.1\Gamma$  over 10000 samples. (a) Detuning distribution. (b) Phase shift distribution for an otherwise perfect QD ( $D = 1$ ,  $\beta = 1$ ,  $\Gamma_{dp} = 0$ ).

#### 4.4.2 Spectral Diffusion Using Monte-Carlo Simulations

Instead of a convolution, we can accurately model spectral diffusion with a Monte-Carlo simulation, where each sample chooses a detuning shift by sampling from the spectral diffusion's normal distribution. Note that Figure 4.7 in the previous section includes spectral diffusion, so we can again conclude that 500 Monte-Carlo samples are sufficient.

With this simulation method, we can determine the effects of spectral diffusion on

circuit performance to determine spectral diffusion limits on QDs for our architecture. To do this, we simulated imperfect and optimized circuit infidelities for a range of spectral diffusions from  $\sigma_{SD} = 10^{-4}\Gamma$  to  $\sigma_{SD} = 0.30\Gamma$  for  $N = 2, 6, 10$  circuits, as shown in Figure 4.11. We see that at  $\sigma_{SD} \leq 0.01\Gamma$ , we get optimization of up to an order of magnitude, and in fact for  $\sigma_{SD} \leq 0.01\Gamma$  in  $N = 6, 10$  circuits, spectral diffusion has no effect. We also see that the  $N = 2$  optimized results near zero spectral diffusion agree with  $N = 2$  infidelity for nanophotonic imperfections as listed in Section 4.1. The  $N = 2$  case has some odd fluctuations between points that we can attribute to convergence issues as described in Section B.2. Infidelity is also below the fault-tolerant limit for  $\sigma_{SD} \leq 0.01\Gamma$  for circuits up to  $N = 10$ . For  $\sigma_{SD} \geq 0.05\Gamma$ , the size of detuning fluctuations from  $\sigma_{SD}$  are too large to overcome, resulting in poor optimization. However, as listed in Section 3.5 of Chapter 3, spectral diffusion can be fully eliminated, so implementations of this architecture should be able to work in a range that allows for good performance and scalability.

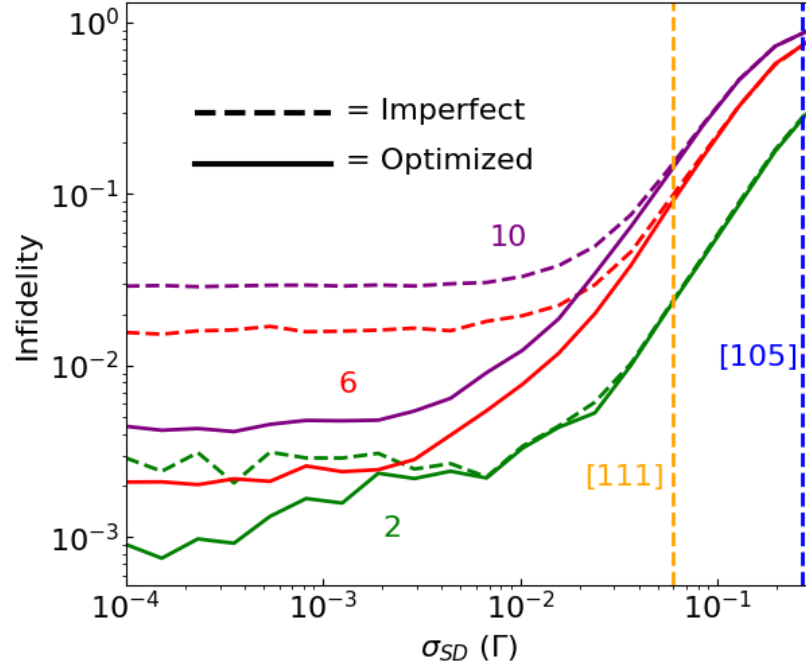


Figure 4.11: Circuit infidelity simulation results for circuits of size  $N = 2$  (green),  $N = 6$  (red),  $N = 10$  (purple) spanning across spectral diffusions of  $\sigma_{SD} = 10^{-4}\Gamma$  to  $\sigma_{SD} = 0.30\Gamma$ , including nanophotonic imperfections as listed in Section 4.1. All points are beta fits to 100 Haar random unitaries with the imperfect data shown as dashed lines and the globally optimized data as solid lines. The orange line is a typical quantum dot implementation where  $\sigma_{SD} = 0.06\Gamma$  [111], and the blue is an implementation where  $\sigma_{SD} = 0.27\Gamma$  [105].

#### 4.5 Simulated Circuit Scalability

By combining all the imperfections we've analyzed, we can simulate the performance and scalability of our implementation on Haar random unitaries to determine the validity of this architecture. To do this, we consider three different cases. The first case is only nanophotonic imperfections, as listed in Section 4.1, which we can use to compare with the performance of circuits with QD imperfections. The second is the state-of-the-art (SOTA) imperfections, where we take the best imperfections that

have been achieved for QDs. For this, we chose the imperfections:  $\{\Gamma_{dp} = 0\Gamma$  [105],  $\sigma_{SD} = 0\Gamma$  [42, 106],  $\beta = 0.98$  [44],  $D = 0.95$  [104]  $\}$ , which we describe in Section 3.5 of Chapter 3. We also consider a “Typical” case, which has standard imperfections that have been achieved by multiple sources. For this case our parameters are  $\{\Gamma_{dp} = 0.01\Gamma$  [105],  $\sigma_{SD} = 0.06\Gamma$  [111],  $\beta = 0.90$  [97],  $D = 0.90$  [97]  $\}$ . Note that since multiple implementations achieve  $\Gamma_{dp} \approx 0\Gamma$ , we chose  $\Gamma_{dp} = 0.01\Gamma$  as a typical sample from the 0 – 2% uncertainty in [105]. Note that both these cases also include our chosen nanophotonic imperfections.

By simulating SOTA imperfections, we can determine the validity and scalability of this architecture for the best possible QD implementation, indicating what is possible with the architecture and how that compares to using classical phase shifters (nanophotonic case). The simulation of the typical case is included to show what currently may be more realistic for this architecture, as combining multiple well-performing quantum dots onto the same circuit is still very difficult, so building this architecture with SOTA QDs is still likely a few years into the future.

To determine these performances, we simulated 100 Haar random unitaries for  $N = 2$  to  $N = 10$  for the three imperfection cases, as well as the typical case with no spectral diffusion or dephasing, and the typical case with no spectral diffusion. We included these last two cases to identify the contributions of each QD imperfection to the infidelity. We then performed a beta fit to the 100 unitaries at each point to provide estimated average circuit infidelities for random quantum circuits, plotting the optimized results in Figure 4.12.

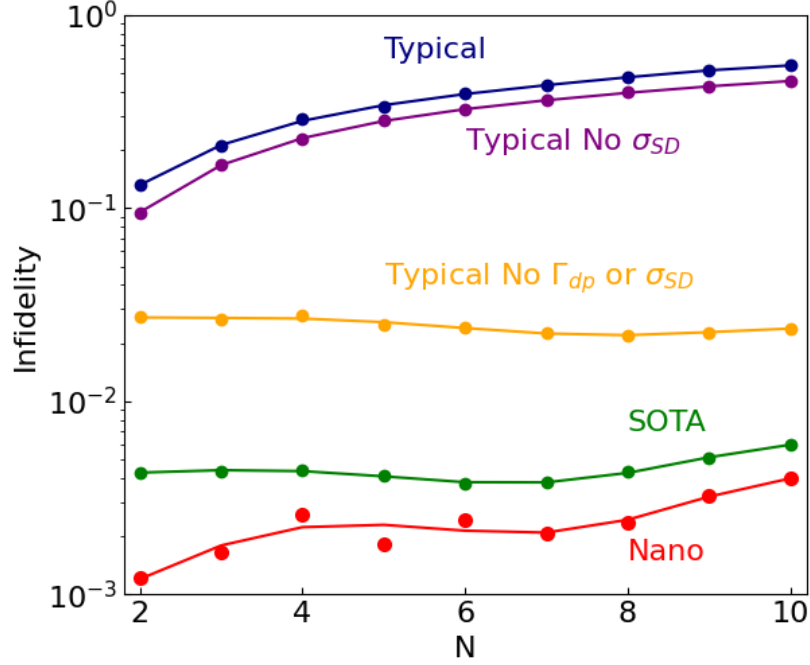


Figure 4.12: Circuit infidelities from  $N = 2$  to  $N = 10$  for different levels of imperfections. Each point is the mean of a beta fit to 100 Haar random unitaries and depicts the data post-global optimization. Imperfections are built up from nanophotonic (red) to state-of-the-art (green), to the typical case (navy). We also include the typical without spectral diffusion (purple) and without both dephasing and spectral diffusion (orange). The lines are 5th-degree polynomial fits to the data that are meant only to guide the eye and do not represent data.

The results from Figure 4.12 are promising for our architecture, as we see that the SOTA case achieves  $\mathcal{I} < 10^{-2}$  for all sizes up to  $N = 10$ , which would enable fault-tolerant quantum computing. Additionally, for  $N = 2 - 8$ , we see no notable difference in infidelity for SOTA. It is only when reaching circuit sizes of  $N = 9, 10$ , that a small infidelity increase becomes evident. This indicates that the optimizer performs well on large circuits with SOTA imperfections, providing promising circuit scalability. Comparing this to the nanophotonic case, we see that while infidelities are significantly better than SOTA at small circuit sizes, the gap decreases as circuits



become larger. This indicates that with the increased number of parameters that come from larger circuits, the optimization is able to reduce the impact of QD imperfections, making the addition of QDs nearly irrelevant for performance in large circuits.

We can also conclude from Figure 4.12 that none of the typical cases have low enough infidelity to achieve fault-tolerant computing. However, we do see an interesting breakdown of the effects of each imperfection in the circuit. Comparing the typical data with and without spectral diffusion, we see that  $\sigma_{SD} = 0.06\Gamma$  has a very minimal effect on infidelity. In fact, dephasing, as expected from the results in Section 4.3, is the imperfection that hinders performance and scalability the most, with  $\Gamma_{dp} = 0.01\Gamma$  causing  $N = 2$  circuits to have  $\mathcal{I} > 0.1$ . This is partially caused by the difficulty it adds to optimization, as the chance of having some phase shifts off makes circuits very difficult to optimize. Without both spectral diffusion and dephasing (orange line), the typical coupling and directionality can be well-optimized, showing that increasing circuit size counter-intuitively provides a decrease in infidelity.

Thus, with SOTA imperfections this architecture becomes a viable path toward large-scale fault-tolerant QPICs. Additionally, we have shown that if spectral diffusion and dephasing can be minimized, our novel global optimization method implements a significant performance increase through phase shift reconfiguration.

## 4.6 Two-Qubit Example Circuit Simulations

In the previous sections we have characterized the performance of this architecture on arbitrary quantum circuits. However, we also want to characterize performance for some example circuits, since for quantum algorithms, we usually have specific gates instead of random unitary matrices. Here, we consider the unheralded CNOT and

CZ gates, as outlined in Chapter 2, to benchmark this performance.

#### 4.6.1 CNOT and CZ Matrix Infidelity

For both example circuits, we began by simulating their matrix infidelities spanning across dephasing for the three imperfection cases (Nanophotonic, SOTA, Typical) as listed in Section 4.5. These dephasing simulations allow us to determine if performance and optimization with dephasing can improve with simpler example circuits where many phase shifters are 0 in the ideal case (as is evident from the plentiful zeros in the unheralded CNOT and CZ matrices shown in Equations 2.21 and 2.22).

To simulate this we spanned from  $\Gamma_{dp} = 10^{-4}\Gamma$  to  $\Gamma_{dp} = 0.10\Gamma$ , and took the beta fit for each point from the infidelities of 100 unheralded CNOTs as shown in Figure 4.13. We repeated this for the unheralded CZ as shown in Figure 4.14. We see that both gates have nearly identical performances, despite the CZ being the simpler<sup>3</sup> gate.

---

<sup>3</sup>The CZ is considered “simpler” since the ideal implementation only uses three MZIs with non-zero phase shifts, compared to 5 for the CNOT gate.

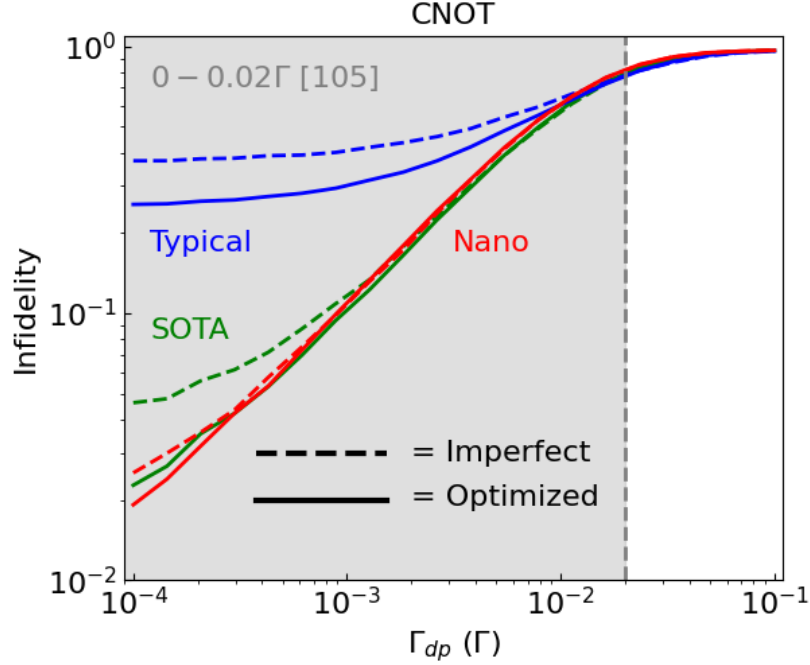


Figure 4.13: Unheralded CNOT imperfect and optimized matrix infidelities for nanophotonic (red), state-of-the-art (green), and typical (blue) imperfections, as listed in Section 4.5 across  $\Gamma_{dp} = 10^{-4}\Gamma$  to  $\Gamma_{dp} = 0.10\Gamma$ . The points on each line are determined from a beta fit to the infidelities of 100 CNOT matrices. The gray region shows the state-of-the-art dephasing, which has a central value of  $\Gamma_{dp} = 0\Gamma$  with an error up to  $\Gamma_{dp} = 0.02\Gamma$  [105].

By comparing the red nanophotonic lines in Figures 4.13 and 4.14 to  $N = 6$  in Figure 4.9, we can see that performance is slightly worse for the CNOT and CZ compared to average  $N = 6$  circuits. This could be caused by the importance of the non-zero phase shifters in the circuit since there are only a few MZIs in the mesh with non-zero phase shifts, so with one of these phase shifts off performance could be massively affected. However, we expected the optimizer to adjust the many redundant phase shifters in these meshes to improve performance, which did not come through in the results. For both circuits the SOTA case is also near-identical

in performance to the nanophotonic implementation after optimization, indicating that we can use QD phase shifters for these gates without hindering performance. In fact, the optimization for both typical and SOTA QD imperfections is better than the nanophotonic case, indicating that for low dephasing, optimization on other QD imperfections is not limited, unlike optimization on nanophotonic imperfections.

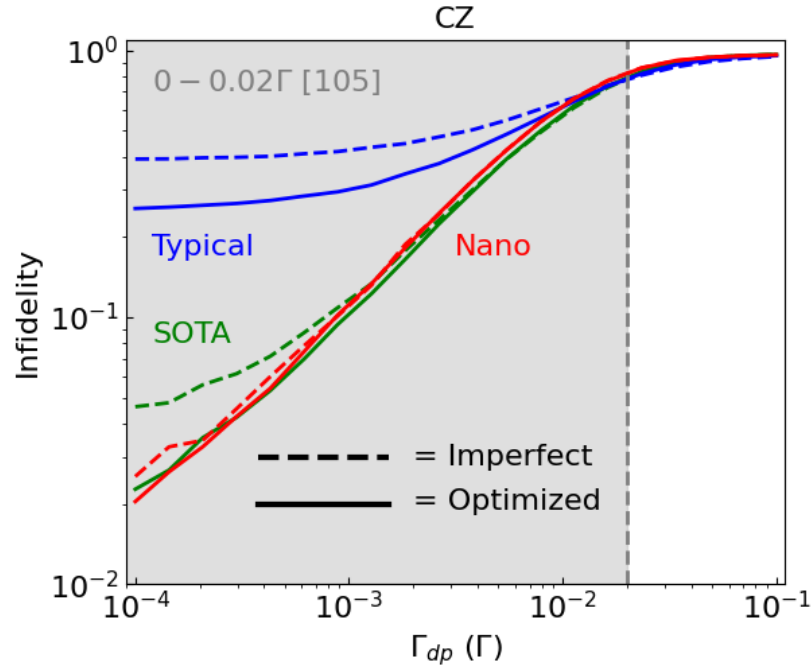


Figure 4.14: Unheralded CZ imperfect and optimized matrix infidelities for nanophotonic (red), state-of-the-art (green), and typical (blue) imperfections, as listed in Section 4.5 across  $\Gamma_{dp} = 10^{-4}\Gamma$  to  $\Gamma_{dp} = 0.10\Gamma$ . The points on each line are determined from a beta fit to the infidelities of 100 CZ matrices. The gray region shows the state-of-the-art dephasing, which has a central value of  $\Gamma_{dp} = 0\Gamma$  with an error up to  $\Gamma_{dp} = 0.02\Gamma$  [105].

### 4.6.2 CNOT and CZ Output Infidelity

While matrix infidelity is a fitting method of characterizing circuit performance for random unitaries, example unitaries allow us to look directly at expected input-output pairs to determine output infidelity. This is easier to measure in hardware than characterizing every element of your circuit to determine its transfer matrix. For this implementation, we use post-selected output infidelity as the cost function for the optimizer (as described in Section 2.3 with Equation 2.30). To determine these infidelities we calculate the matrix permanent for the unheralded CZ and CNOT with two photons, as described in Section 2.1, and truncate these to  $4 \times 4$  matrices where only the entries that correspond to the computational Z-basis input and output states,  $\{|00\rangle, |01\rangle, |10\rangle, |11\rangle\}$ , are left in the matrix. This matrix is then normalized to provide the post-selected  $4 \times 4$  matrix since we are post-selecting on the computational basis. In hardware, this means if output photons are measured that correspond to a non-basis state, the result is discarded. This is similar to our infidelities excluding balanced losses, as we are ignoring the count rate and focusing on accuracy.

For optimization, the post-selected output fidelity is averaged over the Z-basis inputs and the X-basis inputs of  $\{|++\rangle, |+-\rangle, |-+\rangle, |--\rangle\}$  (see Section 2.1), which is done to ensure local phases are factored into the optimization. Without including the X-basis, Equation 2.30 would for example allow the CZ gate to train as the identity matrix, so this must be included.

To simulate these circuits we consider the three imperfection cases again as listed in Section 4.5. For each of these cases, for both the CNOT and CZ, we take 100 iterations, for each of which the typical case, with dephasing and spectral diffusion,

performs 500 Monte-Carlo simulations. We first average the post-selected  $4 \times 4$  matrices over all Monte-Carlos, and then average these 100 matrices to determine an overall post-selected  $4 \times 4$  matrix for the circuit. This is done for both the imperfect and optimized cases, allowing us to plot Figure 4.15 for the CNOT and Figure 4.16 for the CZ. These figures display  $4 \times 4$  grids that represent the post-selected matrices, where the size of each square indicates the amplitude of that matrix entry, and the color indicates the phase shift on that entry. For presentation's sake, we have taken out a global phase from all entries based on the phase of entry  $\langle 00|00 \rangle$  so that phase shifts are clear. The expected  $4 \times 4$  grid for the CNOT and CZ should look like the matrices from Equations 2.6 and 2.7, respectively. Infidelities are listed with each matrix, corresponding to the average output state conditional infidelity for the matrix (each calculated with Equation 2.30) across all input-output pairs in the Z and X bases.

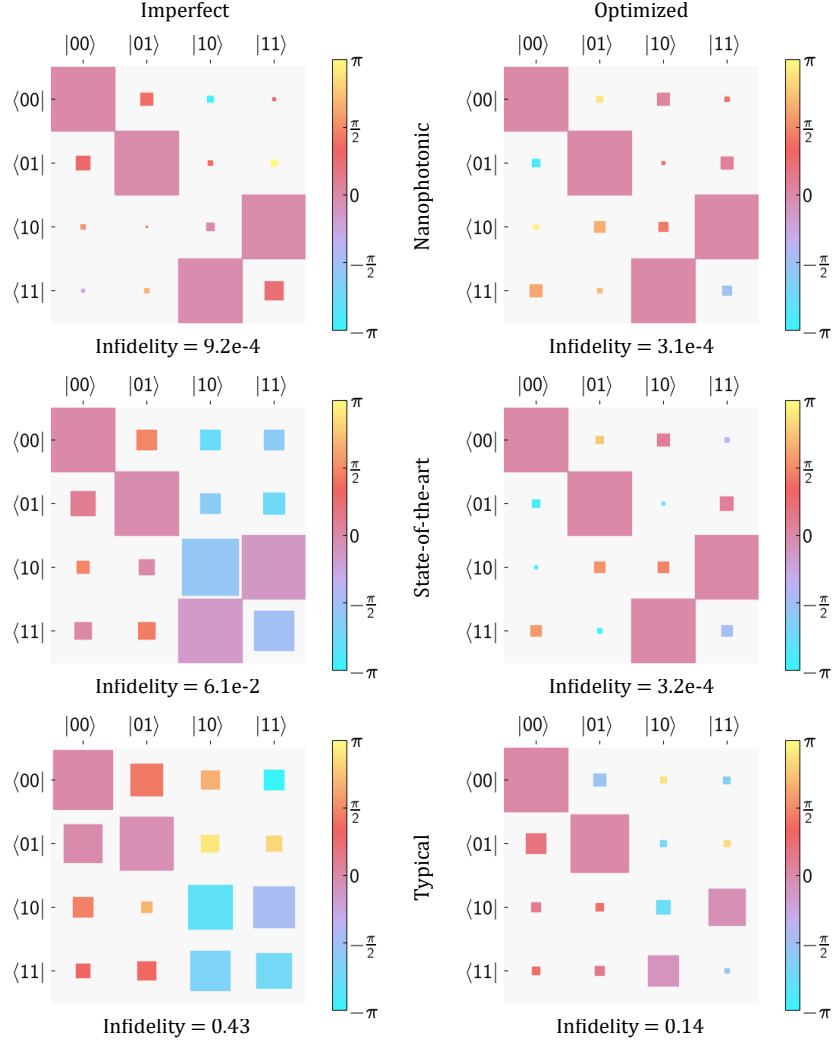


Figure 4.15: CNOT post-selected imperfect and optimized  $4 \times 4$  matrices and their associated conditional infidelities for nanophotonic, state-of-the-art, and typical imperfections. The boxes in each grid indicate the amplitude of that matrix entry, and the color corresponds to the phase, as depicted by the color bars.

Looking at Figures 4.15 and 4.16 we see that the CNOT and CZ are both able to perform nearly perfectly ( $\mathcal{I} \approx 10^{-4}$ ) with nanophotonic and SOTA imperfections after optimization. For the SOTA case, the conditional output infidelity for both circuits was optimized by two orders of magnitude, eliminating all QD imperfection

effects on performance. Thus if this architecture can be implemented with SOTA QD imperfections, while count rate will be lower due to higher overall loss, circuit accuracy will not be affected by the addition of quantum dots. This suggests that this architecture is viable for the implementations of CNOT and CZ gates. Note that the performance for the CZ gate is slightly better in all cases than the CNOT, likely since it is a simpler gate to implement. With typical imperfections, the performance of both CNOT and CZ gates is poor with  $\mathcal{I} > 0.10$ , but the optimization is significantly better than when matrix infidelity was used as a cost function, as we can see from comparing these results to Figures 4.13 and 4.14. The massively improved optimization on SOTA and typical cases compared to matrix infidelity suggests that our global optimization scheme may be best implemented using output state infidelities as the cost function for all circuits.



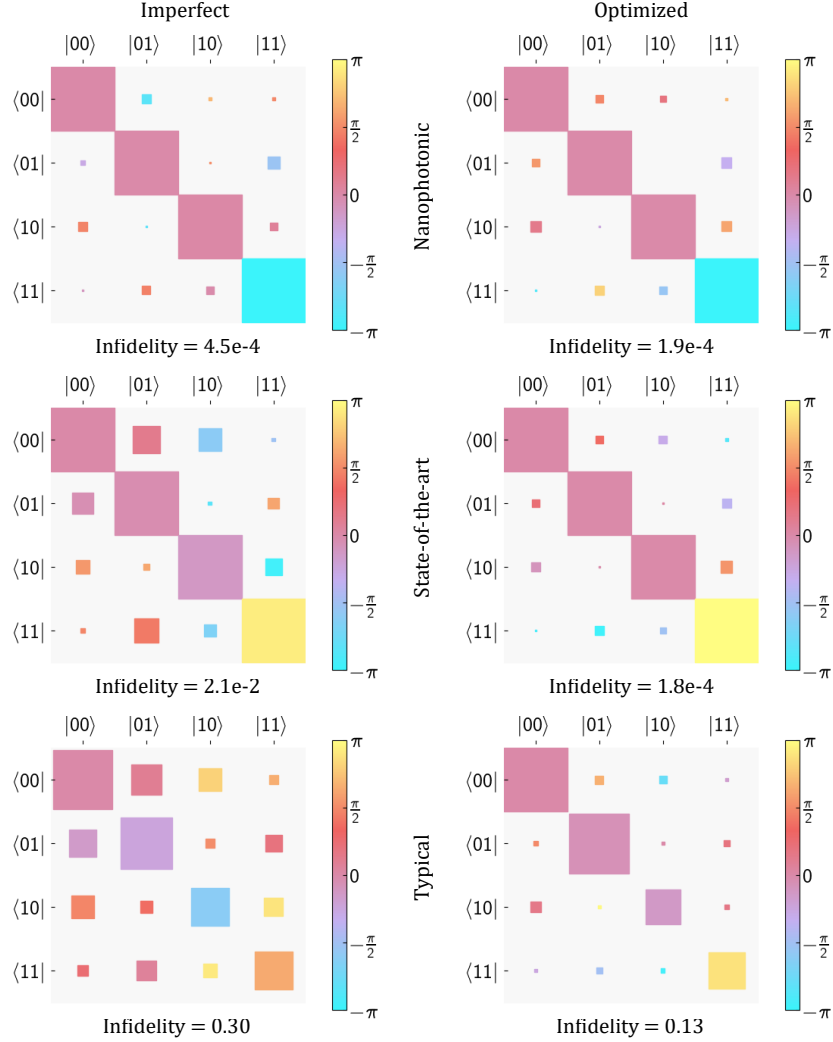


Figure 4.16: CZ post-selected imperfect and optimized  $4 \times 4$  matrices and their associated conditional infidelities for nanophotonic, state-of-the-art, and typical imperfections. The boxes in each grid indicate the amplitude of that matrix entry, and the color corresponds to the phase, as depicted by the color bars.

## Chapter 5

### Conclusions and Outlook

#### 5.1 Summary

Quantum information technology has and will continue to provide solutions to problems that are currently unsolvable with classical computing. We have seen that we can build quantum circuits on-chip that leverage photons as information, providing low-noise ultra-fast processing, and integration with classical computational hardware. However, to build large-scale quantum photonic integrated circuits, the architecture needs to be compatible with single-photon sources/detectors, and be efficiently scalable. In this thesis, we are the first to propose and simulate the use of quantum dots as phase shifters for on-chip quantum photonic circuits, which would provide more compact architecture, increase processing time through faster reconfigurability, and provide cryogenic compatibility.

We have shown that by leveraging chiral quantum dots, we can achieve directional photon scattering with phase shifts ranging from  $-\pi$  to  $\pi$ , and that this phase shift is reconfigurable through adjustments to the quantum dot resonant frequency. We have also shown how we can leverage this phase shift reconfigurability to program

any  $N \times N$  quantum circuit. We then considered the imperfections that come from quantum dots: coupling, directionality, spectral diffusion, and dephasing, as well as nanophotonic imperfections: beam splitter error, and nanophotonic loss, and their effects on the performance of these circuits. Optimization techniques have been used to adjust for these imperfections, and in this work, we proposed a global optimization technique that uses the BOBYQA algorithm with circuit infidelity as the cost function.

We then simulated and optimized random quantum circuits up to  $N = 10$ , where we saw that our optimizer could improve circuit infidelity by up to an order of magnitude. We also saw that with state-of-the-art imperfections, our architecture can reach the performance threshold of  $\mathcal{I} < 10^{-2}$  for fault-tolerant quantum computing, and that through optimization, we can nearly eliminate all loss of performance caused by quantum dot imperfections. These simulations show excellent scalability, with optimization improving with circuit size to adjust for increased imperfections. We do however note that our method struggles to optimize and perform well with high dephasing and spectral diffusions, meaning hardware implementations will need to ensure they limit these imperfections for optimal performance. Lastly, we looked at the unheralded CNOT and CZ as example  $6 \times 6$  circuits, where we optimized on the conditional output state infidelity, achieving near-perfect performance for state-of-the-art quantum dot imperfections. Here we also noted that the optimization was more successful with a cost function that used output state infidelity instead of matrix infidelity. These results allowed us to conclude that this architecture is both viable and scalable, providing a pathway toward implementations of large-scale fully-quantum photonic integrated circuits.

## 5.2 Future Work

The work in this thesis proposes a novel quantum circuit architecture that uses a global optimization method that had not yet been considered for this application. This naturally provides many paths worth investigating. In this work we only simulated these circuits up to  $N = 10$ , but investigating performance for larger circuits such as  $N = 100$  or  $N = 1000$ , would provide more insight on the scalability of this architecture. It would also be beneficial to include the global  $D'$  phases into the global optimization, instead of optimizing them separately, to see if this could improve performance. Another path forward would be to investigate the use of different local and global optimization methods, like gradient-descent, which would allow us to benchmark the performance of our current optimization method. Implementing the optimization with different cost functions such as mean squared error, or arbitrary output state fidelity would also be beneficial to determine if this could improve performance. Additionally, this work only tested the simplest MZM architecture, so future work could also consider adding redundant components such as extra MZI layers or extra QD phase shifters, which has been shown to improve optimization in existing implementations.

It would also be a natural progression to attempt a hardware implementation of these circuits, starting small at  $N = 2$  for a single qubit gate, to determine if the performance in these simulations can translate to hardware as we expect. This could be done at telecom wavelength using InP quantum dots, allowing integration with telecommunications hardware, or using GaAs quantum dots, which is the most developed platform for high-quality QDs. However, to do this, some challenges would still need to be overcome such as high-quality site-selected QD growth. This could

eventually lead to larger-scale circuits, where we could also consider using real-time optimization on-chip to maximize performance.

## Bibliography

- [1] F. Arute, K. Arya, R. Babbush, D. Bacon, J. C. Bardin, R. Barends, R. Biswas, S. Boixo, F. G. Brandao, D. A. Buell, *et al.*, “Quantum supremacy using a programmable superconducting processor,” *Nature*, vol. 574, no. 7779, pp. 505–510, 2019.
- [2] L. S. Madsen, F. Laudenbach, M. F. Askarani, F. Rortais, T. Vincent, J. F. F. Bulmer, F. M. Miatto, L. Neuhaus, L. G. Helt, M. J. Collins, A. E. Lita, T. Gerrits, S. W. Nam, V. D. Vaidya, M. Menotti, I. Dhand, Z. Vernon, N. Quesada, and J. Lavoie, “Quantum computational advantage with a programmable photonic processor,” *Nature*, vol. 606, pp. 75–81, June 2022.
- [3] Z. Merali *et al.*, “First sale for quantum computing,” *Nature*, vol. 474, no. 7349, p. 18, 2011.
- [4] E. R. MacQuarrie, C. Simon, S. Simmons, and E. Maine, “The emerging commercial landscape of quantum computing,” *Nature Reviews Physics*, vol. 2, no. 11, pp. 596–598, 2020.
- [5] J. P. Dowling and G. J. Milburn, “Quantum technology: the second quantum revolution,” *Philosophical Transactions of the Royal Society of London*.

- Series A: Mathematical, Physical and Engineering Sciences*, vol. 361, no. 1809, pp. 1655–1674, 2003.
- [6] P. W. Shor, “Algorithms for quantum computation: discrete logarithms and factoring,” in *Proceedings 35th annual symposium on foundations of computer science*, pp. 124–134, Ieee, 1994.
- [7] C. Zalka, “Grover’s quantum searching algorithm is optimal,” *Physical Review A*, vol. 60, no. 4, p. 2746, 1999.
- [8] A. J. Daley, I. Bloch, C. Kokail, S. Flannigan, N. Pearson, M. Troyer, and P. Zoller, “Practical quantum advantage in quantum simulation,” *Nature*, vol. 607, no. 7920, pp. 667–676, 2022.
- [9] K. L. Brown, W. J. Munro, and V. M. Kendon, “Using quantum computers for quantum simulation,” *Entropy*, vol. 12, no. 11, pp. 2268–2307, 2010.
- [10] A. Ajagekar and F. You, “Quantum computing for energy systems optimization: Challenges and opportunities,” *Energy*, vol. 179, pp. 76–89, 2019.
- [11] A. Abbas, D. Sutter, C. Zoufal, A. Lucchi, A. Figalli, and S. Woerner, “The power of quantum neural networks,” *Nature Computational Science*, vol. 1, no. 6, pp. 403–409, 2021.
- [12] M. Schuld, I. Sinayskiy, and F. Petruccione, “The quest for a quantum neural network,” *Quantum Information Processing*, vol. 13, pp. 2567–2586, 2014.
- [13] P. W. Shor and J. Preskill, “Simple proof of security of the bb84 quantum key distribution protocol,” *Physical review letters*, vol. 85, no. 2, p. 441, 2000.

- [14] V. Scarani, H. Bechmann-Pasquinucci, N. J. Cerf, M. Dušek, N. Lütkenhaus, and M. Peev, “The security of practical quantum key distribution,” *Reviews of modern physics*, vol. 81, no. 3, p. 1301, 2009.
- [15] Y. Cao, J. Romero, and A. Aspuru-Guzik, “Potential of quantum computing for drug discovery,” *IBM Journal of Research and Development*, vol. 62, no. 6, pp. 6–1, 2018.
- [16] R. Orús, S. Mugel, and E. Lizaso, “Quantum computing for finance: Overview and prospects,” *Reviews in Physics*, vol. 4, p. 100028, 2019.
- [17] V. Giovannetti, S. Lloyd, and L. Maccone, “Advances in quantum metrology,” *Nature photonics*, vol. 5, no. 4, pp. 222–229, 2011.
- [18] R. Ur Rasool, H. F. Ahmad, W. Rafique, A. Qayyum, J. Qadir, and Z. Anwar, “Quantum computing for healthcare: A review,” *Future Internet*, vol. 15, no. 3, p. 94, 2023.
- [19] A. Bayerstadler, G. Becquin, J. Binder, T. Botter, H. Ehm, T. Ehmer, M. Erdmann, N. Gaus, P. Harbach, M. Hess, *et al.*, “Industry quantum computing applications,” *EPJ Quantum Technology*, vol. 8, no. 1, p. 25, 2021.
- [20] W. K. Wootters and W. H. Zurek, “The no-cloning theorem,” *Physics Today*, vol. 62, no. 2, pp. 76–77, 2009.
- [21] P. Kaye, R. Laflamme, and M. Mosca, *An introduction to quantum computing*. OUP Oxford, 2006.



- [22] D. Bouwmeester, J.-W. Pan, K. Mattle, M. Eibl, H. Weinfurter, and A. Zeilinger, “Experimental quantum teleportation,” *Nature*, vol. 390, no. 6660, pp. 575–579, 1997.
- [23] E. Knill, “Quantum computing with realistically noisy devices,” *Nature*, vol. 434, no. 7029, pp. 39–44, 2005.
- [24] S.-K. Liao, H.-L. Yong, C. Liu, G.-L. Shentu, D.-D. Li, J. Lin, H. Dai, S.-Q. Zhao, B. Li, J.-Y. Guan, W. Chen, Y.-H. Gong, Y. Li, Z.-H. Lin, G.-S. Pan, J. S. Pelc, M. M. Fejer, W.-Z. Zhang, W.-Y. Liu, J. Yin, J.-G. Ren, X.-B. Wang, Q. Zhang, C.-Z. Peng, and J.-W. Pan, “Long-distance free-space quantum key distribution in daylight towards inter-satellite communication,” *Nature Photonics*, vol. 11, pp. 509–513, Aug. 2017.
- [25] J. M. Lukens and P. Lougovski, “Frequency-encoded photonic qubits for scalable quantum information processing,” *Optica*, vol. 4, pp. 8–16, Jan 2017.
- [26] M. Reck, A. Zeilinger, H. J. Bernstein, and P. Bertani, “Experimental realization of any discrete unitary operator,” *Physical Review Letters*, vol. 73, pp. 58–61, July 1994.
- [27] E. Knill, R. Laflamme, and G. J. Milburn, “A scheme for efficient quantum computation with linear optics,” *nature*, vol. 409, no. 6816, pp. 46–52, 2001.
- [28] N. Gisin and R. Thew, “Quantum communication,” *Nature photonics*, vol. 1, no. 3, pp. 165–171, 2007.
- [29] H.-L. Huang, D. Wu, D. Fan, and X. Zhu, “Superconducting quantum computing: a review,” *Science China Information Sciences*, vol. 63, pp. 1–32, 2020.

- [30] D. Kielpinski, C. Monroe, and D. J. Wineland, “Architecture for a large-scale ion-trap quantum computer,” *Nature*, vol. 417, no. 6890, pp. 709–711, 2002.
- [31] M. Jacques, A. Samani, E. El-Fiky, D. Patel, Z. Xing, and D. V. Plant, “Optimization of thermo-optic phase-shifter design and mitigation of thermal crosstalk on the soi platform,” *Optics express*, vol. 27, no. 8, pp. 10456–10471, 2019.
- [32] J. Parra, J. Hurtado, A. Griol, and P. Sanchis, “Ultra-low loss hybrid ito/si thermo-optic phase shifter with optimized power consumption,” *Optics Express*, vol. 28, no. 7, pp. 9393–9404, 2020.
- [33] H. Sun, Q. Qiao, Q. Guan, and G. Zhou, “Silicon photonic phase shifters and their applications: A review,” *Micromachines*, vol. 13, no. 9, p. 1509.
- [34] K. Van Acoleyen, J. Roels, P. Mechet, T. Claes, D. Van Thourhout, and R. Baets, “Ultracompact phase modulator based on a cascade of nems-operated slot waveguides fabricated in silicon-on-insulator,” *IEEE Photonics Journal*, vol. 4, no. 3, pp. 779–788, 2012.
- [35] P. Dong, S. Liao, D. Feng, H. Liang, D. Zheng, R. Shafiiha, C.-C. Kung, W. Qian, G. Li, X. Zheng, *et al.*, “Low v pp, ultralow-energy, compact, high-speed silicon electro-optic modulator,” *Optics express*, vol. 17, no. 25, pp. 22484–22490, 2009.
- [36] C. Wang, M. Zhang, X. Chen, M. Bertrand, A. Shams-Ansari, S. Chandrasekhar, P. Winzer, and M. Lončar, “Integrated lithium niobate electro-optic

- modulators operating at cmos-compatible voltages,” *Nature*, vol. 562, no. 7725, pp. 101–104, 2018.
- [37] M. Xu, M. He, H. Zhang, J. Jian, Y. Pan, X. Liu, L. Chen, X. Meng, H. Chen, Z. Li, *et al.*, “High-performance coherent optical modulators based on thin-film lithium niobate platform,” *Nature communications*, vol. 11, no. 1, p. 3911, 2020.
- [38] J. Carolan, C. Harrold, C. Sparrow, E. Martín-López, N. J. Russell, J. W. Silverstone, P. J. Shadbolt, N. Matsuda, M. Oguma, M. Itoh, *et al.*, “Universal linear optics,” *Science*, vol. 349, no. 6249, pp. 711–716, 2015.
- [39] B. J. Metcalf, J. B. Spring, P. C. Humphreys, N. Thomas-Peter, M. Barbieri, W. S. Kolthammer, X.-M. Jin, N. K. Langford, D. Kundys, J. C. Gates, *et al.*, “Quantum teleportation on a photonic chip,” *Nature photonics*, vol. 8, no. 10, pp. 770–774, 2014.
- [40] X. Qiang, X. Zhou, J. Wang, C. M. Wilkes, T. Loke, S. O’Gara, L. Kling, G. D. Marshall, R. Santagati, T. C. Ralph, *et al.*, “Large-scale silicon quantum photonics implementing arbitrary two-qubit processing,” *Nature photonics*, vol. 12, no. 9, pp. 534–539, 2018.
- [41] P. Lodahl, S. Mahmoodian, and S. Stobbe, “Interfacing single photons and single quantum dots with photonic nanostructures,” *Rev. Mod. Phys.*, vol. 87, pp. 347–400, May 2015.
- [42] F. T. Pedersen, Y. Wang, C. T. Olesen, S. Scholz, A. D. Wieck, A. Ludwig, M. C. LObl, R. J. Warburton, L. Midolo, R. Uppu, *et al.*, “Near transform-limited quantum dot linewidths in a broadband photonic crystal waveguide,”

- ACS Photonics*, vol. 7, no. 9, pp. 2343–2349, 2020.
- [43] H. Le Jeannic, A. Tiranov, J. Carolan, T. Ramos, Y. Wang, M. H. Appel, S. Scholz, A. D. Wieck, A. Ludwig, N. Rotenberg, *et al.*, “Dynamical photon–photon interaction mediated by a quantum emitter,” *Nature Physics*, vol. 18, no. 10, pp. 1191–1195, 2022.
- [44] M. Arcari, I. Söllner, A. Javadi, S. Lindskov Hansen, S. Mahmoodian, J. Liu, H. Thyrrstrup, E. H. Lee, J. D. Song, S. Stobbe, and P. Lodahl, “Near-unity coupling efficiency of a quantum emitter to a photonic crystal waveguide,” *Phys. Rev. Lett.*, vol. 113, p. 093603, Aug 2014.
- [45] P. Lodahl, S. Mahmoodian, S. Stobbe, A. Rauschenbeutel, P. Schneeweiss, J. Volz, H. Pichler, and P. Zoller, “Chiral quantum optics,” *Nature*, vol. 541, pp. 473–480, Jan. 2017.
- [46] C. Sayrin, C. Junge, R. Mitsch, B. Albrecht, D. O’Shea, P. Schneeweiss, J. Volz, and A. Rauschenbeutel, “Nanophotonic optical isolator controlled by the internal state of cold atoms,” *Physical Review X*, vol. 5, no. 4, p. 041036, 2015.
- [47] M. Scheucher, A. Hilico, E. Will, J. Volz, and A. Rauschenbeutel, “Quantum optical circulator controlled by a single chirally coupled atom,” *Science*, vol. 354, no. 6319, pp. 1577–1580, 2016.
- [48] I. Shomroni, S. Rosenblum, Y. Lovsky, O. Bechler, G. Guendelman, and B. Dayan, “All-optical routing of single photons by a one-atom switch controlled by a single photon,” *Science*, vol. 345, no. 6199, pp. 903–906, 2014.

- [49] W. R. Clements, P. C. Humphreys, B. J. Metcalf, W. S. Kolthammer, and I. A. Walmsley, “Optimal design for universal multiport interferometers,” *Optica*, vol. 3, pp. 1460–1465, Dec 2016.
- [50] C. P. Williams, “Quantum Gates,” in *Explorations in Quantum Computing*, pp. 51–122, London: Springer London, 2011. Series Title: Texts in Computer Science.
- [51] L. Xu, Y. Wang, A. Kumar, E. El-Fiky, D. Mao, H. Tamazin, M. Jacques, Z. Xing, M. G. Saber, and D. V. Plant, “Compact high-performance adiabatic 3-db coupler enabled by subwavelength grating slot in the silicon-on-insulator platform,” *Opt. Express*, vol. 26, pp. 29873–29885, Nov 2018.
- [52] J. C. Mikkelsen, W. D. Sacher, and J. K. S. Poon, “Dimensional variation tolerant silicon-on-insulator directional couplers,” *Opt. Express*, vol. 22, pp. 3145–3150, Feb 2014.
- [53] J. Cao, Z. Zhao, H. Sun, Y. Yang, Y. Deng, and P. Cao, “On Chip Polarization Beam Splitter Based on Inverse Design,” *Journal of Physics: Conference Series*, vol. 2464, p. 012019, Mar. 2023.
- [54] B. E. Saleh and M. C. Teich, *Fundamentals of photonics*. John Wiley & sons, 2019.
- [55] T. C. Ralph, N. K. Langford, T. B. Bell, and A. G. White, “Linear optical controlled-not gate in the coincidence basis,” *Phys. Rev. A*, vol. 65, p. 062324, Jun 2002.

- [56] N. Kiesel, C. Schmid, U. Weber, R. Ursin, and H. Weinfurter, “Linear Optics Controlled-Phase Gate Made Simple,” *Physical Review Letters*, vol. 95, p. 210505, Nov. 2005.
- [57] S. Aaronson and A. Arkhipov, “The computational complexity of linear optics,” 2010.
- [58] A. Ribeiro, A. Ruocco, L. Vanacker, and W. Bogaerts, “Demonstration of a 4x4-port universal linear circuit,” *Optica*, vol. 3, pp. 1348–1357, Dec 2016.
- [59] S. Bandyopadhyay, R. Hamerly, and D. Englund, “Hardware error correction for programmable photonics,” *Optica*, vol. 8, pp. 1247–1255, Oct 2021.
- [60] R. Hamerly, S. Bandyopadhyay, and D. Englund, “Accurate self-configuration of rectangular multiport interferometers,” *Phys. Rev. Appl.*, vol. 18, p. 024019, Aug 2022.
- [61] J. Mower, N. C. Harris, G. R. Steinbrecher, Y. Lahini, and D. Englund, “High-fidelity quantum state evolution in imperfect photonic integrated circuits,” *Phys. Rev. A*, vol. 92, p. 032322, Sep 2015.
- [62] J. Ewaniuk, J. Carolan, B. J. Shastri, and N. Rotenberg, “Imperfect Quantum Photonic Neural Networks,” *Advanced Quantum Technologies*, vol. 6, p. 2200125, Mar. 2023.
- [63] W. Bogaerts, D. Pérez, J. Capmany, D. A. B. Miller, J. Poon, D. Englund, F. Morichetti, and A. Melloni, “Programmable photonic circuits,” *Nature*, vol. 586, pp. 207–216, Oct. 2020.

- [64] F. Shokraneh, S. Geoffroy-gagnon, and O. Liboiron-Ladouceur, “The diamond mesh, a phase-error- and loss-tolerant field-programmable mzi-based optical processor for optical neural networks,” *Opt. Express*, vol. 28, pp. 23495–23508, Aug 2020.
- [65] F. Shokraneh, M. Sanadgol Nezami, and O. Liboiron-Ladouceur, “Theoretical and Experimental Analysis of a 44 Reconfigurable MZI-Based Linear Optical Processor,” *Journal of Lightwave Technology*, pp. 1–1, 2021.
- [66] R. Jozsa, “Fidelity for mixed quantum states,” *Journal of Modern Optics*, vol. 41, no. 12, pp. 2315–2323, 1994.
- [67] S. Pai, B. Bartlett, O. Solgaard, and D. A. B. Miller, “Matrix optimization on universal unitary photonic devices,” *Phys. Rev. Appl.*, vol. 11, p. 064044, Jun 2019.
- [68] R. Hamerly, S. Bandyopadhyay, and D. Englund, “Asymptotically fault-tolerant programmable photonics,” *Nature Communications*, vol. 13, p. 6831, Nov. 2022.
- [69] G. R. Steinbrecher, J. P. Olson, D. Englund, and J. Carolan, “Quantum optical neural networks,” *npj Quantum Information*, vol. 5, p. 60, Dec. 2019.
- [70] D. A. B. Miller, “Perfect optics with imperfect components,” *Optica*, vol. 2, pp. 747–750, Aug 2015.
- [71] C. M. Wilkes, X. Qiang, J. Wang, R. Santagati, S. Paesani, X. Zhou, D. A. B. Miller, G. D. Marshall, M. G. Thompson, and J. L. O’Brien, “60db high-extinction auto-configured mach–zehnder interferometer,” *Opt. Lett.*, vol. 41, pp. 5318–5321, Nov 2016.

- [72] M. J. Powell *et al.*, “The bobyqa algorithm for bound constrained optimization without derivatives,” *Cambridge NA Report NA2009/06*, University of Cambridge, Cambridge, vol. 26, 2009.
- [73] S. G. Johnson and J. Schueller, “Nlopt: Nonlinear optimization library,” *Astrophysics Source Code Library*, pp. ascl–2111, 2021.
- [74] P. Virtanen, R. Gommers, T. E. Oliphant, M. Haberland, T. Reddy, D. Cournapeau, E. Burovski, P. Peterson, W. Weckesser, J. Bright, *et al.*, “Scipy 1.0: fundamental algorithms for scientific computing in python,” *Nature methods*, vol. 17, no. 3, pp. 261–272, 2020.
- [75] C. Santori, D. Fattal, J. Vučković, G. S. Solomon, and Y. Yamamoto, “Indistinguishable photons from a single-photon device,” *Nature*, vol. 419, pp. 594–597, Oct. 2002.
- [76] D. Huber, M. Reindl, Y. Huo, H. Huang, J. S. Wildmann, O. G. Schmidt, A. Rastelli, and R. Trotta, “Highly indistinguishable and strongly entangled photons from symmetric GaAs quantum dots,” *Nature Communications*, vol. 8, p. 15506, May 2017.
- [77] J. Y. Marzin, J. M. Gérard, A. Izraël, D. Barrier, and G. Bastard, “Photoluminescence of single inas quantum dots obtained by self-organized growth on gaas,” *Phys. Rev. Lett.*, vol. 73, pp. 716–719, Aug 1994.
- [78] P. Senellart, G. Solomon, and A. White, “High-performance semiconductor quantum-dot single-photon sources,” *Nature nanotechnology*, vol. 12, no. 11, pp. 1026–1039, 2017.



- [79] Y. Deng, X. Lin, W. Fang, D. Di, L. Wang, R. H. Friend, X. Peng, and Y. Jin, “Deciphering exciton-generation processes in quantum-dot electroluminescence,” *Nature Communications*, vol. 11, p. 2309, May 2020.
- [80] A. S. Bracker, D. Gammon, and V. L. Korenev, “Fine structure and optical pumping of spins in individual semiconductor quantum dots,” *Semiconductor Science and Technology*, vol. 23, p. 114004, Nov. 2008.
- [81] X. Li, Q. Xu, and Z. Zhang, “Molecular Beam Epitaxy Growth of Quantum Wires and Quantum Dots,” *Nanomaterials*, vol. 13, p. 960, Mar. 2023.
- [82] I. N. Stranski and L. v. Krastanow, “Sitzungsberichte der akademie der wissenschaften in wien,” *Akad. Wiss. Lit. Mainz Math.-Natur. Kl. IIb*, vol. 146, p. 797, 1939.
- [83] W. Seifert, N. Carlsson, M. Miller, M.-E. Pistol, L. Samuelson, and L. R. Walenberg, “In-situ growth of quantum dot structures by the Stranski-Krastanow growth mode,” *Progress in Crystal Growth and Characterization of Materials*, vol. 33, pp. 423–471, Jan. 1996.
- [84] J. Skiba-Szymanska, R. M. Stevenson, C. Varnava, M. Felle, J. Huwer, T. Müller, A. J. Bennett, J. P. Lee, I. Farrer, A. B. Krysa, P. Spencer, L. E. Goff, D. A. Ritchie, J. Heffernan, and A. J. Shields, “Universal growth scheme for quantum dots with low fine-structure splitting at various emission wavelengths,” *Phys. Rev. Appl.*, vol. 8, p. 014013, Jul 2017.

- [85] P. J. Poole, K. Kaminska, P. Barrios, Z. Lu, and J. Liu, “Growth of InAs/InP-based quantum dots for 1.55 $\mu$ m laser applications,” *Journal of Crystal Growth*, vol. 311, no. 6, pp. 1482–1486, 2009.
- [86] R. S. R. Gajjela, A. L. Hendriks, J. O. Douglas, E. M. Sala, P. Steindl, P. Klenovský, P. A. J. Bagot, M. P. Moody, D. Bimberg, and P. M. Koenraad, “Structural and compositional analysis of (InGa)(AsSb)/GaAs/GaP Stran-ski–Krastanov quantum dots,” *Light: Science & Applications*, vol. 10, p. 125, June 2021.
- [87] A. Nemcsics, “Quantum dots prepared by droplet epitaxial method,” in *Quantum Dots* (V. N. Stavrou, ed.), ch. 5, Rijeka: IntechOpen, 2015.
- [88] S. Haffouz, K. D. Zeuner, D. Dalacu, P. J. Poole, J. Lapointe, D. Poitras, K. Mnaymneh, X. Wu, M. Couillard, M. Korkusinski, E. Schöll, K. D. Jöns, V. Zwiller, and R. L. Williams, “Bright Single InAsP Quantum Dots at Telecom Wavelengths in Position-Controlled InP Nanowires: The Role of the Photonic Waveguide,” *Nano Letters*, vol. 18, pp. 3047–3052, May 2018. Publisher: American Chemical Society.
- [89] C. Gerry and P. L. Knight, *Introductory quantum optics*. Cambridge university press, 2005.
- [90] A. Asenjo-Garcia, J. Hood, D. Chang, and H. Kimble, “Atom-light interactions in quasi-one-dimensional nanostructures: A green’s-function perspective,” *Physical Review A*, vol. 95, no. 3, p. 033818, 2017.

- [91] H. T. Dung, L. Knöll, and D.-G. Welsch, “Resonant dipole-dipole interaction in the presence of dispersing and absorbing surroundings,” *Physical Review A*, vol. 66, no. 6, p. 063810, 2002.
- [92] D. Dzsoţjan, J. Kästel, and M. Fleischhauer, “Dipole-dipole shift of quantum emitters coupled to surface plasmons of a nanowire,” *Physical Review B*, vol. 84, no. 7, p. 075419, 2011.
- [93] M. C. Rogge, B. Harke, C. Fricke, F. Hohls, M. Reinwald, W. Wegscheider, and R. J. Haug, “Coupling symmetry of quantum dot states,” *Phys. Rev. B*, vol. 72, p. 233402, Dec 2005.
- [94] A. Musia , P. Holewa, P. Wyborski, M. Syperek, A. Kors, J. P. Reithmaier, G. Sek, and M. Benyoucef, “High-purity triggered single-photon emission from symmetric single inas/inp quantum dots around the telecom c-band window,” *Advanced Quantum Technologies*, vol. 3, no. 2, p. 1900082, 2020.
- [95] H. Ollivier, I. Maillette de Buy Wenniger, S. Thomas, S. C. Wein, A. Harouri, G. Coppola, P. Hilaire, C. Millet, A. Lema tre, I. Sagnes, O. Krebs, L. Lanco, J. C. Lored, C. Ant n, N. Somaschi, and P. Senellart, “Reproducibility of high-performance quantum dot single-photon sources,” *ACS Photonics*, vol. 7, no. 4, pp. 1050–1059, 2020.
- [96] P. T rschmann, H. Le Jeannic, S. F. Simonsen, H. R. Haakh, S. G tzinger, V. Sandoghdar, P. Lodahl, and N. Rotenberg, “Coherent nonlinear optics of quantum emitters in nanophotonic waveguides,” *Nanophotonics*, vol. 8, no. 10, pp. 1641–1657, 2019.

- 
- [97] I. Söllner, S. Mahmoodian, S. L. Hansen, L. Midolo, A. Javadi, G. Kiršanskė, T. Pregolato, H. El-Ella, E. H. Lee, J. D. Song, S. Stobbe, and P. Lodahl, “Deterministic photon–emitter coupling in chiral photonic circuits,” *Nature Nanotechnology*, vol. 10, pp. 775–778, Sept. 2015.
- [98] R. J. Warburton, “Single spins in self-assembled quantum dots,” *Nature materials*, vol. 12, no. 6, pp. 483–493, 2013.
- [99] N. V. Hauff, H. Le Jeannic, P. Lodahl, S. Hughes, and N. Rotenberg, “Chiral quantum optics in broken-symmetry and topological photonic crystal waveguides,” *Phys. Rev. Res.*, vol. 4, p. 023082, Apr 2022.
- [100] S. Mahmoodian, K. Prindal-Nielsen, I. Söllner, S. Stobbe, and P. Lodahl, “Engineering chiral light–matter interaction in photonic crystal waveguides with slow light,” *Opt. Mater. Express*, vol. 7, pp. 43–51, Jan 2017.
- [101] D. Martin-Cano, H. R. Haakh, and N. Rotenberg, “Chiral Emission into Nanophotonic Resonators,” *ACS Photonics*, vol. 6, pp. 961–966, Apr. 2019. Publisher: American Chemical Society.
- [102] I. J. Luxmoore, N. A. Wasley, A. J. Ramsay, A. C. T. Thijssen, R. Oulton, M. Hugues, S. Kasture, V. G. Achanta, A. M. Fox, and M. S. Skolnick, “Interfacing spins in an ingaas quantum dot to a semiconductor waveguide circuit using emitted photons,” *Phys. Rev. Lett.*, vol. 110, p. 037402, Jan 2013.
- [103] R. Mitsch, C. Sayrin, B. Albrecht, P. Schneeweiss, and A. Rauschenbeutel, “Quantum state-controlled directional spontaneous emission of photons into a nanophotonic waveguide,” *Nature Communications*, vol. 5, p. 5713, Dec. 2014.

- [104] R. J. Coles, D. M. Price, J. E. Dixon, B. Royall, E. Clarke, P. Kok, M. S. Skolnick, A. M. Fox, and M. N. Makhonin, “Chirality of nanophotonic waveguide with embedded quantum emitter for unidirectional spin transfer,” *Nature Communications*, vol. 7, p. 11183, Mar. 2016.
- [105] H. Le Jeannic, A. Tiranov, J. Carolan, T. Ramos, Y. Wang, M. H. Appel, S. Scholz, A. D. Wieck, A. Ludwig, N. Rotenberg, L. Midolo, J. J. García-Ripoll, A. S. Sørensen, and P. Lodahl, “Dynamical photon–photon interaction mediated by a quantum emitter,” *Nature Physics*, vol. 18, pp. 1191–1195, Oct. 2022.
- [106] A. V. Kuhlmann, J. Houel, A. Ludwig, L. Greuter, D. Reuter, A. D. Wieck, M. Poggio, and R. J. Warburton, “Charge noise and spin noise in a semiconductor quantum device,” *Nature Physics*, vol. 9, no. 9, pp. 570–575, 2013.
- [107] A. V. Kuhlmann, J. H. Preetel, J. Houel, A. Ludwig, D. Reuter, A. D. Wieck, and R. J. Warburton, “Transform-limited single photons from a single quantum dot,” *Nature communications*, vol. 6, no. 1, p. 8204, 2015.
- [108] M. J. Mangnus, J. W. de Wit, S. J. Vonk, J. J. Geuchies, W. Albrecht, S. Bals, A. J. Houtepen, and F. T. Rabouw, “High-throughput characterization of single-quantum-dot emission spectra and spectral diffusion by multiparticle spectroscopy,” *ACS Photonics*, 2023.
- [109] H. Thyrestrup, G. Kirsanske, H. Le Jeannic, T. Pregnolato, L. Zhai, L. Raahauge, L. Midolo, N. Rotenberg, A. Javadi, R. Schott, *et al.*, “Quantum optics with near-lifetime-limited quantum-dot transitions in a nanophotonic waveguide,” *Nano letters*, vol. 18, no. 3, pp. 1801–1806, 2018.

- [110] A. Tiranov, V. Angelopoulou, C. J. van Diepen, B. Schrintski, O. A. D. Sandberg, Y. Wang, L. Midolo, S. Scholz, A. D. Wieck, A. Ludwig, *et al.*, “Collective super- and subradiant dynamics between distant optical quantum emitters,” *Science*, vol. 379, no. 6630, pp. 389–393, 2023.
- [111] H. Thyrestrup, G. Kiršanskė, H. Le Jeannic, T. Pregnolato, L. Zhai, L. Raahauge, L. Midolo, N. Rotenberg, A. Javadi, R. Schott, A. D. Wieck, A. Ludwig, M. C. Löbl, I. Söllner, R. J. Warburton, and P. Lodahl, “Quantum Optics with Near-Lifetime-Limited Quantum-Dot Transitions in a Nanophotonic Waveguide,” *Nano Letters*, vol. 18, pp. 1801–1806, Mar. 2018. Publisher: American Chemical Society.
- [112] W. Langbein, P. Borri, U. Woggon, V. Stavarache, D. Reuter, and A. Wieck, “Radiatively limited dephasing in inas quantum dots,” *Physical Review B*, vol. 70, no. 3, p. 033301, 2004.
- [113] C. Matthiesen, A. N. Vamivakas, and M. Atatüre, “Subnatural linewidth single photons from a quantum dot,” *Physical Review Letters*, vol. 108, no. 9, p. 093602, 2012.
- [114] H.-S. Nguyen, G. Sallen, C. Voisin, P. Roussignol, C. Diederichs, and G. Cassabois, “Ultra-coherent single photon source,” *Applied Physics Letters*, vol. 99, no. 26, 2011.
- [115] K. Życzkowski and M. Kus, “Random unitary matrices,” *Journal of Physics A: Mathematical and General*, vol. 27, no. 12, p. 4235, 1994.

- [116] M. Ozols, “How to generate a random unitary matrix,” *unpublished essay on <http://home.lu.lv/sd20008>*, 2009.
- [117] M. Lundberg and L. Svensson, “The haar measure and the generation of random unitary matrices,” in *Processing Workshop Proceedings, 2004 Sensor Array and Multichannel Signal*, pp. 114–118, 2004.
- [118] R. Wille, R. Van Meter, and Y. Naveh, “Ibm’s qiskit tool chain: Working with and developing for real quantum computers,” in *2019 Design, Automation & Test in Europe Conference & Exhibition (DATE)*, pp. 1234–1240, IEEE, 2019.
- [119] P. Meystre and M. Sargent, *Elements of quantum optics*. Springer Berlin Heidelberg, 2007.

## Appendix A

### Additional Mathematical Derivation for Chapter 3

#### A.1 Interaction Picture Evolution Operator Derivation

Here we cover the derivation of the evolution operators for the interaction picture as used in Section 3.2. We begin with the emitter evolution operator as,

$$\begin{aligned}
 \hat{U}_A &= \exp\left[-\frac{i}{\hbar}\hat{H}_{0_A}t\right] \\
 &= \exp\left[-\frac{i}{\hbar}(\hbar\omega_A\hat{\sigma}_{eg}\hat{\sigma}_{ge})t\right] \\
 &= \exp(-i\omega_At|e\rangle\langle e|).
 \end{aligned} \tag{A.1}$$

Then through a Taylor expansion,

$$\exp(-i\omega_At|e\rangle\langle e|) = 1 + -i\omega_At|e\rangle\langle e| + \frac{(-i\omega_At|e\rangle\langle e|)^2}{2!} + \dots, \tag{A.2}$$

which can be simplified if we note that,

$$\begin{aligned}
 (|e\rangle\langle e|)^2 &= |e\rangle\langle e|e\rangle\langle e| = |e\rangle\langle e| \\
 (|e\rangle\langle e|)^3 &= |e\rangle\langle e|e\rangle\langle e|e\rangle\langle e| = |e\rangle\langle e|,
 \end{aligned} \tag{A.3}$$



which holds for all powers of this term. We can now insert closure, which in this case is,

$$\begin{aligned}\hat{I} &= \sum_i |i\rangle\langle i| \\ &= |g\rangle\langle g| + |e\rangle\langle e|.\end{aligned}\tag{A.4}$$

Taking all this together gives the atomic evolution operator as,

$$\begin{aligned}\hat{U}_A &= \exp(-i\omega_A t |e\rangle\langle e|) \\ &= |g\rangle\langle g| + |e\rangle\langle e| - i\omega_A t |e\rangle\langle e|(|g\rangle\langle g| + |e\rangle\langle e|) + \frac{(-i\omega_A t)^2 |e\rangle\langle e|(|g\rangle\langle g| + |e\rangle\langle e|)}{2!} + \dots \\ &= |g\rangle\langle g| + |e\rangle\langle e| - i\omega_A t |e\rangle\langle e| + \frac{(-i\omega_A t)^2}{2!} |e\rangle\langle e| + \dots \\ &= |g\rangle\langle g| + \exp(-i\omega_A t) |e\rangle\langle e|.\end{aligned}\tag{A.5}$$

Similarly, we can determine the light field evolution operator as,

$$\begin{aligned}\hat{U}_P &= \exp\left[-\frac{i}{\hbar} \hat{H}_{0_P} t\right] \\ &= \exp\left[-\frac{i}{\hbar} (\hbar\omega_P \hat{f}^\dagger \hat{f}) t\right] \\ &= \exp\left[-\frac{i}{\hbar} \hbar\omega_P t \sum_{n'} \sqrt{n'+1} |n'+1\rangle\langle n'| \sum_n \sqrt{n} |n-1\rangle\langle n|\right].\end{aligned}\tag{A.6}$$

Note that all terms are 0 unless  $n' = n - 1$ , so we can set this equation to be true, resulting in,

$$\begin{aligned}\hat{U}_P &= \exp\left[-\frac{i}{\hbar}\hbar\omega_P t \sum_{n=1}^{\infty} \sqrt{n}|n\rangle\langle n-1|\sqrt{n}|n-1\rangle\langle n|\right] \\ &= \exp\left[-i\omega_P t \sum_n n|n\rangle\langle n|\right].\end{aligned}\tag{A.7}$$

## A.2 Current Density Operator Derivation

In this section, we derive the current density operator for the light field in a waveguide to determine the electric field equation as shown in Equation 3.19. We start with the fluctuation-dissipation theorem,

$$\langle 0|S[\hat{P}_N(r, \omega)\hat{P}_N^\dagger(r', \omega')]|0\rangle = \frac{\hbar}{2\pi}\epsilon_0 \text{Im}\chi(r, \omega)\delta(r - r')\delta(\omega - \omega'),\tag{A.8}$$

where we have

$$S[\hat{a}\hat{b}^\dagger] = \frac{1}{2}(\hat{a}\hat{b}^\dagger + \hat{b}^\dagger\hat{a}),\tag{A.9}$$

and where  $\hat{P}_N(r, \omega)$  is the polarization noise operator, which we will assume takes the form of,

$$\hat{P}_N(r, \omega) = iC\hat{f}(r, \omega)\tag{A.10}$$

where C is a real constant. So, for the  $\hat{E}^+$  operator, we can find the C constant using Equation A.8 starting with the LHS,

$$\begin{aligned}
LHS &= \langle 0 | S [\hat{P}_N(r, \omega) \hat{P}_N^\dagger(r', \omega')] | 0 \rangle \\
&= \langle 0 | \frac{1}{2} [\hat{P}_N(r, \omega) \hat{P}_N^\dagger(r', \omega') + \hat{P}_N^\dagger(r', \omega') \hat{P}_N(r, \omega)] | 0 \rangle \\
&= \langle 0 | \frac{1}{2} [iC \hat{f}(r, \omega) (-iC \hat{f}^\dagger(r', \omega')) + (-iC \hat{f}^\dagger(r', \omega')) iC \hat{f}(r, \omega)] | 0 \rangle \\
&= \langle 0 | \frac{1}{2} [C^2 \hat{f}(r, \omega) \hat{f}^\dagger(r', \omega') + C^2 \hat{f}^\dagger(r', \omega') \hat{f}(r, \omega)] | 0 \rangle.
\end{aligned} \tag{A.11}$$

We know how these number states will apply to the bosonic operators,

$$\begin{aligned}
\hat{f}(r, \omega) | 0 \rangle &= \sum_n \sqrt{n} | n-1 \rangle \langle n | 0 \rangle \\
&= 0,
\end{aligned} \tag{A.12}$$

$$\begin{aligned}
\hat{f}^\dagger(r', \omega') | 0 \rangle &= \sum_n \sqrt{n+1} | n+1 \rangle \langle n | 0 \rangle \\
&= | 1 \rangle,
\end{aligned} \tag{A.13}$$

$$\begin{aligned}
\hat{f}(r, \omega) | 1 \rangle &= \sum_n \sqrt{n} | n-1 \rangle \langle n | 1 \rangle \\
&= | 0 \rangle.
\end{aligned} \tag{A.14}$$

Thus, returning to the LHS we get,

$$\begin{aligned}
LHS &= \langle 0 | \frac{1}{2} [C^2 \hat{f}(r, \omega) \hat{f}^\dagger(r', \omega') + C^2 \hat{f}^\dagger(r', \omega') \hat{f}(r, \omega)] | 0 \rangle \\
&= \langle 0 | \frac{1}{2} [C^2 | 0 \rangle + 0] \\
&= \frac{1}{2} C^2.
\end{aligned} \tag{A.15}$$

So Equation A.8 becomes,

$$\begin{aligned}
 \frac{1}{2}C^2 &= \frac{\hbar}{2\pi}\epsilon_0 \text{Im}\chi(r, \omega)\delta(r - r')\delta(\omega - \omega') \\
 C^2 &= \frac{\hbar}{\pi}\epsilon_0 \text{Im}\chi(r, \omega) \\
 C &= \sqrt{\frac{\hbar}{\pi}\epsilon_0 \text{Im}\chi(r, \omega)} \\
 C &= \sqrt{\frac{\hbar}{\pi}\epsilon_0 \epsilon_I(r, \omega)}
 \end{aligned} \tag{A.16}$$

where we have used the fact that  $\text{Im}\chi(r, \omega) = \epsilon_I(r, \omega)$ . So we can now determine the noise polarization operator from Equation A.10 as,

$$\hat{P}_{NL}(r, \omega) = i\sqrt{\frac{\hbar}{\pi}\epsilon_0 \epsilon_I(r, \omega)}\hat{f}(r, \omega). \tag{A.17}$$

We know the relation between the noise polarization operator and the noise current is,

$$\begin{aligned}
 \hat{j}_N(r, \omega) &= -i\omega\hat{P}_N(r, \omega) \\
 \hat{j}_N(r, \omega) &= \omega\sqrt{\frac{\hbar}{\pi}\epsilon_0 \epsilon_I(r, \omega)}\hat{f}(r, \omega).
 \end{aligned} \tag{A.18}$$

Now, equipped with the current density operator we can write the electric field operator with the volume integral equation (Equation 3.18), as shown in Equation 3.19.

### **A.3 Open System Emitter Dynamics and the Density Matrix**

In this section we derive the reduced density matrix and system dynamics for the light-matter interaction in an open system, which we use in Sections 3.3 and 3.4. From the Jaynes-Cummings Hamiltonian, if we assume that all photons have a frequency  $\omega_P$ ,

we can move into the frame that rotates with  $\omega_P$  and rewrite the Hamiltonian as,

$$\hat{H}_S = -\hbar\Delta_P\hat{\sigma}_{eg}\hat{\sigma}_{ge} + \hbar\omega_P\hat{f}^\dagger\hat{f} - \hbar\Omega_P(\hat{\sigma}_{eg} + \hat{\sigma}_{ge}), \quad (\text{A.19})$$

where  $\Delta_P = \omega_P - \omega_A$  is the detuning between the quantum dot resonance frequency and the light field.  $\Omega_P$  is the Rabi frequency of the light, defined by,

$$\Omega_P = d^* \cdot \frac{E^+}{\hbar}, \quad (\text{A.20})$$

which quantifies the strength of the light-matter interaction. Note that this is a semi-classical definition of the Rabi frequency, and it is redefined properly as the quantum operator in Section 3.2. We can then write the emitter's reduced density matrix as,

$$\rho_A = \begin{bmatrix} \rho_{gg} & \rho_{ge} \\ \rho_{eg} & \rho_{ee} \end{bmatrix}, \quad (\text{A.21})$$

where the diagonal terms describe the population of the ground and excited states, and the off-diagonal terms depict the quantum coherences of the system between the energy levels. By tracing over the density matrix, we can calculate expectation values for the atomic operators as,

$$\langle \hat{\sigma}_{i,j} \rangle = \text{tr}(\rho_A \hat{\sigma}_{i,j}) = \rho_{j,i} = \rho_{i,j}^*, \quad (\text{A.22})$$

which is used in the derivation in Sections 3.3 and 3.4. Since the emitter is not in a closed system and interacts with the environment, it will experience decoherence from environmental interactions, which can be modeled by assuming the emitter is

coupled to a reservoir. This then allows you to model the dynamics of the emitter using the Lindblad master equation [119] as follows,

$$\dot{\hat{\rho}} = \frac{-i}{\hbar} [\hat{H}_S, \hat{\rho}] + \sum_{i,j} \frac{\Gamma_{ij}}{2} (2\hat{\sigma}_{ji}\hat{\rho}\hat{\sigma}_{ij} - \hat{\sigma}_{ii}\hat{\rho} - \hat{\rho}\hat{\sigma}_{ii}), \quad (\text{A.23})$$

where  $\Gamma_{eg} = \Gamma$  is the rate of spontaneous emission of the emitter, and  $\Gamma_{gg} = \Gamma_{ee} = \Gamma_{dp}$  is the rate of pure dephasing in the system. Using this master equation, we can derive the equations of motion,

$$\begin{aligned} \dot{\rho}_{gg} &= i\Omega_P(\rho_{eg} - \rho_{ge}) + \Gamma\rho_{ee} \\ \dot{\rho}_{ge} &= -(\Gamma_2 + i\Delta_P)\rho_{ge} + i\Omega_P(\rho_{ee} - \rho_{gg}) \\ \dot{\rho}_{eg} &= -(\Gamma_2 - i\Delta_P)\rho_{eg} - i\Omega_P(\rho_{ee} - \rho_{gg}) \\ \dot{\rho}_{ee} &= -i\Omega_P(\rho_{eg} - \rho_{ge}) - \Gamma\rho_{ee}, \end{aligned} \quad (\text{A.24})$$

where we have defined,

$$\Gamma_2 = \frac{\Gamma}{2} + \Gamma_{dp}, \quad (\text{A.25})$$

to simplify the equations. To determine the solutions to these equations of motion, we look at the steady state behavior of the system where  $\dot{\rho}_A = 0$ . From this we get the populations as,

$$\rho_{ee} = \frac{2\Gamma_2\Omega_P^2}{\Gamma(\Gamma_2^2 + \Delta_P^2 + 4(\Gamma_2/\Gamma)\Omega_P^2)} \quad (\text{A.26})$$

$$\rho_{eg} = \frac{\Omega_P(i\Gamma_2 - \Delta_p)}{\Gamma_2^2 + \Delta_p^2 + 4(\Gamma_2/\Gamma)\Omega_P^2} \quad (\text{A.27})$$

$$\rho_{ge} = \frac{-\Omega_P(i\Gamma_2 + \Delta_p)}{\Gamma_2^2 + \Delta_p^2 + 4(\Gamma_2/\Gamma)\Omega_P^2} \quad (\text{A.28})$$

$$\rho_{gg} = 1 - \frac{2\Gamma_2\Omega_P^2}{\Gamma(\Gamma_2^2 + \Delta_p^2 + 4(\Gamma_2/\Gamma)\Omega_P^2)} \quad (\text{A.29})$$

#### A.4 Commutator Derivation for Heisenberg Equation of Motion

In this section, we cover the commutator solutions to the Heisenberg equation of motion as shown in Equation 3.25 that is used in Section 3.2. We begin by knowing, due to the operators being in different Hilbert spaces that,

$$\left[ \hbar\omega_A \hat{\sigma}_{eg} \hat{\sigma}_{ge}, \hat{f} \right] = 0. \quad (\text{A.30})$$

By definition, the bosonic operators have the following commutator relations,

$$\begin{aligned} \left[ \hat{f}, \hat{f} \right] &= 0 \\ \left[ \hat{f}^\dagger(r', \omega), \hat{f}(r, \omega_P) \right] &= -\delta(r - r')\delta(\omega_P - \omega) \\ &= -1, \end{aligned} \quad (\text{A.31})$$

where the light field is at frequency  $\omega_P$  and we are at some point  $r$  in the waveguide. Additionally, since the electric field operators depend on the bosonic operators, we can determine that

$$[\hat{E}^+, \hat{f}] = 0. \quad (\text{A.32})$$

This leaves only two terms to compute in the equation of motion. Beginning with the commutator,

$$\left[ \hbar\omega_P \hat{f}^\dagger \hat{f}, \hat{f} \right] = \left[ \hbar\omega_P \hat{f}^\dagger, \hat{f} \right] \hat{f} = -\hbar\omega_P \hat{f}. \quad (\text{A.33})$$

Leaving only the following commutator to compute,

$$\left[ d \cdot \hat{E}^- \hat{\sigma}_{ge}, \hat{f}(r, \omega_P) \right] = \left[ d \cdot \hat{E}^-, \hat{f}(r, \omega_P) \right] \hat{\sigma}_{ge}. \quad (\text{A.34})$$

To solve this, we assume the TLS is at some location  $r_A$ , and we can write,

$$d = d(r) \delta(r - r_A), \quad (\text{A.35})$$

then allowing us to describe the dipole-field interaction as,

$$d \cdot \hat{E}^- = d(r_A) \cdot \hat{E}^-(r_A), \quad (\text{A.36})$$

which allows us to solve the commutator by substituting in the known electric field operator from Equation 3.20,



$$\begin{aligned}
\left[ d \cdot \hat{E}^-, \hat{f}(r, \omega_P) \right] \hat{\sigma}_{ge} &= [d(r_A) \cdot \\
&\quad - i\omega^2 \mu_0 \sqrt{\frac{\hbar}{\pi} \epsilon_0} \int dr' \sqrt{\epsilon_I(r', \omega)} G^{\leftrightarrow*}(r_A, r', \omega) \hat{f}^\dagger(r', \omega), \hat{f}(r, \omega_P)] \hat{\sigma}_{ge} \\
&= d(r_A) \cdot -i\omega^2 \mu_0 \sqrt{\frac{\hbar}{\pi} \epsilon_0} \int dr' \sqrt{\epsilon_I(r', \omega)} G^{\leftrightarrow*}(r_A, r', \omega) \\
&\quad \left[ \hat{f}^\dagger(r', \omega), \hat{f}(r, \omega_P) \right] \hat{\sigma}_{ge} \\
&= d(r_A) \cdot -i\omega^2 \mu_0 \sqrt{\frac{\hbar}{\pi} \epsilon_0} \int dr' \sqrt{\epsilon_I(r', \omega)} G^{\leftrightarrow*}(r_A, r', \omega) \\
&\quad \delta(r - r') \delta(\omega - \omega_P) \hat{\sigma}_{ge} \\
&= i\omega_P^2 \mu_0 \sqrt{\frac{\hbar}{\pi} \epsilon_0} d(r_A) \cdot \int dr' \delta(r' - r) \sqrt{\epsilon_I(r', \omega_P)} G^{\leftrightarrow*}(r_A, r', \omega_P) \hat{\sigma}_{ge} \\
&= i\omega_P^2 \mu_0 \sqrt{\frac{\hbar}{\pi} \epsilon_0} d(r_A) \sqrt{\epsilon_I(r, \omega_P)} G^{\leftrightarrow*}(r_A, r, \omega_P) \hat{\sigma}_{ge}.
\end{aligned} \tag{A.37}$$

With the solutions to these commutators, we are able to determine the equation of motion as shown in Equation 3.26.

## Appendix B

### Supplemental Data and Analysis for Chapter 4

#### B.1 Infidelity Beta Distributions

To ensure accurate results, every matrix infidelity data point in the figures in Chapter 4 comes from 100 Haar random unitary matrices. However, these infidelities are not averaged across all 100, as there are often outliers that do not perform as well, so the accurate infidelity for the distribution is often below the average infidelity. To account for this, the infidelity distributions are instead fit to a beta distribution which follows the probability density function,

$$f(x) = \frac{(x-a)^{p-1}(b-x)^{q-1}}{B(p,q)(b-a)^{p+q-1}}, \quad (\text{B.1})$$

where  $a$  and  $b$  are the lower and upper bounds on  $x$ ,  $p$  and  $q$  are shape parameters where  $p, q > 0$  and  $B(p, q)$  is the beta function that follows the equation,

$$B(\alpha, \beta) = \int_0^1 t^{\alpha-1}(1-t)^{\beta-1} dt. \quad (\text{B.2})$$

The curve fit is performed in Python using the Scipy library’s curve fit function, using Scipy’s stats library for the beta distribution’s probability density function. Figure B.1 shows an example infidelity histogram for an  $N = 4$  circuit with an arbitrary choice of 2.3% beam splitter error, simulated as described in Section 4.1. On this figure, we plot a beta fit, normal distribution fit, and the mean of the data to determine the best model to match the data.

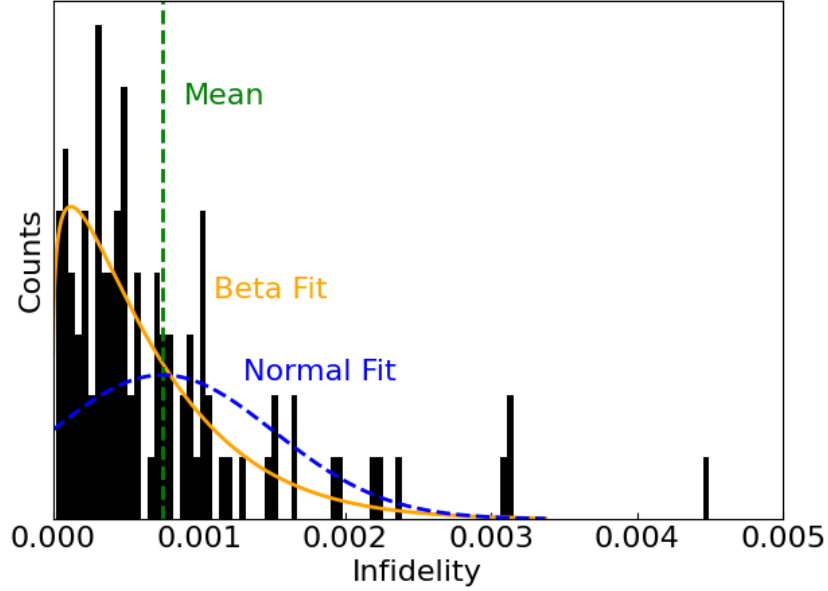


Figure B.1: Matrix infidelity histogram over 100 Haar random  $N = 4$  circuits for a beam splitter error of 2.3%, with no other imperfections. Here we show the mean of the data (green), a beta fit (orange), and a normal fit (blue), to the data.

In Figure B.1, we see that the mean and normal fit both result in average infidelity that is higher than the majority of the data. Conversely, the beta fit accounts for the asymmetry of the data, and more accurately represents the data. Thus, for matrix infidelity simulations in this work, we always use the mean of a beta fit to represent

the data.

## B.2 Optimization Convergence and Tolerance

While the Monte-Carlo simulation method is accurate, as described in Section 4.3, at times it can limit optimization convergence. The optimization converges when the change in cost between optimization steps is below a set tolerance. For our case, this tolerance is set to  $10^{-9}$ , and without spectral diffusion and dephasing, will always converge to an optimum. However, with spectral diffusion and dephasing, the fluctuations in cost can become too large to ever reach the tolerance, and the optimizer will fail to converge. To address this, if the optimizer fails twice on a unitary optimization, it will increase the tolerance by an order of magnitude, and repeat this until it either converges or reaches a tolerance of 0.01. At this point if it does not converge after two more trials, the phases from the imperfect case will be taken instead.

This never occurred in our imperfection ranges for  $N = 4$  or larger circuits, as they have enough phase shifters to adjust for the fluctuations, and are still able to converge at the  $10^{-9}$  tolerance. However, for  $N = 2, 3$  circuits, this occurs often and hinders the ability to optimize them, at times causing odd fluctuations in the data.

## B.3 Supplemental Monte-Carlo Testing Data

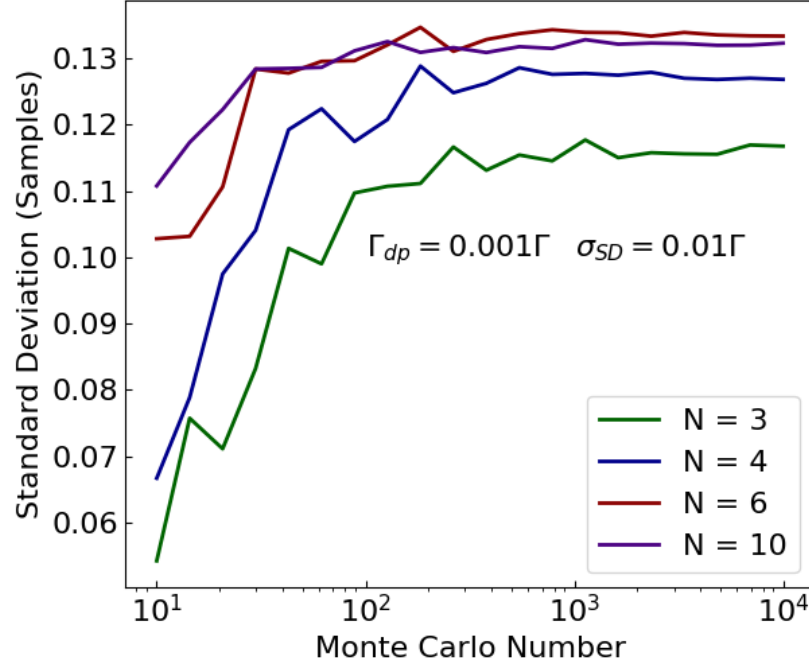


Figure B.2: Standard deviation between Monte-Carlo samples for  $N = 3$  (green),  $N = 4$  (blue),  $N = 6$  (red),  $N = 10$  (purple), circuit infidelities with  $\Gamma_{dp} = 0.001\Gamma$  and  $\sigma_{SD} = 0.01\Gamma$ . This is shown across 10 to 10000 Monte-Carlo Samples per unitary. Each point is averaged over 100 Haar random unitaries.

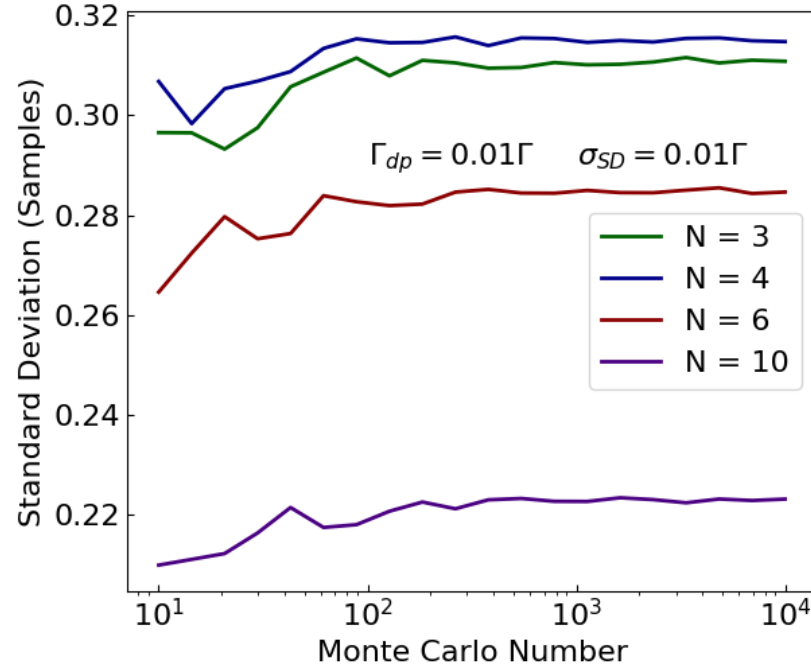


Figure B.3: Standard deviation between Monte-Carlo samples for  $N = 3$  (green),  $N = 4$  (blue),  $N = 6$  (red),  $N = 10$  (purple), circuit infidelities with  $\Gamma_{dp} = 0.01\Gamma$  and  $\sigma_{SD} = 0.01\Gamma$ . This is shown across 10 to 10000 Monte-Carlo Samples per unitary. Each point is averaged over 100 Haar random unitaries.

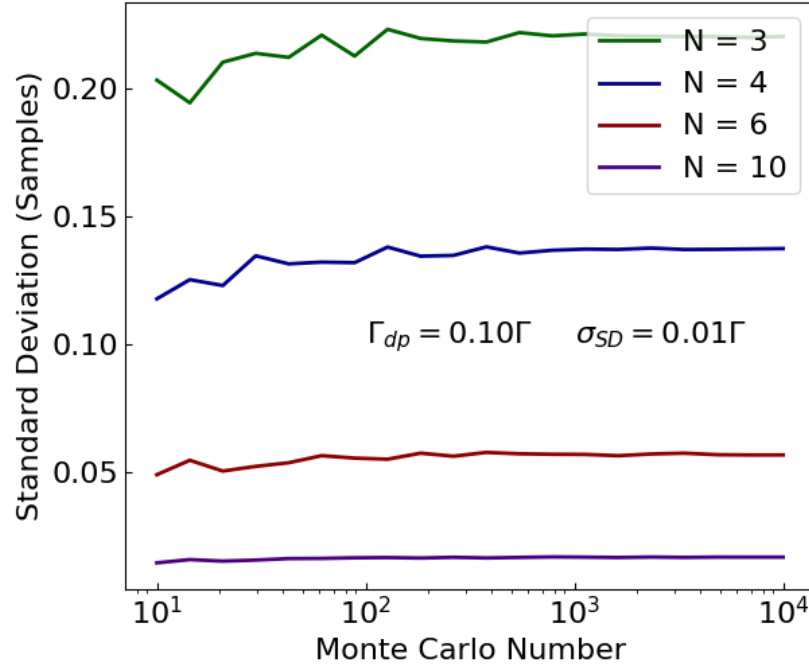


Figure B.4: Standard deviation between Monte-Carlo samples for  $N = 3$  (green),  $N = 4$  (blue),  $N = 6$  (red),  $N = 10$  (purple), circuit infidelities with  $\Gamma_{dp} = 0.10\Gamma$  and  $\sigma_{SD} = 0.01\Gamma$ . This is shown across 10 to 10000 Monte-Carlo Samples per unitary. Each point is averaged over 100 Haar random unitaries.

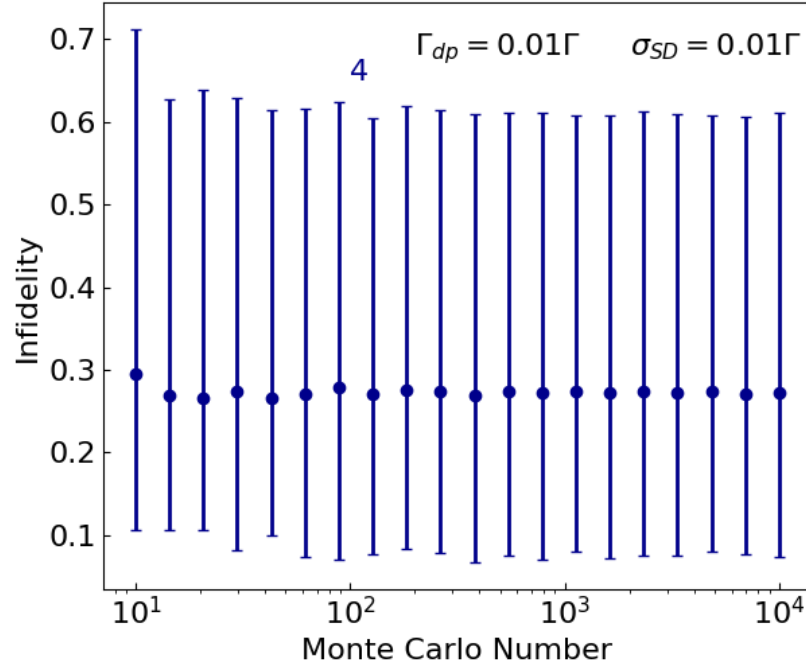


Figure B.5: Imperfect circuit infidelity results spanning 10 to 10000 Monte-Carlo simulations for  $N = 4$  circuits. Each point is taken from the beta fit to 100 Haar random unitaries, and the error bars are the standard deviations of the fit. This simulation was performed with  $\Gamma_{dp} = 0.01\Gamma$  and with spectral diffusion of  $\sigma_{SD} = 0.01\Gamma$ .



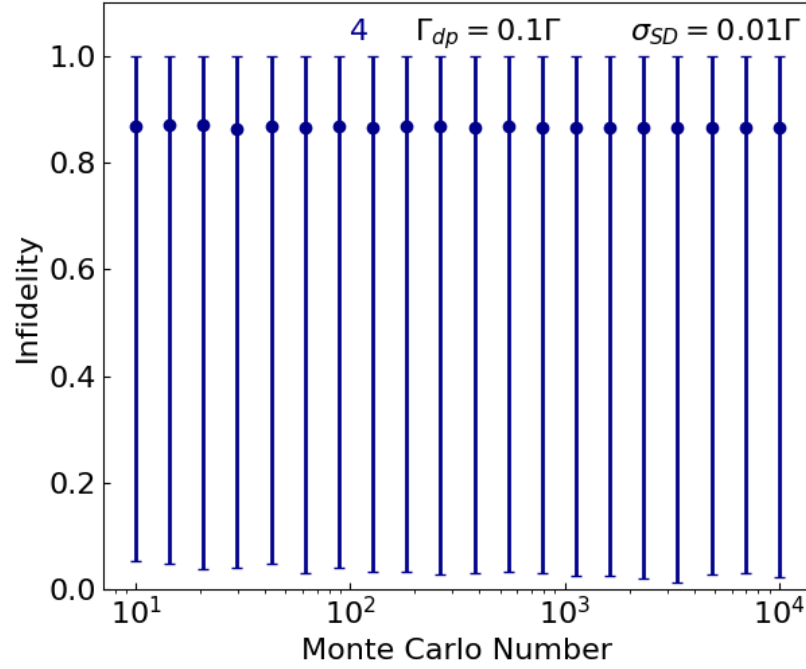


Figure B.6: Imperfect circuit infidelity results spanning 10 to 10000 Monte-Carlo simulations for  $N = 4$  circuits. Each point is taken from the beta fit to 100 Haar random unitaries, and the error bars are the standard deviations of the fit. This simulation was performed with  $\Gamma_{dp} = 0.10\Gamma$  and with spectral diffusion of  $\sigma_{SD} = 0.01\Gamma$ .

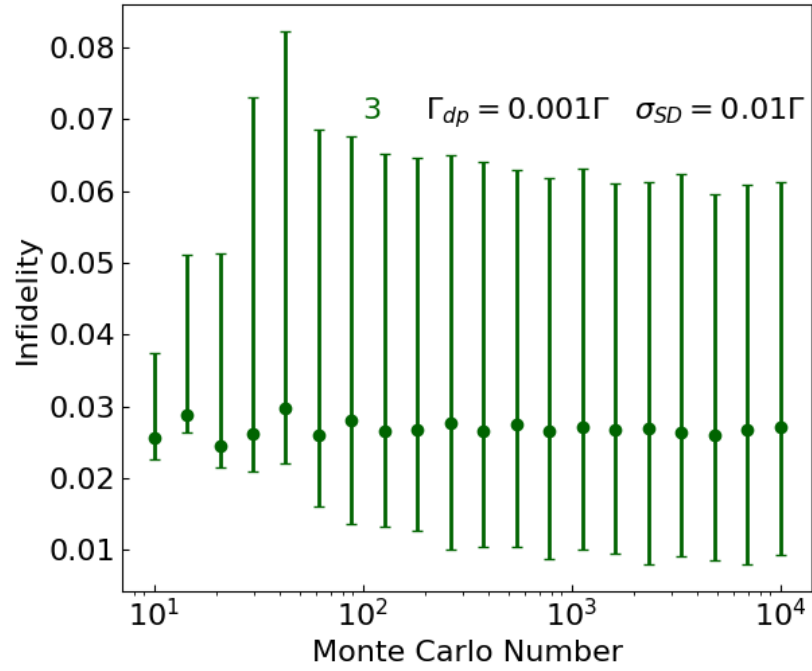


Figure B.7: Imperfect circuit infidelity results spanning 10 to 10000 Monte-Carlo simulations for  $N = 3$  circuits. Each point is taken from the beta fit to 100 Haar random unitaries, and the error bars are the standard deviations of the fit. This simulation was performed with  $\Gamma_{dp} = 0.001\Gamma$  and with spectral diffusion of  $\sigma_{SD} = 0.01\Gamma$ .

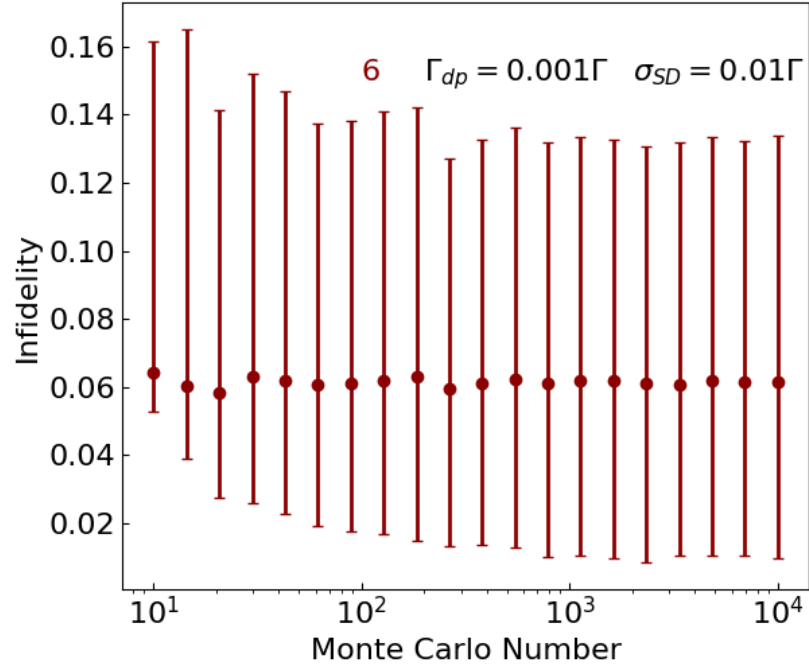


Figure B.8: Imperfect circuit infidelity results spanning 10 to 10000 Monte-Carlo simulations for  $N = 6$  circuits. Each point is taken from the beta fit to 100 Haar random unitaries, and the error bars are the standard deviations of the fit. This simulation was performed with  $\Gamma_{dp} = 0.001\Gamma$  and with spectral diffusion of  $\sigma_{SD} = 0.01\Gamma$ .

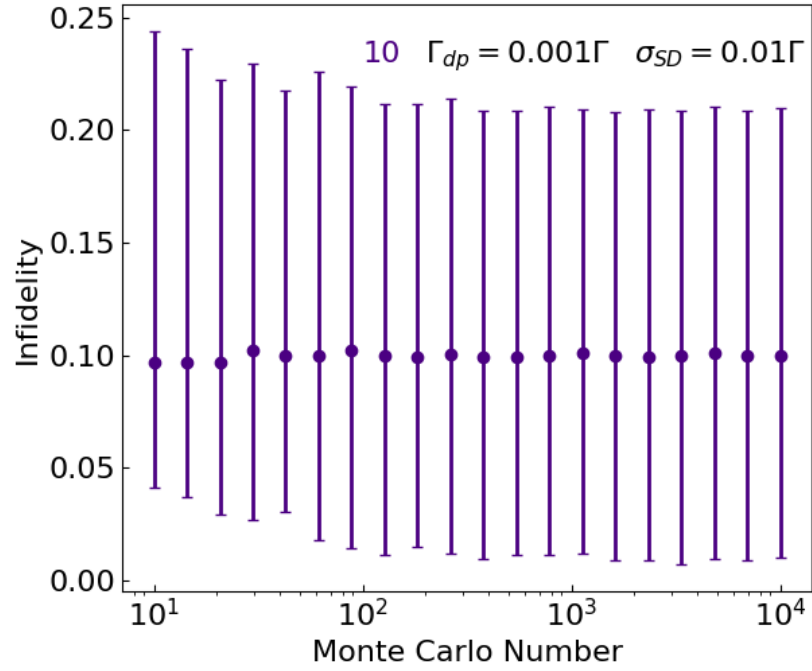


Figure B.9: Imperfect circuit infidelity results spanning 10 to 10000 Monte-Carlo simulations for  $N = 10$  circuits. Each point is taken from the beta fit to 100 Haar random unitaries, and the error bars are the standard deviations of the fit. This simulation was performed with  $\Gamma_{dp} = 0.001\Gamma$  and with spectral diffusion of  $\sigma_{SD} = 0.01\Gamma$ .